Università degli Studi di Napoli *Federico II*

Università di Camerino

DOTTORATO DI RICERCA IN QUANTUM TECHNOLOGIES

Ciclo XXXV

Coordinatore: prof. Francesco Tafuri

Magnetic tunnel Josephson Junctions towards hybrid quantum architectures

Settore Scientifico Disciplinare ___FIS__/____03__

Dottorando
Roberta Satariano

Tutore
Prof. Giovanni Piero Pepe

Anni 2019/2023

Contents

Motivations and Outline

Superconducting qubits have emerged as a prominent platform for realizing large-scale quantum processors [1, 2], which can fulfill remarkable computational tasks that are far beyond the capabilities of classical computers, such as prime factorization [3] and simulation of complex quantum systems [4, 5]. Superconducting qubits are lithographically defined electronic circuits, composed of elements such as Josephson Junctions (JJs), capacitors, inductors, and resonators, whose fabrication has been borrowed from well-established integrated-circuit technology. In contrast to other quantum computing modalities, e.g., electron spins, trapped ions, ultracold atoms and nitrogen-vacancies in diamond, where the quantum information is encoded in natural microscopic quantum systems, these circuits allow the design of their characteristic frequencies with a high degree of flexibility and scalability [2]. These frequencies can be tuned by adjusting an external parameter, and the coupling between two qubits can be switched on and off as required [1]. These devices have thus been successfully manipulated to effectively execute multi-qubit gate operations [6, 7] and complex quantum algorithms, including Google's pioneering experiment, demonstrating quantum computational supremacy [8].

However, despite this significant achievement, going beyond the current size of today's quantum processor consisting of few hundreds qubits to a scalable quantum processor with thousands of qubits is far from a trivial challenge. Moreover, qubits coherence times should be made as long as possible to considerably reduce the resource requirements for quantum error-correction [9]. Understanding and further mitigating sources of decoherence in superconducting qubits is thus a fundamental step for building scalable quantum computing architectures [9, 10].

Over the past two decades, the five-order-of-magnitude-increase of the relaxation coherence time has been the result of continuous improvements in fabrication techniques, materials, and circuit designs [9, 10]. The most-widely adopted superconducting qubit design, the *transmon* [11], has led to spectacular progress, but it still presents certain architectural issues. Frequency-tunable trasmon allows fast two-qubit gates, but the susceptibility to flux-noise in Superconductor Quantum Interference Devices (SQUIDs) results in typical phase coherence times of order of a few μs. Moreover, the milliampere currents used to control the flux-lines in the SQUID generate heat dissipation and introduce cross-talk, thus complicating the integration [12].

So far, superconducting quantum circuits have relied almost exclusively on Superconductor/ Insulator/ Superconductor (SIS) JJs based on Al technology. Recently, novel hybrid paradigms have been introduced demonstrating that devices integrating superconductors and exotic barriers can provide additional qubit frequency knobs [13, 14, 15, 16]. Among unconventional Josephson devices, one may benefit from combining Superconductors with Ferromagnets (F). In the last decades, the impressive developments in realizing Magnetic Josephson Junctions (MJJs) with a large variety of materials, geometries and structures have established a unique playground to explore the interplay between superconductivity and ferromagnetism. A series of fascinating experiments have revealed striking phenomena at the S/F interface, e.g., 0-π phase transition [17] and the generation of spin-triplet correlations [18], and have paved the way for new functionalities in a wide range of applications from spintronics [19] to superconducting digital electronics [20].

For what concerns the use of MJJs in quantum architectures, they have been mainly suggested as π-phase shifters or as *quiet* qubits [21, 22]. For long time, they have not been considered in the realization of active elements in quantum circuits, because of their intrinsic high dissipation resulting from the metallic nature of standard ferromagnetic barriers. Recent advances in realizing MJJs by coupling ferromagnetic layers with insulating barriers inside JJs (SIsFS or SIFS JJs) [23, 24] and by exploiting intrinsic insulating ferromagnetic materials

(SI_FS JJs) [25] have allowed to engineer MJJs with low damping and access the Macroscopic Quantum Tunneling (MQT) regime [26]. The integration of MJJs as active components in quantum circuits has thus gained attention. In Ref. [27], a proof-of-concept of a hybrid ferromagnetic transmon qubit, namely the *ferro-trasmon*, has been proposed. The main idea of the ferro-trasmon consists in the use of tunnel MJJs that allows a digital control of the qubit frequency by means of magnetic field pulses. The memory properties of MJJs enable them to retain their state at the end of the pulse, thus eliminating the need for a static field during the qubit operation that can be detrimental for coherence. This proposal may have a strong impact on the scalability of superconducting quantum systems. Indeed, the natural digital behavior of MJJs may promote alternative control schemes with energy-efficient cryogenic digital electronics.

The main aim of this thesis is to develop a tunnel MJJ suitable for the integration into the hybrid circuit mentioned above. In this pursuit, we intend to gain a deeper insight into the rich phenomenology of a special class of MJJs: the SIsFS JJs, i.e., tunnel MJJs consisting of a serial connection of SIs and sFS JJs. In contrast to SI_FS JJs that pose several limitations because of the poor availability of intrinsic ferromagnetic insulators, in SIsFS JJs a wide class of magnetic materials can be exploited to obtain the desired magnetic response. In addition, also the transport properties can be engineered to a much great extent.

In the Chapter 1, we first review the standard behavior of SIS and SFS JJs, and then we show how the SIsFS can combine the physics of their components.

In Chapter 2, we discuss the state of the art on Nb-based SIsFS JJs, which have been proposed as promising solution for the realization of a Random Access Memory for Single Flux Quantum (SFQ) electronics [23]. Then, we motivate our approach to realize scalable SIsFS JJs, demonstrating that they are the smallest memory elements compatible with standard superconducting circuits [28].

To date, the functionality of MJJs as magnetic switches for digital electronics [20] and for spintronic devices [19] has been demonstrated mostly at liquid-helium temperature. However, at the operating temperature of quantum circuits, the *inverse proximity effect*, i.e., the transfer of a ferromagnetic order into a super-

conductor from the S/F interface, can emerge and lead to a significant modification of the operating regime of the overall device. As addressed in the Chapter 3, this issue has motivated the temperature characterization of the magnetic field patterns of Nb-based SIsFS JJs down $T = 10$ mK [29, 30, 31].

Finally, in the Chapter 4, for an easy integration of the MJJs into actual quantum circuits that mostly rely on Al technology, we have successfully transferred the knowledge acquired to demonstrate the Josephson effect in SIsFS JJs with aluminum electrodes and their compatibility with the ferro-transmon design [32, 33].

Bibliography

[1] J. Clarke and F. Wilhelm. "Superconducting quantum bits." In: *Nat.* 453.10 (2008), pp. 1031–1042. DOI: 10.1109/T-ED.1980.20128.

[2] P. Krantz et al. "A quantum engineer's guide to superconducting qubits". In: *Appl. Phys. Rev.* 6.2 (2019), p. 021318. DOI: 10.1063/1.5089550.

[3] E. Lucero et al. "Computing prime factors with a Josephson phase qubit quantum processor". In: *Nat. Phys.* 8 (10 2012), pp. 719–723. DOI: 10.1038/nphys2385.

[4] R. P. Feynman. "Simulating physics with computers". In: *Int. J. Theor. Phys.* 21 (6 1982), pp. 467–488. DOI: 10.1007/BF02650179.

[5] S. Lloyd. "Universal Quantum Simulators". In: *Science* 273.5278 (1996), pp. 1073–1078. DOI: 10.1126/science.273.5278.1073.

[6] F. Yan et al. "Tunable Coupling Scheme for Implementing High-Fidelity Two-Qubit Gates". In: *Phys. Rev. Appl.* 10 (5 2018), p. 054062. DOI: 10.1103/PhysRevApplied.10.054062. URL: https://link.aps.org/doi/10.1103/PhysRevApplied.10.054062.

[7] Y. Sung et al. "Realization of High-Fidelity CZ and ZZ-Free iSWAP Gates with a Tunable Coupler". In: *Phys. Rev. X* 11 (2 2021), p. 021058. DOI: 10.1103/PhysRevX.11.021058. URL: https://link.aps.org/doi/10.1103/PhysRevX.11.021058.

[8] F. Arute et al. "Quantum supremacy using a programmable superconducting processor". In: *Nature* 574 (7779 2019), pp. 505–510. DOI: 10.1038/

s41586-019-1666-5. URL: https://doi.org/10.1038/s41586-019-1666-5.

[9] M. Kjaergaard et al. "Superconducting Qubits: Current State of Play". In: *Annual Review of Condensed Matter Physics* 11.1 (2020), pp. 369–395. DOI: 10.1146/annurev-conmatphys-031119-050605.

[10] W. D. Oliver and P. B. Welander. "Materials in superconducting quantum bits". In: *MRS Bulletin* 38.10 (2013), pp. 816–825. DOI: 10.1557/mrs.2013.229.

[11] J. Koch et al. "Charge-insensitive qubit design derived from the Cooper pair box". In: *Phys. Rev. A* 76 (4 2007), p. 042319. DOI: 10.1103/PhysRevA.76.042319.

[12] R. Aguado. "A perspective on semiconductor-based superconducting qubits". In: *Appl. Phys. Lett* 117.24 (2020), p. 240501. DOI: 10.1063/5.0024124.

[13] T. W. Larsen et al. "Semiconductor-Nanowire-Based Superconducting Qubit". In: *Phys. Rev. Lett.* 115 (12 2015), p. 127001. DOI: 10.1103/PhysRevLett.115.127001. URL: https://link.aps.org/doi/10.1103/PhysRevLett.115.127001.

[14] F. Luthi et al. "Evolution of Nanowire Transmon Qubits and Their Coherence in a Magnetic Field". In: *Phys. Rev. Lett.* 120 (10 2018), p. 100502. DOI: 10.1103/PhysRevLett.120.100502. URL: https://link.aps.org/doi/10.1103/PhysRevLett.120.100502.

[15] L. Casparis et al. "Superconducting gatemon qubit based on a proximitized two-dimensional electron gas". In: *Nat. Nanotechnol.* 13.10 (2018), pp. 913–919. DOI: 10.1038/s41565-018-0207-y.

[16] J. I. Wang et al. "Coherent control of a hybrid superconducting circuit made with graphene-based van der Waals heterostructures". In: *Nat. Nanotechnol.* 14 (2 2019), pp. 120–125. DOI: 10.1038/s41565-018-0329-2.

[17] A. A. Golubov, M. Yu. Kupriyanov, and E. Il'ichev. "The current-phase relation in Josephson junctions". In: *Rev. Mod. Phys.* 76 (2 2004), pp. 411–469. DOI: 10.1103/RevModPhys.76.411.

[18] F. S. Bergeret, A. F. Volkov, and K. B. Efetov. "Odd triplet superconductivity and related phenomena in superconductor-ferromagnet structures". In: *Rev. Mod. Phys.* 77 (2005), pp. 1321–1373.

[19] J. Linder and J. W. A. Robinson. "Superconducting spintronics". In: *Nat. Phys.* 11 (2015), pp. 307–315.

[20] I. I. Soloviev et al. "Beyond Moore's technologies: operation principles of a superconductor alternative". In: *Beilstein J. Nanotechnol.* 8 (2017), pp. 2689–2710. DOI: doi:10.3762/bjnano.8.269.

[21] A. K. Feofanov et al. "Implementation of superconductor/ferromagnet/superconductor π-shifters in superconducting digital and quantum circuits". In: *Nat. Phys.* 6 (8 2010), pp. 593–597. DOI: 10.1103/PhysRevB.103.094509. URL: https://link.aps.org/doi/10.1103/PhysRevB.103.094509.

[22] A. V. Shcherbakova et al. "Fabrication and measurements of hybrid Nb/Al Josephson junctions and flux qubits with π-shifters". In: 28.2 (2020), p. 025009. DOI: https://doi.org/10.1007/s10948-020-05577-0. URL: https://dx.doi.org/10.1088/0953-2048/28/2/025009.

[23] T. I. Larkin et al. "Ferromagnetic Josephson switching device with high characteristic voltage". In: *Appl. Phys. Lett.* 100 (2012), p. 222601.

[24] M. Weides et al. "High quality ferromagnetic 0 and π Josephson tunnel junctions". In: *Appl. Phys. Lett.* 89.12 (2006), p. 122511. DOI: 10.1063/1.2356104.

[25] K. Senapati, M. G. Blamire, and Z. H. Barber. "Spin-filter Josephson junctions". In: *Nat. Mater.* 10 (2011), pp. 849–852. DOI: 10.1038/nmat3116.

[26] D. Massarotti et al. “Macroscopic quantum tunnelling in spin filter ferromagnetic Josephson junctions”. In: *Nat. Commun.* 6 (2015), p. 7376. DOI: 10.1038/ncomms8376.

[27] H. G. Ahmad et al. “Hybrid ferromagnetic transmon qubit: Circuit design, feasibility, and detection protocols for magnetic fluctuations”. In: *Phys. Rev. B* 105 (21 2022), p. 214522. DOI: 10.1103/PhysRevB.105.214522.

[28] L. Parlato et al. “Characterization of scalable Josephson memory element containing a strong ferromagnet”. In: *J. Appl. Phys.* 127 (2020), p. 193901. DOI: https://doi.org/10.1063/5.0004554.

[29] R. Satariano et al. “Inverse magnetic hysteresis of the Josephson supercurrent: study of the magnetic properties of thin Nb/Py interfaces”. In: *Phys. Rev. B* 103 (2021), p. 224521. DOI: 10.1103/PhysRevB.103.224521.

[30] R. Satariano et al. “Investigation of the inverse magnetic hysteresis of the Josephson supercurrent in magnetic Josephson Junctions”. In: *IEEE Trans. Appl. Supercond.* (2021), pp. 1–1. DOI: 10.1109/TASC.2021.3129983.

[31] R. Satariano. “Nanoscale spin ordering and full screening in tunnel ferromagnetic Josephson junctions”. In: *in preparation* (2023).

[32] A. Vettoliere et al. “Aluminum-ferromagnetic Josephson tunnel junctions for high quality magnetic switching devices”. In: *Appl. Phys. Lett.* 120.26 (2022), p. 262601. DOI: 10.1063/5.0101686.

[33] A. Vettoliere et al. “High-Quality Ferromagnetic Josephson Junctions Based on Aluminum Electrodes”. In: *Nanomaterials* 12.23 (2022). DOI: 10.3390/nano12234155.

Chapter 1

Josephson effect and magnetism

The aim of this Chapter is to introduce the major notions and theories to which we refer throughout this thesis. We review the main features of the Josephson effect in standard tunnel Superconductor/ Insulator/ Superconductor (SIS) and metallic ferromagnetic Superconductor/ Ferromagnet/ Superconductor (SFS) Josephson Junctions (JJs). Then, we show a new type of magnetic JJs (MJJs) consisting of a complex weak link through a IsF barrier. With a proper choice of the s layer thickness and F material, these structures behave as a serial connection of a SIs tunnel junction and an sFS sandwich, thus, paving the way for realizing switchable elements with high quality factor. As it will be addressed in the next Chapters, such tunnel SIsFS JJs can provide novel functionalities not only in superconducting digital circuits, but also in hybrid quantum architectures.

1.1 The Josephson effect

1.1.1 Josephson equations

In a Superconductor (S), at temperatures T lower than its critical temperature T_c, a condensate of the Cooper pairs forms, described by a single wave-function Ψ. If we consider two superconductors S_1 and S_2 separated by a macroscopic distance, the phase of the two superconductors can change independently. If we reduce the distance S_1 and S_2 down to about 1 nm, the Cooper pairs can flow from one superconductor to the other (Josephson tunneling). In this situation, the long-range order is transmitted across the boundary. Therefore, we expect that the whole system of the two superconductors separated by a thin insulating barrier will be behave, to some extent, as a single superconductor [1]. This phenomenon is often referred as *weak superconductivity*, because of the much lower values of the critical parameters involved [2]. Such *weak link* occurs any time the macroscopic wave-functions of the two superconducting electrodes $\Psi_1 = |\Psi_1| e^{i\varphi_1}$ and $\Psi_2 = |\Psi_2| e^{i\varphi_2}$ overlap in the barrier region (Fig. 1.1). The weak coupling can be realized in sandwich structures with metallic or ferromagnetic barriers by proximity effect. A superconducting film with a short narrow constriction (*Dayem bridge* [3]) falls into this category, provided the size of the constriction is of the order of the superconducting coherence length ξ_S, i.e., the Cooper pair size. In all these cases we refer as Josephson Junction (JJ), in honor of Brian Josephson the physicist who first theoretically predicted the tunneling of Cooper pairs through an insulating barrier [4].

According to the *first Josephson equation*, in absence of an applied voltage, the supercurrent depends solely on the phase difference across the two superconducting electrodes φ:

$$I = I_c \sin \varphi, \tag{1.1}$$

where I_c is the *critical current*, i.e., the maximum dissipation-free current through the junction. It depends on the temperature and the magnetic field and is subject to fluctuations [5]. In case of unconventional systems, the current-phase relation

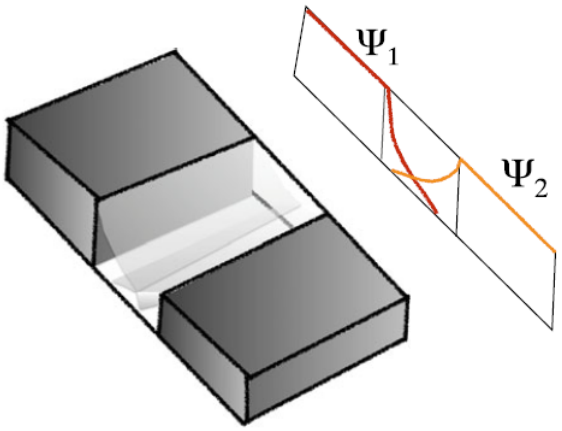

Figure 1.1. The Josephson effect occurs as long as the macroscopic wave-functions of the two electrodes $\Psi_1 = |\Psi_1| e^{i\varphi_1}$ and $\Psi_2 = |\Psi_2| e^{i\varphi_2}$ overlap in the barrier region.

1.1 should be generalized in order to take into account also higher harmonics [6]:

$$I(\varphi) = \sum_{n \geq 1} I_n \sin(n\varphi). \tag{1.2}$$

If φ evolves over time, a voltage difference V appears across the superconducting electrodes, according to the *second Josephson relation*:

$$V(t) = \frac{\hbar}{2e} \frac{d\varphi}{dt}, \tag{1.3}$$

where e and $\hbar$ are the electron charge and the reduced Planck constant, respectively. If we apply a constant voltage $V \neq 0$, it follows by integration of (1.3) that phase difference φ varies in time as $\varphi = \varphi_0 + \frac{2e}{\hbar} Vt$. Therefore, an alternative current appears:

$$I = I_c \sin(\varphi_0 + \frac{2e}{\hbar} Vt) \tag{1.4}$$

with a frequency $\omega = 2\pi\nu = 2eV/\hbar$. This is called the *a.c. Josephson effect*. The ratio between frequency and voltage is constant and is given by:

$$\frac{\nu_0}{V} = \frac{2e}{h} = 483.6 \text{ MHz}/\mu \text{ V}. \tag{1.5}$$

A microwave tone applied to a JJ biased with a d.c. current leads to the appearance of current steps at constant voltages. The steps current occurs at voltage:

$$V_n = \frac{nh}{2e}\nu_0, \tag{1.6}$$

where n is an integer number and ν_0 is the frequency of the applied radiation. Such steps have been observed for the first time by Shapiro in 1963 [7] and are thus called *Shapiro steps*.

1.1.2 Josephson Junctions (JJs) in a magnetic field

One of the most striking features of the Josephson structures is the occurrence of diffraction and interference phenomena when magnetic fields are applied. This is a consequence of the wave-like nature of Cooper pairs and the phase coherence through the Josephson link. With reference to axis system in Fig. 1.2a, by applying a magnetic field along the y direction H_y, the phase difference φ assumes a spatial dependence of the form:

$$\varphi(x) = \frac{2e}{\hbar}d_m H_y x + \varphi_0, \tag{1.7}$$

where d_m is the magnetic thickness, i.e., the thickness penetrated by the external magnetic field H_y, given by $d_m = \lambda_{L,1} + \lambda_{L,2} + d_I$ with $\lambda_{L,1}$ and $\lambda_{L,2}$ the London penetration depths in the two superconductors and d_I the thickness of the oxide layer and φ_0 is the phase difference for $x = 0$. By substituting Equation 1.7 in Equation 1.1 and by integrating over the entire junction area, we obtain the analytical expression of critical current $I_c(H)$. A rectangular junction with a lateral size L and a uniform zero-field tunneling current distribution exhibits a dependence of the maximum supercurrent on the applied magnetic field in the form of a Fraunhofer-like diffration pattern:

$$I_c(H) = I_c(0)\left|\frac{\sin(\pi\frac{\Phi}{\Phi_0})}{\pi\frac{\Phi}{\Phi_0}}\right|, \tag{1.8}$$

where $\Phi = \mu_0 H L d_m$ is the flux threading the junction and $\Phi_0 = h/2e$ is the magnetic flux quantum (2.07×10^{-15} Wb). Thus, for a rectangular JJ the minima in

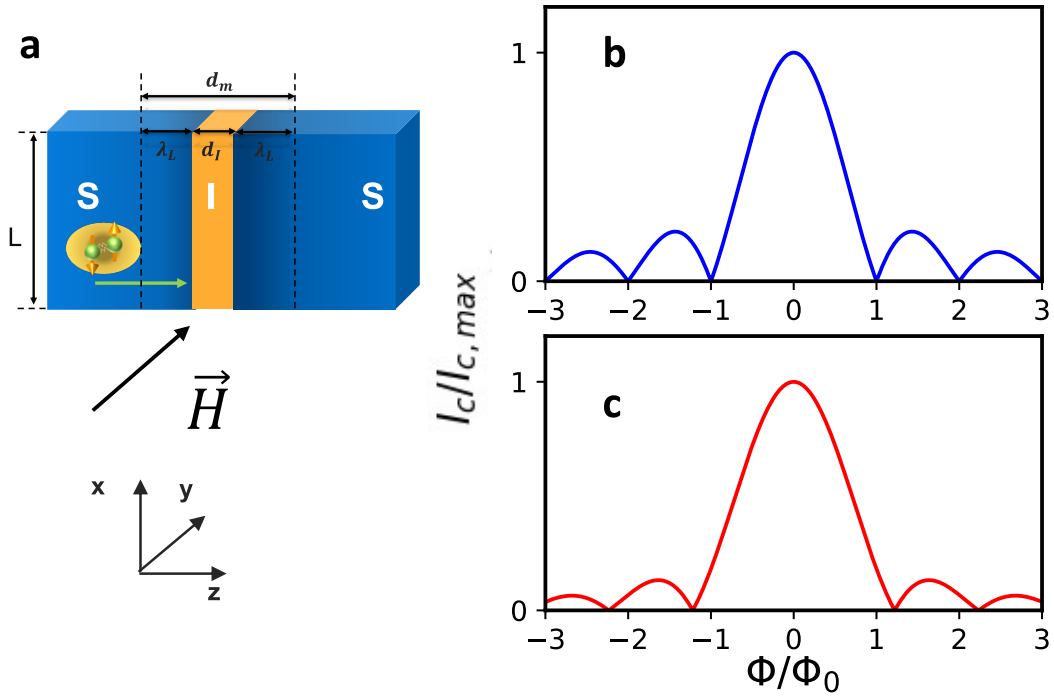

Figure 1.2. (a) Sketch of a standard Josephson Junction (JJ) in presence of a magnetic field **H** along y direction. The supercurrent flows without dissipation until a critical current I_c value is reached. Magnetic dependence of the critical current $I_c(H)$, normalized to its maximum value $I_{c,max}(H)$, for (b) a rectangular and (c) circular JJ. The $I_c(H)$ curve follows a Fraunhofer and Airy pattern, respectively.

the pattern occur at multiples integer of Φ_0 (Fig. 1.2b).

For circular JJs with a uniform zero-field tunneling current distribution, the analytical expression of the $I_c(H)$ follows an Airy pattern (Fig. 1.2c):

$$I_c(H) = I_c(0)\left|\frac{2\mathfrak{J}_1\left(\frac{2\pi\Phi}{\Phi_0}\right)}{\frac{2\pi\Phi}{\Phi_0}}\right|, \tag{1.9}$$

where $\mathfrak{J}_1$ is a Bessel function of the first kind. In this case, the flux threading the junction is: $\Phi = \mu_0 H 2Rd_m$with R the JJ radius.

This description is valid within the *short junction limit*, i.e., when L is smaller than the Josephson penetration depth λ_J:

$$\lambda_J = \sqrt{\frac{\Phi_0}{2\pi\mu_0 j_c d_m}}, \tag{1.10}$$

where j_c is the critical current density. In this limit, the self-field due to the current flowing in the junction electrodes can be neglected. Deviations from the $I_c(H)$ expected behavior, such as minima with non-zero current, suppression of the amplitude of secondary lobes, asymmetries or distortions of the pattern, can be related to a non-uniform current distribution, an arbitrary orientation of the in-plane magnetic field or to structural fluctuations [1].

1.1.3 Phase dynamics

The physical processes occurring in JJs are encoded in their current-voltage (I-V) curve. Modeling I-V characteristics is the first step to define the transport mechanism of a junction, its electrodynamics, and to understand its potential applications for digital and quantum circuits.

According to the Resistively and Capacitively Shunted Junction (RCSJ) model, a JJ in an external circuit can be modeled as an ideal JJ in parallel with a resistance R and a capacitor C [1, 8, 9, 10, 11]. The capacitance C arises from the charge accumulation at the interfaces between the superconducting electrodes, whereas the ohmic element is due to the generation of a dissipative current.

If we assume that only a d.c. current I is present, the balance equation for this

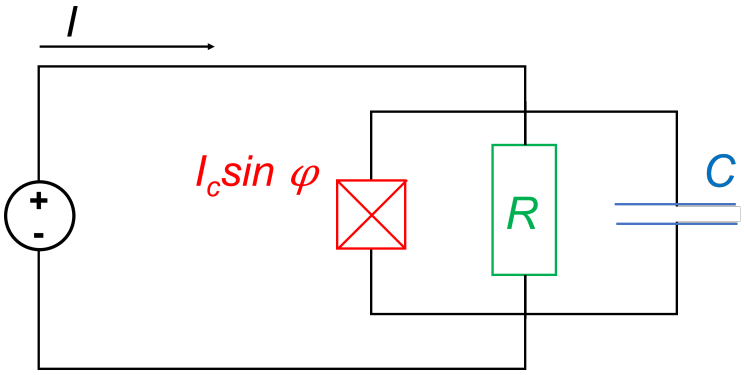

Figure 1.3. Equivalent circuit for the Resistively and Capacitively Shunted Junction (RCSJ) model.

circuit in Fig. 1.3 is:

$$I = I_c \sin\varphi + \frac{V}{R} + C\frac{dV}{dt}. \tag{1.11}$$

By using Equation 1.1-1.3, the expression 1.11 can be transformed into an equation for the phase φ:

$$I = \frac{\hbar}{2e}\, C\, \frac{d^2\varphi}{dt^2} + \frac{\hbar}{2e}\, \frac{1}{R}\, \frac{d\varphi}{dt} + I_c \sin\varphi. \tag{1.12}$$

Multiply by $\frac{\hbar}{2e}$ and defining the Josephson coupling energy as

$$E_J = \frac{\hbar I_c}{2e} \tag{1.13}$$

we obtain:

$$\left(\frac{\hbar}{2e}\right)^2 C\, \frac{d^2\varphi}{dt^2} + \left(\frac{\hbar}{2e}\right)^2 \frac{1}{R}\, \frac{d\varphi}{dt} + \frac{d}{d\varphi}\left\{E_J\left[\cos\varphi - \frac{I}{I_c}\varphi\right]\right\} = 0. \tag{1.14}$$

It can be easily seen that Equation 1.14 is equivalent to the motion equation of a phase particle of mass $M = \left(\frac{\hbar}{2e}\right)^2 C$ subject to a damping $\eta = \left(\frac{\hbar}{2e}\right)^2 \frac{1}{R}$ and moving in a *tilted washboard potential U(φ, I)*:

$$U(\varphi, I) = E_J\left(-\cos\varphi - \frac{I}{I_c}\varphi\right). \tag{1.15}$$

Equation 1.12 is often written in dimensionless variables by introducing the quality factor $Q = \omega_P RC$ and the normalized time $\tau = \omega_P t$, where $\omega_P = \sqrt{\frac{2eIc}{\hbar C}}$ is the plasma frequency. By this choice, Equation 1.12 becomes [10]:

$$\frac{d^2\varphi}{d\tau^2} + \frac{1}{Q}\frac{d\varphi}{d\tau} + \sin\varphi = \frac{I(\varphi)}{I_c}. \tag{1.16}$$

The phase dynamics can be discussed by using the tilted washboard potential analogy (Fig. 1.4).

- For $I < I_c$, the phase particle φ is trapped in a minimum and oscillates at the plasma frequency $\omega_p/2\pi$ [12]. This corresponds to the superconducting branch of the I-V curve.

- Increasing the bias current for $I \geq I_c$, the phase particle escapes from the potential well: the transition from the superconductive to resistive state

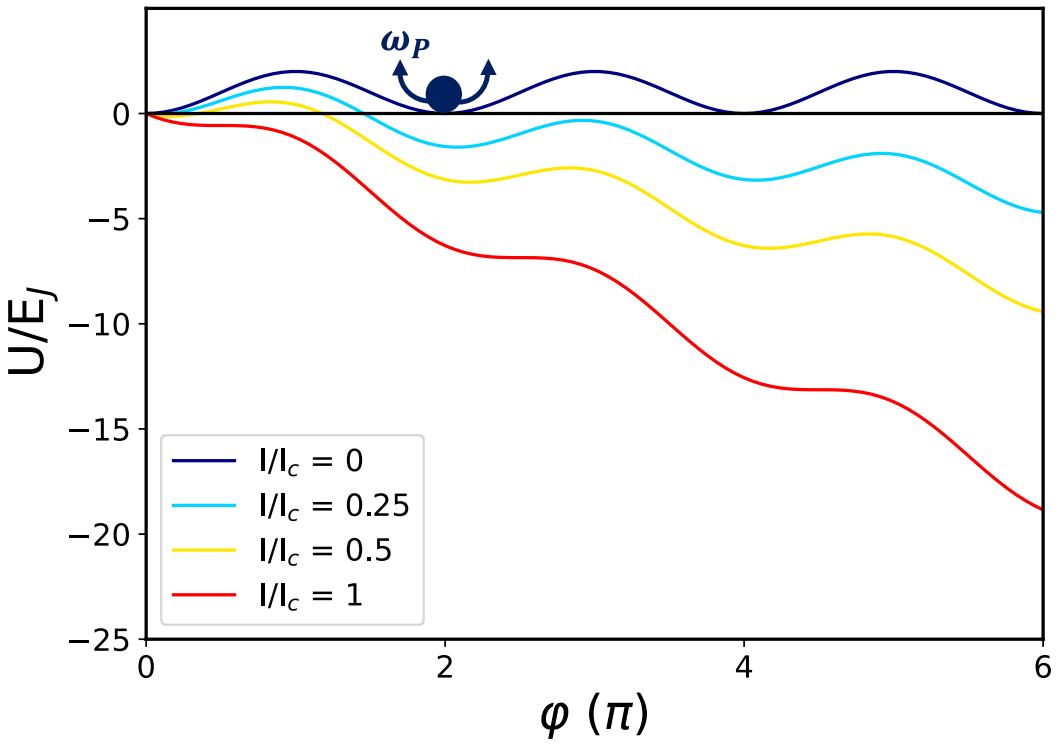

Figure 1.4. Analogy between the motion of the gauge-invariant phase difference of a Josephson junction φ and the damped motion of a particle of mass M in the tilt washboard potential.

occurs with a switch to a finite voltage V_{sw}, which in the ideal case is the sum of the gap values of the two electrodes $V_g = |(\Delta_1 + \Delta_2)/e|$. Thus, the phase particle starts rolling down the washboard potential and this corresponds to the ohmic branch of the I-V curve, characterized by a normal resistance R_N.

- When decreasing the bias current to $I < I_c$, the particle remains in a non-ohmic resistive state that corresponds to the subgap branch of the I-V curve. The phase particle remains in this state until the current reaches a certain value, called *retrapping current* I_r.

- In the case of overdamped regime ($Q < 1$), the particle will immediately stop its motion and will be trapped in one of the local minima, because of its small kinetic energy ($\propto C$) and of the large damping ($\propto 1/R$). These features are typical of JJ with a non-insulating, metallic barrier. For these

JJs, the phase does no longer evolve in time and the junction switches into the zero voltage state as soon as the applied current is reduced below I_c (non-hysteretic I-V in Fig 1.5a).

- In the case of underdamped regime ($Q \gg 1$), the massive particle due to sufficient kinetic energy and to small damping can easily move down the potential even if there are local minima. In order to stop the particle, the potential has to be brought almost to the horizontal position. For the JJ with dielectric barrier characterized by high value of the capacitance C, the current has be to reduced almost to zero to return to the zero-voltage state of the junction, i.e.,$I_r \sim 0$ (hysteretic I-V in Fig 1.5b).

- For $I < I_r$, the particle is trapped again in a minimum of the potential, thus returning to the superconducting branch.

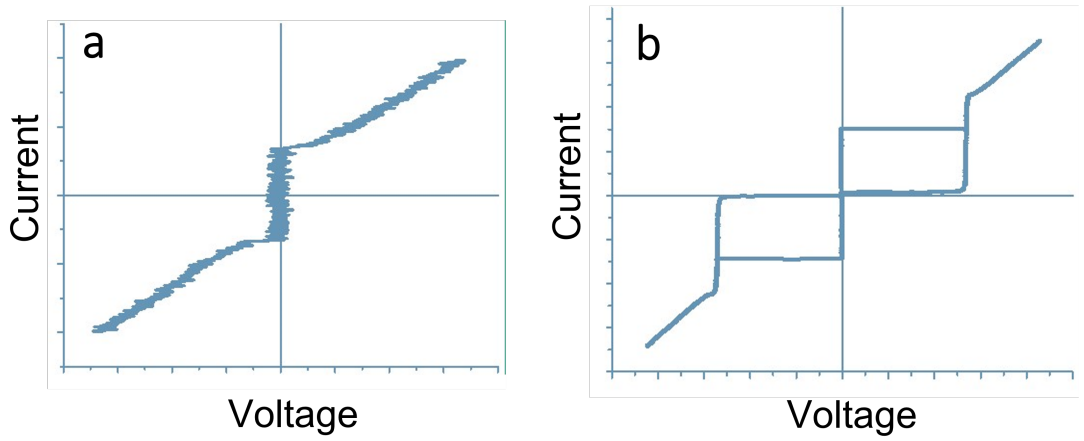

Figure 1.5. Current-voltage characteristics of (a) an overdamped and (b) underdamped JJ.

The above description of the JJ is effectively a zero-temperature description. At a finite temperature, thermal fluctuations excite the phase particle above the energy barrier, causing the switch to the resistive state. The process escape rate follows the very general Arrhenius law [13]. In underdamped junctions and at very low temperatures, the phase escapes from the well through quantum tunneling [14]: rather than hopping over the potential barrier, the phase particle tunnels through it. In this regime, the escape becomes independent of temperature. Both thermal

activation (TA) and Macroscopic Quantum Tunneling (MQT) escape processes can be studied by performing switching current distribution measurements as function of the temperature [15, 16, 17]. Finally, in overdamped and moderately damped junctions, the phase particle can be retrapped in one of the following minima after an escape event (*phase diffusion*). At low current bias, escape and retrap events can occur multiple times, preventing the switch to the running state until the tilt of the potential is increased. In this case, a finite voltage appears in the superconducting branch of the I-V curve [18, 19].

The RCSJ model is appropriate when the JJs fall in the overdamped regime. Since the capacitance C is small, second derivative term in Equation 1.16 can be neglected and the equation can be solved analytically. However, the strongly non-linear voltage dependence of the subgap branch in tunnel junctions has caused difficulties in comparing experimental and theoretical curves, thus promoting alternative models. In non-linear resistive (RSJN) model [20, 21], the term $I_N = V/R_N$ in Equation 1.11 has been for instance approximated by a simple piecewise-linear behavior:

$$I_n(V) = V \times \begin{cases} 1/R_L & for\ |V| < V_g \\ 1/R_N & for\ |V| > V_g \end{cases} \tag{1.17}$$

or by a power-law:

$$I_N(V) = \frac{V}{R_N} \frac{(V/V_g)^n}{1 + (V/V_g)^n} \tag{1.18}$$

with $n \gg 1$.

The Tunnel Junction Microscopic (TJM) model provides a more sophisticated description of the non-linear voltage dependence of the quasiparticle resistance [1]. Referring to [1, 11] for further details, here we recall just the main notions. Basically, in the TJM model the simple sinusoidal current-phase relation and the external parallel resistance used in the basic RCSJ model (Equation 1.11) are replaced by a more general expression for the current $I(\varphi)$ derived by the microscopic theory, which includes the effects of both quasiparticles and pairs transport:

$$I = \frac{\Phi_0}{2\pi} C \frac{\partial^2 \varphi}{\partial t^2} + I(\varphi), \tag{1.19}$$

where the phase φ is related to the voltage through the a.c. Josephson relation (Equation 1.3):

$$\varphi(t) = \frac{2\pi}{\Phi_0}\int_0^t V(t')dt'. \tag{1.20}$$

In the adiabatic approximation, the voltage *V(t)* is small and slowly dependent on time, when compared with the gap frequency $2\Delta/\hbar$ and Equation 1.20 thus turns into:

$$I = \frac{\Phi_0}{2\pi}C\frac{\partial^2\varphi}{\partial t^2} + I_{qp}V(t) + I_{J2}V(t)\cos(\varphi(t)) + I_{J1}V(t)\sin(\varphi(t)). \tag{1.21}$$

In Equation 1.21, the time-dependent total current *I(t)* that flows in the device is given by the sum of the supercurrent term I_{J1} and I_{J2}, due to the tunneling of Cooper pairs, and a quasiparticle dissipative current I_{qp}. The phase-dependent quasiparticle term in Equation 1.21 is not simply related to the ohmic resistance R_N, but to the shape of the subgap branch and its slope near the superconducting branch, i.e., the *subgap resistance* R_{sg}. Therefore, the TJM model is a powerful tool to the estimate the quasiparticle tunneling, which in general is a figure of merit in all classical and quantum circuits. For instance, as illustrated in the Chapter 4, JJs exploited in superconducting qubits are designed in order to have large subgap resistance to reduce quasiparticle noise that affect both the relaxation and the coherence times [22, 23].

1.2 Magnetic Josephson Junctions (MJJs)

In our experimental work, we simultaneously exploit superconducting and magnetic materials to create novel ferromagnetic Josephson switching elements having their two competing orders. In this Section, we first give a brief introduction on the ferromagnetism, focused on the type and appearance it takes in our devices. Then, taking into account the metallic nature of standard ferromagnetic barrier, we introduce the *proximity effect* as the fundamental mechanism related to transport through a S/ Normal metal (N) interface. At the end, we examine the specific features of SF systems in terms of both transport properties and magnetic response to an applied field.

1.2.1 Fundamentals of ferromagnetism

Ferromagnetic order

As superconductors, ferromagnetic materials are characterized by spontaneous broken symmetry below a critical temperature, namely the Curie temperature T_{Curie} [24]. For $T > T_{\text{Curie}}$, the ground state of the system is symmetric, i.e., each magnetic moment can point in any direction (disordered paramagnetic phase). For $T < T_{\text{Curie}}$, the rotational symmetry is broken since now the ground state consists of spins aligned along the same directions. The vanishing of magnetization at $T = T_{\text{Curie}}$ is a second-order phase transition in which the spontaneous magnetization (order parameter) changes discontinuously as a function of the temperature. Near the Curie temperature, according to Landau's approach to study phase transitions, the magnetization is proportional to $(T - T_{\text{Curie}})^{1/2}$. However, in real systems, it is found that the magnetization does behave as $(T - T_{\text{Curie}})^{\beta}$ close to the transition, but the exponent β is not necessarily equal to $\frac{1}{2}$. At low temperatures, the temperature dependence of the spontaneous magnetization can be fitted using a spin-wave model and it follows the Bloch $T^{3/2}$ law [25].

We deal with itinerant ferromagnets, such as those made of iron (Fe) or nickel

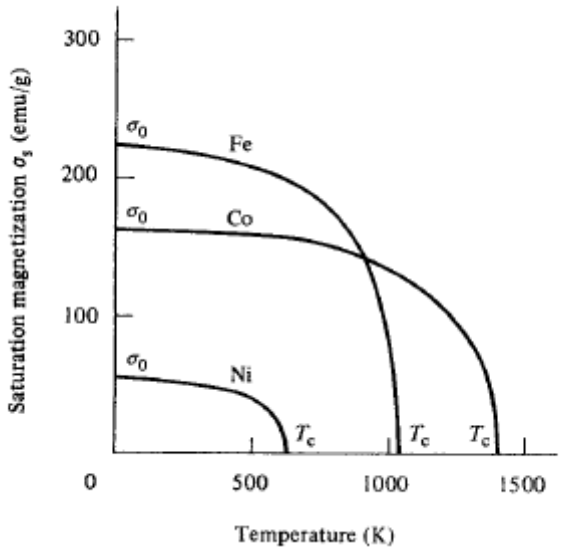

Figure 1.6. Saturation magnetization of iron (Fe), cobalt (Co), and nickel (Ni) as a function of temperature T [26].

(Ni), whose spins aligned to create the magnetic state are also responsible for

conduction. Experimental data on the variation of the saturation magnetization M_s of Fe, Co, and Ni with temperature can be found in Fig. 1.6. In band-ferromagnetism, the magnetization is due to spontaneously spin-splitting. One spin-band (majority band) contains more electrons $n_\uparrow$ and is filled up a to a higher energy level compared to the other spin-band (minority band) that contains $n_\downarrow$ electrons (Fig. 1.7). As a result, the number of electrons above the Fermi level is $N(E_F)\delta E/2$ with an increase in energy δE, where $N(E_F)$ is the density of states (DOS) at the Fermi energy E_F. The total kinetic energy change is therefore:

$$\Delta E_K = \frac{1}{2} N(E_F)\delta E^2. \tag{1.22}$$

This process has an energy cost and looks thus unfavourable. However, in molecular field theory all spins experience an identical average exchange field ($H_{ex} = \lambda M$) produced by all their neighbours. The interaction of the magnetization with the molecular field gives an energy reduction that can exceed this cost. The number density of spin-up is $n_\uparrow = \frac{1}{2}(n + N(E_F)\delta E)$ and the number density of spin-down is $n_\downarrow = \frac{1}{2}(n - N(E_F)\delta E)$ with $n = n_\uparrow + n_\downarrow$. The magnetization is thus $M = \mu_B(n_\uparrow - n_\downarrow)$, under the assumption that each electron has a magnetic moment equal to the Bohr magneton μ_B. The resulting potential energy change is:

$$\Delta E_P = -\frac{1}{2}\mu_0 \lambda M^2 = -\frac{1}{2}\mu_B^2 \mu_0 \lambda (n_\uparrow - n_\downarrow)^2 = -\frac{1}{2} U (N(E_F)\delta E)^2, \tag{1.23}$$

where $U = \mu_B^2 \mu_0 \lambda$ is a measure of the exchange correlation. The total change of energy ΔE is:

$$\Delta E = \frac{1}{2} N(E_F)\delta E^2 (1 - U N(E_F)). \tag{1.24}$$

Thus, spontaneous spin-splitting is possible if $\Delta E \leq 0$, which leads to the *Stoner criterion* of the ferromagnetism to occur for $UN(E_F) \geq 1$ [27]. This condition for the ferromagnetic stability requires that the Coulomb effects are strong and also that the density of states at the Fermi energy is large [25].

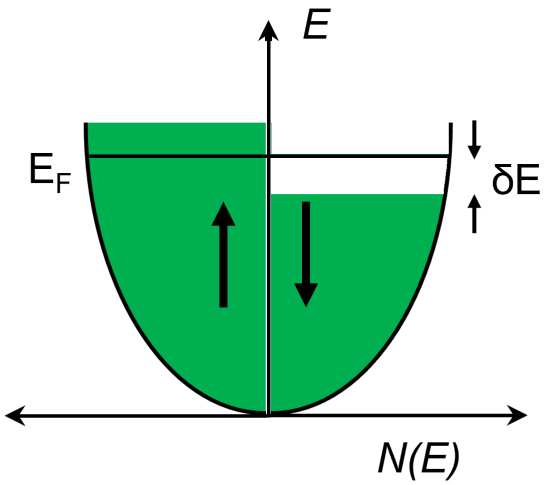

Figure 1.7. Stoner criterion for ferromagnetism

Magnetic energies

The magnetic behavior of a ferromagnetic material is determined by a trade-off between competing energies. The main terms that must be considered are the following.

- The *exchange energy* (E_{ex}), introduced above, is the interaction between nearby electron spins and is minimized for parallel alignment of the spin. If two atoms i and j have spin angular momentum $\mathbf{S}_i$ and $\mathbf{S}_j$, respectively, the exchange energy E_{ex} between them is given by:

$$E_{ex} = -2J_{ex}\mathbf{S}_i \cdot \mathbf{S}_j = -2J_{ex}S_i \cdot S_j \cos\phi, \tag{1.25}$$

  where J_{ex} is a particular constant, called the *exchange integral*, which occurs in the calculation of the exchange effect, and ϕ is the angle between the spins. For a ferromagnet J_{ex} is positive, E_{ex} is minimized when the spins are parallel. A useful constant to quantify the exchange coupling is A the *exchange stiffness*. It is a measure of the force tending to keep adjacent spins parallel to one another, i.e., of the torsional stiffness of spin-spin coupling. It is related to the exchange integral J_{ex} by:

$$A = \frac{nJ_{ex}S^2}{a}, \tag{1.26}$$

with S is the spin, a the lattice parameter, and n is the number of atoms in the unit cell [26].

- The *magnetocrystalline anisotropy energy* (E_{anis}) relates the direction of the magnetization with the lattice orientation. When an external field H tries to orient the spin of an electron, the orbit of that electron also tends to be oriented. However, the orbit of the electron is strongly coupled to the lattice and therefore resists the attempt to rotate the spin axis. Thus, the magnetocrystalline anisotropy energy is the energy required to overcome the spin–orbit coupling [26]. For a uniaxial anisotropy, the energy density can be written as:

$$E_{anis} = K_0 + K_1 \sin^2\theta + K_2 \sin^4\theta + ... \tag{1.27}$$

  When K_1 and K_2 are both positive, the energy is minimized for $\theta = 0$ and the axis corresponds to an easy axis of magnetization. When K_1 and K_2 are both negative, the energy is minimized for $\theta = 90°$ and this leads to an easy plane of magnetization lying perpendicular to the axis [26]. Anisotropy constants are usually in the range $10^2 - 10^7$ J/m^3 [25].

- Because $\nabla\cdot\mathbf{H} = -\nabla\cdot\mathbf{M}$, at the edges of a sample the magnetic field diverges and this produces demagnetizing fields, which fill space and cost $B^2/2\mu_0$ Joules of energy per cubic metre. The energy associated with the demagnetizing field is called, variously, the *demagnetization energy*, *magnetostatic energy* or *dipolar energy* (E_{dip}). It takes the value:

$$E_{dip} = -\frac{\mu_0}{2}\int_V \mathbf{M}\cdot\mathbf{H_d}\; d\tau, \tag{1.28}$$

  where $\mathbf{H_d}$ is the *demagnetizing field*, also called the *stray field* outside the ferromagnet $\mathbf{H_s}$, and the integral is taken over the volume of the sample. For an ellipsoidally shaped sample magnetized along one of its principal

axes, this energy reduces to

$$E_{dip} = \frac{\mu_0}{2} N_d M^2 V, \tag{1.29}$$

where N_d is the *demagnetizing factor* and V is the sample volume [25]. The value of N depends mainly on the shape of the body, and has a single calculable value only for ellipsoid. It is minimized by keeping flux inside the ferromagnet: for example, in ferromagnetic thin films, it is minimized by keeping the magnetization in-plane [28].

- *Zeeman energy* (E_{Zeeman}) is the potential energy of a magnetized body in an external magnetic field **H** and is minimized for parallel alignment. The Zeeman energy can be defined as:

$$E_{\text{Zeeman}} = -\mu_0 \int_V \mathbf{M} \cdot \boldsymbol{H}, \tag{1.30}$$

where the integral is done over the volume of the body V.

Domains and magnetization processes

A ferromagnet in the demagnetized state is divided into a number of small regions called *domains*. Each domain is spontaneously magnetized to the saturation value M_s, but the directions of magnetization of the various domains are such that a specimen as a whole has no net magnetization. The domains are separated by domain walls, in which the magnetization vector rotates from the direction of the domain on one side to the direction of the domain on the other side. Two main classes of domain walls are distinguished. In Bloch walls the rotation goes out-of-plane, while in Néel walls it goes in-plane. Dipolar energy determines the type of domain wall that can form: Bloch walls are favored in the bulk, whereas Neel walls tend to be favored in thin films, where there is an energy saving for keeping the magnetization in the plane of the film [25]. Other more complex rotation exists, but they are always a combination of the Bloch and Néel type [29]. The competition of the exchange energy and anisotropy yields the so-called *Bloch wall*

width or *exchange length*: $\Delta = \sqrt{A/K_1}$ for the case of uniaxial anisotropy. While the exchange energy tries to make the wall as wide as possible, in order to make the angle ϕ between adjacent spins as small as possible, the anisotropy energy tries to make the wall thin, in order to reduce the spin pointing in an uneasy direction.

The appearance of the domain and its configuration result from the minimization

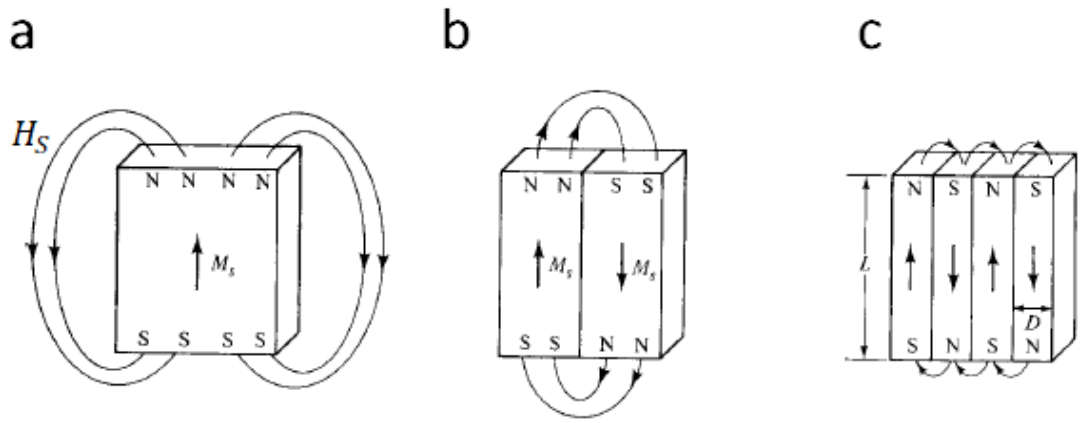

Figure 1.8. The division of a crystal into domains results from a minimization of the magnetostatic energy of the overall sample [26].

of the overall energy of the system. In Fig. 1.8a we have a single-domain: as a consequence, free poles form on the edges, thus resulting in a large stray-field. The magnetostatic energy evaluated over all space (Equation 1.28) can be reduced by almost a factor of 2 if the crystal splits into two domains magnetized in opposite directions as in Fig. 1.8b, because this brings north and south poles closer to one another, thus decreasing the spatial extent of the stray fields. The so-called closure domain structure in Fig. 1.8c minimizes the dipolar energy but introduces numerous domain walls [30]. However, the division into smaller and smaller domains cannot continue indefinitely, because of the formation of domain walls, which add energy to the system. Therefore, in the same way as the size of a domain wall is a balance between the exchange and anisotropy energies, so the formation of domains is a balance between the cost of a demagnetizing field and the cost of a domain wall [25].

During the process of magnetization, a specimen from a multi-domain state

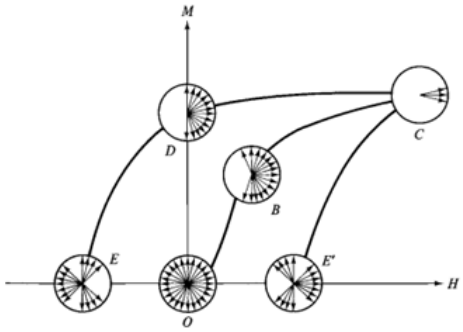

Figure 1.9. Domain arrangements for various states of magnetization [31].

is converted into a single-domain along the direction of the applied field H, as shown in Fig. 1.9. The arrangements of vectors M_s in the domains is represented by a set of vectors drawn from a common origin. The ideal demagnetized state is shown at point O. When a positive field is applied, domains magnetized in the opposite direction are eliminated first by 180° wall motion, leading to the distribution shown at point B. The motion of domain walls depends in detail upon the metallurgical properties of the material. Domain walls can be pinned by strains, by dislocations and impurities that increase thus the fields to magnetize the sample. Further increase in field rotates spin within the domains into the state of saturation shown at C. Since the crystalline anisotropy energy contribution must be overcome, a large increase in the H field produces a relatively small increase of M. When the field is now removed, the domain vectors fall back to the easy direction in each grain nearest to the $+H$ direction. After being partially saturated, now the ferromagnet shows a significant magnetization in zero applied field, i.e., a *remanent magnetization* M_r. The effect of applying a negative field to the remanent state is to first reverse the domain magnetization pointing in the $+H$ direction, leading to state E at the *coercive field* H_c.

The energy dissipated (as heat) by a ferromagnet as it is taken around a circuit of its hysteresis loop is proportional to the area of that loop. If the area is small, the material is said to be magnetically *soft*. If the area is large, the material is said to be magnetically *hard*. A magnetic material is considered soft when its coercive field strength is of the order of or lower than the earth's magnetic field (about 40 A/m) at room temperature [33]. Soft materials have small anisotropy

Metals	$M_s(10^6$ A/m)	A (10^{11} J/m)	Δ (nm)	K_1 (J/m^3)
Co	1.445	3.00	4.78	5×10^5
Fe	1.752	2.10	3.30	4.84×10^4
Ni	0.484	0.86	5.29	-5.7×10^3
Py	0.860	1.30	7.64	1.3×10^{-11}

Table 1.1. Magnetic parameters for band-ferromagnets Co [25], Fe [25], Ni [25], and Py [32]: saturation magnetization M_s, exchange stifness A, Bloch wall-width Δ, and magnetocrystalline anisotropy constant K_1.

constant value K_1, which make them easy to magnetize. Low magnetostriction is often desirable so that internal strains will not induce a local anisotropy energy. Permalloy ($Ni_{80}Fe_{20}$: Py), which has a vanishing value of the anisotropy constant K_1, is an example of a soft ferromagnetic alloy. However, it is still unclear from the fundamental point of view why it has a value of K_1 so small, while both Fe and Ni have large magnetic anisotropy energy [32]. In Table 1.1, a review of the main parameter of typical band-ferromagnet can be found.

1.2.2 Proximity effect at S/N interface

In this Section, the transport through a SNS JJ is discussed. The understanding of this key structure is essential for the study of the conduction mechanism through a S/F interface, where F is typically a ferromagnetic metallic barrier. When a superconductor is in contact with a Normal metal (N), the Cooper pairs penetrate across the S/N interface at some distance inside the metal, thus inducing superconducting properties. This is the so-called *proximity effect*. From a phenomenological perspective, the proximity effect at the S/N interface can be described in the framework of the Ginzburg-Landau (GL) theory. The transition between the superconducting phase to the normal state is a second-order phase transition. In absence of external field, the order parameter Ψ depends only on space variables. The parameter Ψ assumes its maximum value 1 well inside S and vanishes inside N [34]. At the S/N interface, a continuous variation of the order parameter between the two phases is observed along the distance z from the interface. Imposing the above boundary conditions and solving the 1-D linearized GL equation $-\xi_N^2 \frac{d^2\psi}{dz^2} + \psi = 0$, we obtain a decaying solution for the order

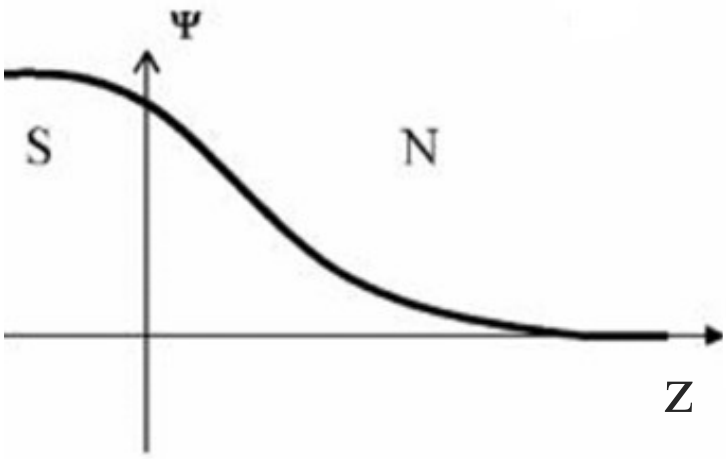

Figure 1.10. Schematic behavior of the superconducting order parameter at the S/N interface. The continuity of the order parameter at the interface implies the absence of the potential barrier. In the general case, at the interface the jump of the superconducting order parameter occurs [35].

parameter [35]:

$$\psi = \psi_0 \exp^{-z/\xi_N(T)}, \tag{1.31}$$

where the coherence length ξ_N is the characteristic decay length of ψ in the normal metal (Fig. 1.10). The coherence length ξ_N depends on the temperature as $\xi_N^2 \propto \frac{1}{1-t}$ with $t = T/T_c$ [34]. Rigorous calculations based on the microscopic theory give the following results for the coherence length ξ_N [36]. If the metal N is clean, i.e., if the mean free path l_N is large compared to the coherence length ($l_N > \xi_N$), the coherence length is:

$$\xi_N(c) = \frac{\hbar v_F}{2\pi k_B T}, \tag{1.32}$$

where v_F is the Fermi velocity and k_B is the Boltzmann constant. In the dirty limit ($l_N < \xi_N$), the leakage of the Cooper pairs is controlled by diffusive processes and it is convenient to introduce the diffusion coefficient $D_N = \frac{1}{3} l_N v_N$. In this limit, the coherence length is:

$$\xi_N(d) = \sqrt{\frac{\hbar D_N}{2\pi k_B T}} = \sqrt{\frac{l_e}{3}\xi_N(c)}. \tag{1.33}$$

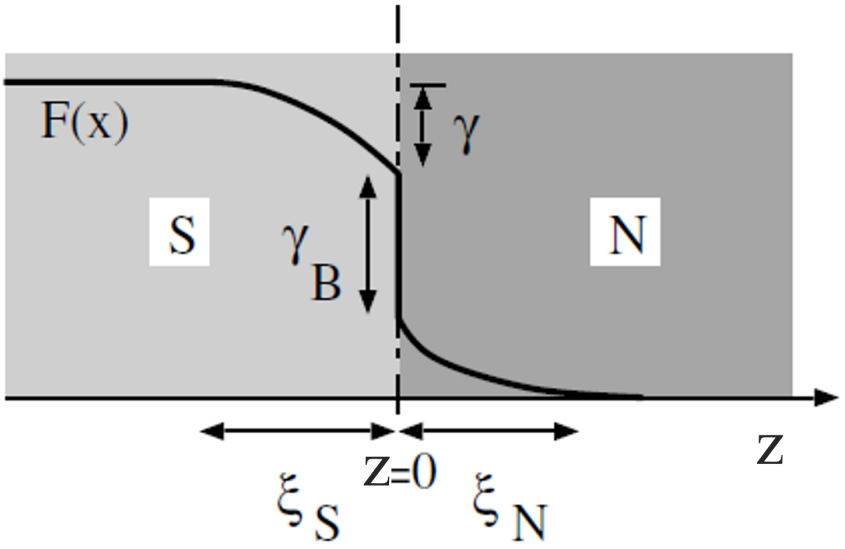

Figure 1.11. Schematic illustration of the spatial dependence of the Cooper pair density $F(z)$ at an S/N interface boundary [38]. γ and γ_B represent the proximity strength and the interface transparency, respectively.

Typical values for ξ_N are in the range of $10 - 100$ μm [2].

Kupriyanov and Lukichev succeeded in deriving boundary conditions for the proximity effect at S/N interface [37], by introducing two parameters that quantify the proximity strength:

$$\gamma = \frac{\rho_S \xi_S}{\rho_N \xi_N} \tag{1.34}$$

and the interface transparency:

$$\gamma_B = \frac{R_B}{\rho_N \xi_N}. \tag{1.35}$$

Here, R_B is the resistance for unit area of the S/N interface, whereas $\rho_{S,N}$ are the normal state resistivity of S and N materials, respectively. As shown in Fig. 1.11, γ_B determines the jump in the Cooper pair density $F(z)$, while γ is a measure of the suppression of $F(z)$ in the superconductor near the interface [38].

As a result of this coupling, the DOS in an SN sandwich differs significantly from the DOS of a bulk superconductor (Fig. 1.12). At the S/N interface, the maximum of the DOS around Δ_S is widened and lowered if the coupling between the layers is enhanced by decreasing γ_B. At the free surface of the N layer, a gap Δ_N is developed in the DOS owing to the coupling to the superconductor. This

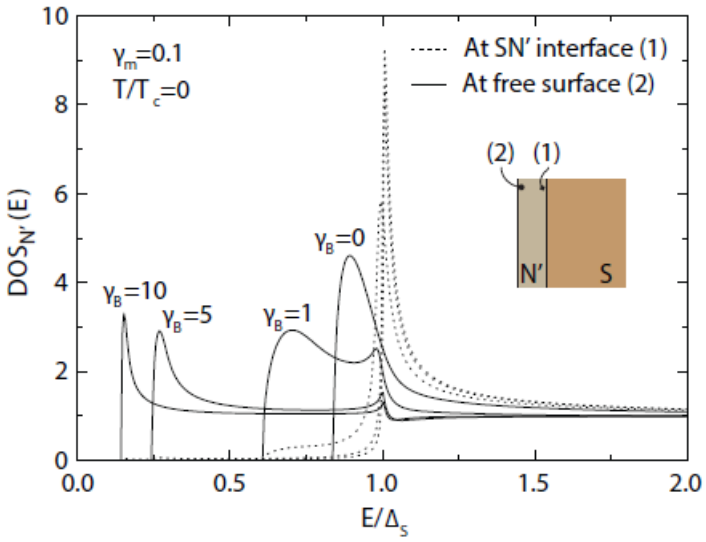

Figure 1.12. DOS in a thin N layer ($d_N \ll \xi_N$) of an SN sandwich normalized to the normal-state value at the free surface (solid lines) and at the SN boundary (dashed lines) for $\gamma_m = \gamma d_N/\xi_N = 0.1$ and for various values of γ_B [38, 39].

energy gap approaches the gap of the superconductor Δ_0 if γ_B is decreased. Near the S/N interface, the DOS in the N layer has an induced maximum below the gap of the superconductor. This maximum is shifted towards zero if the distance from the interface is increased [38, 39].

The microscopic mechanism that allows the transfer of a Cooper pair from S to N (and vice versa) is the *Andreev reflection* and it is sketched in Fig. 1.13 [40]. An incoming electron at energy reaching the S/N interface cannot penetrate directly the superconductor if its energy is smaller than the superconducting energy gap ($\epsilon < \Delta$). In contrast of being reflected, it drags along a second electron at energy $-\epsilon$, with opposite momentum and spin, to enter the superconductor as Cooper pair. This second electron is taken from the valence band and consequently leaves a hole behind. This hole travels back along the path of the original coming electron because it has opposite direction of momentum. The reverse mechanism takes place as well. In this case, the incoming quasiparticle is a hole in the valance band (energy $-\epsilon$), which upon arriving at the interface pulls a Cooper pair out of the condensate. One of the electrons occupies the hole, while the other electron occupies an excited state in the conduction band and travels back along the path

of the original incoming hole. The net result of an Andreev reflection is thus a charge transfer of $-2e$ from N to S (Fig. 1.13a). The Andreev reflection is

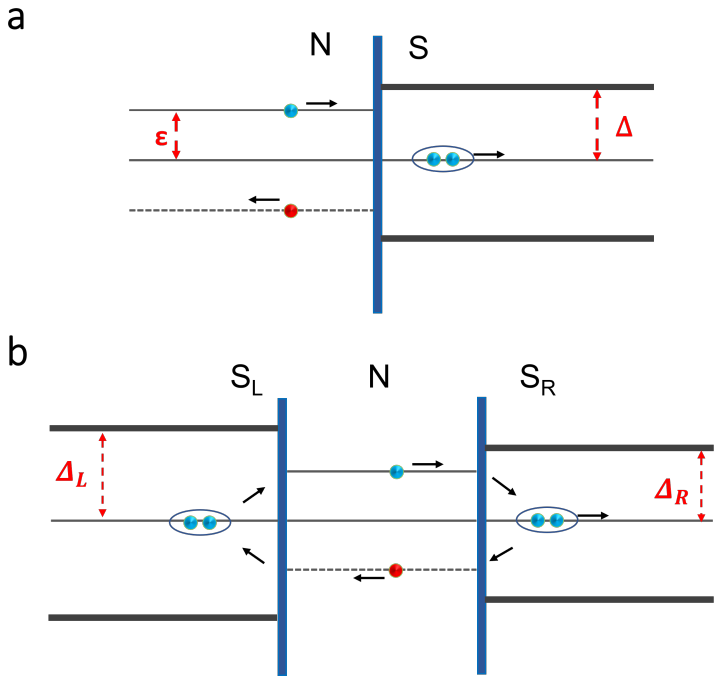

Figure 1.13. Andreev reflection (a) at S/N interface and (b) in a SNS JJ.

the primary mechanism for Cooper pairs to be transferred across a SNS JJ. An electron approaching one of the interfaces is converted into a hole moving in the opposite direction, thus generating a Cooper pair in a superconductor. This hole is consequently Andreev reflected at the second interface and is converted back to an electron, leading to the destruction of a Cooper pair (Fig. 1.13b). As a result of this cycle, a pair of correlated electrons is transferred from one superconductor to another creating a supercurrent flow across a junction [6].

In Fig. 1.14, we show the temperature dependence of the critical current $I_c(T)$ in SNS JJs theoretically predicted by Likharev, as the function of the ratio t/ξ_N, where t is the length of the barrier [41]. For low value of t/ξ_N, the $I_c(T)$ curve shows a down-ward concavity and is similar to those expected in tunnel JJs. According to Ambegaokar-Baratoff (AB) theory, the temperature dependence of the critical current in standard SIS JJs is related to the Bardeen-Cooper-Schrieffer

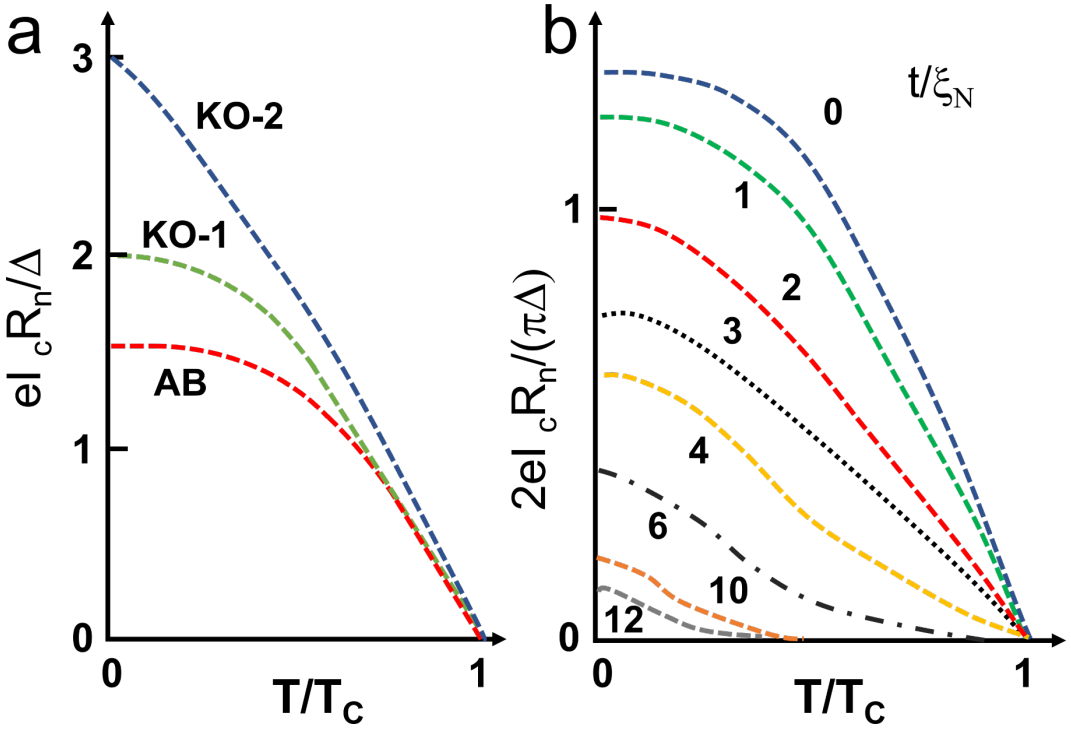

Figure 1.14. (a) $I_cR_N(T)$ in the AB (dashed red line), KO1 (grey dashed line) and KO2 (blue continuous line) limits, respectively. (b) $I_cR_N(T)$ is reported in units normalized to the gap value Δ as a function of the temperature T, for different values of the ratio between the barrier length t and ξ_N [5].

(BCS) energy gap $\Delta(T)$ of the superconducting electrodes:

$$I_c(T) = \frac{\pi}{2eR_N}\Delta(T)\tanh\left(\frac{\Delta(T)}{2k_BT}\right), \tag{1.36}$$

which saturates at $\frac{\pi}{2eR_N}\Delta(0)$ [42]. In point-contacts JJs, the values of $I_c(T)$ at $T \to 0$ K are higher than the one expected by the AB theory. In the dirty limit (KO1 theory), the saturation at low temperatures occurs at a value 32% larger than in SIS JJs, whereas in the clean limit (KO2 theory) at a value 50% larger than in SIS JJs [41]. In SNS JJs the K01 limit is found for $t/\xi_N = 0$. For high values of t/ξ_N, at the lowest T there is a saturation of I_c, while I_c has a characteristic exponential dependence for $T \to T_c$. These two regions are connected at intermediate T by a curve with up-ward concavity (see Fig. 1.14). The tail of the exponential decay and the width of the intermediate region essentially depend on t/ξ_N. Finally, in the long-junction limit ($L \gg \xi_N$), the $I_c(T)$ shows a fully exponential trend.

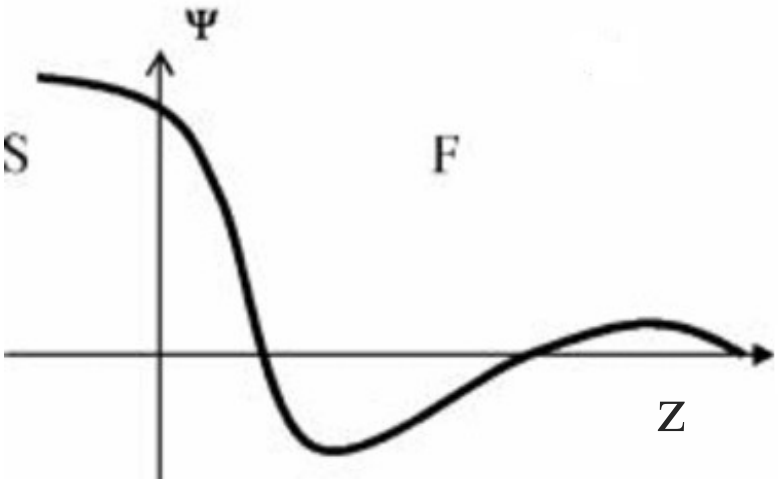

Figure 1.15. Schematic behavior of the superconducting order parameter at the S/F interface. The continuity of the order parameter at the interface implies the absence of the potential barrier. In the general case, at the interface the jump of the superconducting order parameter occurs [35].

1.2.3 Proximity effect at S/F interface

When the normal metal is replaced by a ferromagnet, the effects of a non-zero spin polarization and of the exchange energy E_{ex} have to be included. The Andreev reflection is in this case limited by the presence of a minority spin-band. In the extreme limit of a fully spin-polarized metals, all carriers have the same spin and the Andreev reflection is totally suppressed [35]. Moreover, the induced electron-hole pair experiences the exchange splitting of the spin-bands in the ferromagnet. As a result, the spin-up electron decreases its potential energy by E_{ex}, while the spin-down electron potential energy increases by the same value. To compensate this energy variation, the spin-up electron increases its kinetic energy, while the spin-down electron decreases its kinetic energy. Thus, the Fermi momentum of the electron with spin ($\uparrow$) will shift from $+k_F$ to $k_1 = k_F + \delta k_F$, with $\delta k_F = \frac{\mu_B H_{ex}}{v_F}$. Similarly, the Fermi momentum of the electron with spin ($\downarrow$) will shift from $-k_F$ to $k_2 = -k_F + \delta k_F$. As a result the Cooper pair acquires a center-of-mass momentum $k_1 + k_2 = 2\delta k_F \neq 0$, which implies the modulation of the order parameter with a period $\pi v_F / E_{ex}$. The direction of the modulation wave vector must be perpendicular to the interface, because only this orientation allows a uniform order parameter in the superconductor [35]. In the framework

of the GL theory, it can be demonstrated that ψ assumes the form [35]:

$$\psi = \psi_0 \exp\left(-\frac{z}{\xi_{F1}}\right) \cos\left(-\frac{z}{\xi_{F2}}\right), \tag{1.37}$$

where $\xi_{F1} \propto \left(\sqrt{1+\frac{T-T_{ci}}{T-T_{cu}}}-1\right)^{-1/2}$ and $\xi_{F2} \propto \left(\sqrt{1+\frac{T-T_{ci}}{T-T_{cu}}}+1\right)^{-1/2}$. T_{cu} is the transition temperature of the system into the uniform superconducting state and T_{ci} the transition temperature of the system into the non-uniform superconducting state [35]. Thus, the decay of the order parameter in the F layer is then accompanied by its oscillation, which is a characteristic feature of the proximity effect in SF systems (Fig. 1.15).

In real ferromagnets, the exchange field is large compared to the superconducting temperature and energy scales, and as such the gradients of the superconducting order parameter variations are also large, and cannot be treated with the generalized GL functional. To describe relevant experimental situations, a microscopical approach is needed. The most convenient scheme is the Bogoliubov–de Gennes equations or the Green's functions using the quasiclassical Eilenberger or Usadel equations [35]. In the clean limit, the coherence length ξ_F:

$$\xi_F(c) = \frac{\hbar v_F}{2(\pi k_B T + iE_{ex})}, \tag{1.38}$$

whereas in the dirty limit:

$$\xi_F(d) = \sqrt{\frac{\hbar D_F}{2(\pi k_B T + iE_{ex})}} = \sqrt{\frac{l_F}{3}\xi_F(c)}, \tag{1.39}$$

where $D_F = \frac{1}{3} l_F v_F$ is the diffusion coefficient of the ferromagnet and l_F is the mean-free path of the F layer. In the dirty case, $\xi_{F1}(d) \simeq \xi_{F2}(d) \simeq \sqrt{\hbar l_e v_F / 3E_{ex}}$ are of order of 1 - 10 nm. On the other side, in the clean case the two scales are different: $\xi_{F1}(c) \simeq \frac{\hbar v_F}{2\pi k_B T}$ is long as ξ_N, and $\xi_F(c) \simeq \frac{\hbar v_F}{2E_{ex}}$ is short.

Because of these oscillations, different signs of the order parameter can occur at the two S banks when the F layer thickness d_F is of the order of an half period. This is the so-called π-phase state, which competes for existence with

the ordinary 0-phase state. The $0-\pi$ phase transition can manifest itself in a non-monotonous thickness dependence both of the superconducting transition temperature T_c [43, 44, 45] and of the critical current [46, 47, 48, 49] I_c in SFS JJs. A dominant second harmonic in the current phase relation has been manifested as half-integer Shapiro steps [45] and as magnetic interference patterns with half the expected period [50].

Finally, spin-triplet pairing can be generated by introducing some magnetic non-collinearity at the S/F interface, e.g, spin-mixer layers [51, 52]. Thus, in magnetic JJs containing complex ferromagnetic multilayers, triplet pairs are immune to pair breaking by the exchange field in F and the coupling between S and F layers is enhanced on anomalously long scaling lengths [53, 54].

From an application point of view, a crucial advantage of MJJs compared to standard SIS JJs stands in their behavior in presence of a magnetic field H. In JJs containing a F barrier, to evaluate the total magnetic flux through the junction Φ, the flux due to the F magnetization M_F must be considered: $\Phi_F = \mu_0 M_F L d_F$, with L the cross-section width of the JJ and d_F the F thickness. Hence, the total magnetic flux through the junction is $\Phi_F = \mu_0 H L d_m + \mu_0 M_F L d_F$, where the thickness of the material penetrated by the applied field is $\mathrm{d}_m = 2\lambda_L + \mathrm{d}_F$ [55]. Because of the magnetic hysteresis of the F layer, the $I_c(H)$ curves acquire a magnetic hysteresis depending on the sweeping direction of H. The $I_c(H)$ curves are shifted in field to a point where the flux due to the external field cancels out the flux due to the magnetization. As a result, sweeping H from positive to negative fields (*down curve*), the Fraunhofer-like pattern is expected to be shifted at a negative field, because of the positive remanence of the ferromagnet, whereas when the field is swept from positive to negative fields (*up curve*), it is shifted at a positive field (Fig. 1.16). Thus, in the simplest case of a homogeneous F barrier in a single-domain state, we can assume that $\mu_0 M_F = \mu_0 M_s \sim \mu_0 M_r$ and the Fraunhofer pattern is simply offset by a factor:

$$\pm\mu_0 H_{shift} = \mp\frac{\mu_0 M_s d_F}{d_m}. \tag{1.40}$$

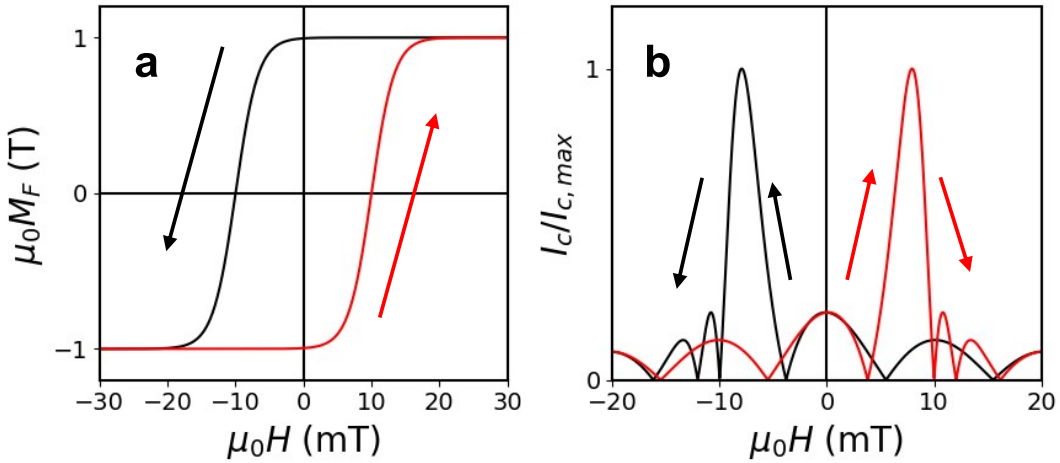

Figure 1.16. (a) For a JJ containing a F layer characterized by a magnetization curve *M(H)*, (b) the $I_c(H)$ curve is expected to be shifted depending on the sweeping field direction.

From the $I_c(H)$ curves, we can derive information on the magnetization process of F barrier. In rectangular JJs, the minima and maxima of the critical current are determined by the following relations:

$$\begin{cases} \Phi_{min} = \Phi_0 m \\ \Phi_{max} = \Phi_0 \left(n + 1/2\right) \end{cases} \tag{1.41}$$

where m and n are two integers. Using Equation 1.41, it is possible to evaluate the values of $\Phi(H)$ corresponding to the minima and maxima of $I_c(H)$: in correspondence of these values, the flux due to the external field is determined. Subtracting this contribution to the total flux, we obtain the flux due to F magnetization and hence the *M(H)* dependence. This procedure is called *Josephson magnetometry* [55, 56] and provides a powerful tool to investigate novel phenomena at the S/F interface, as discussed in detail in the the Chapter 3.

1.3 SIsFS JJs

Standard SFS JJs typically present an overdamped regime because of the standard metallic nature of the F barrier. However, a proper coupling of ferromagnetic layers with insulating barriers inside the JJs (SIsFS or SIFS JJs) allows to en-

gineer ferromagnetic JJs characterized by high quality factors and underdamped behavior [57].

Properties of SIsFS structures can be discussed in the framework of a microscopic model proposed in Ref. [58, 59], which mainly assumes the dirty limit for the involved materials and an arbitrary finite transparency for the bilayer interface, which is assumed identical for both sF and FS interface and is characterized by the parameters γ and γ_B (Equation 1.34 - 1.35). Under the above conditions the Josephson effect in the SIsFS junctions can be described by solving the U-sadel equations with Kupriyanov-Lukichev boundary conditions at Is, sF, and FS interfaces and by assuming a bulk pair potential in the depth of S electrodes. In Fig. 1.17, the dependence of the I_cR_N product on the ratio of the s and F thicknesses over their respective coherence lengths is shown. Basically, three operation modes can be distinguished by comparing the s thickness d_s with the critical thickness d_{sc}, i.e., the minimal thickness of the s layer in a sF bilayer above which superconductivity still exists at a given temperature [59].

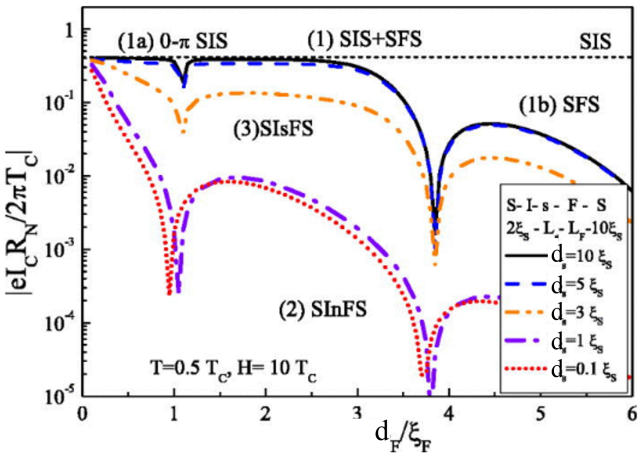

Figure 1.17. Characteristic voltage I_cR_N of the SIsFS structures versus thickness of the F layer d_F for different thicknesses of the middle superconducting film d_s at $T = 0.5\ T_c$. Short-dashed straight line shows the I_cR_N product of the tunnel SIS junction at the same temperature. Interface parameters: $\gamma_{BI} = 1000$, $\gamma_{BFS} = 0.3$ and $\gamma = 1$ at the sF and FS interfaces [59].

- **Mode 1:** If $d_s \gg d_{sc}$, the pair potential in the s layer Δ is close to that of the bulk material and the SIsFS structure can be considered as a series of a tunnel SIs JJ and a ferromagnetic sFS JJ.

(a) For small d_F and for the ordinary case in which $I_{c,SIs} \ll I_{c,sFS}$, then the I-V curve of the overall SIsFS device is determined by its SIs part and the I_cR_N product can reach its maximum value corresponding to a standard SIS JJ. At the same time, the phase difference φ in the ground state of an SIsFS junction is controlled by the sFS part. As a result, both 0 and π states can be achieved depending on the thickness of the F layer d_F.

(b) For large d_F value, the structure transforms into a standard SFS junction without any influence of the barrier.

- **Mode 2:** If $d_s < d_{sc}$, the absence of superconductivity in the s interlayer leads to a formation of the complex-InF-weak link area, where n marks the intermediate s film in the normal state. It results in I_cR_N values of the order of SIFS JJs.

- **Mode 3:** If $d_s \sim d_{sc} \sim 3\xi_s$, the properties of the structure are very sensitive to d_F and the exchange field of the F layer, since these parameters control the suppression of superconductivity in the sF bilayer. The latter tunes the effective transition temperature T_c^*, which is the transition temperature of the sF interlayer leading to the appearance of a proximity-like tail in the $I_cR_N(T)$ dependence (Fig. 1.18).

If $d_s < \lambda_L$, the whole structure behaves as a single junction with respect to an external magnetic field H, since d_s is too thin to screen the magnetic field. When the SIsFS junction is in mode (1a) and far from the 0 -π transition, the current-phase relation has a standard sinusoidal form (Equation 1.1). Thus, in a rectangular JJs we still observe a Fraunhofer-like dependence of the $I_c(H)$ curves. In this case, the total magnetic flux through the junction becomes [57]:

$$\Phi = \mu_0 M_F L d_F + \mu_0 H L d_m \tag{1.42}$$

where the thickness of the material penetrated by the applied field is $d_m = 2\lambda_L + d_s + d_F + d_I$ [57]. As it will be addressed throughout this thesis, this operating

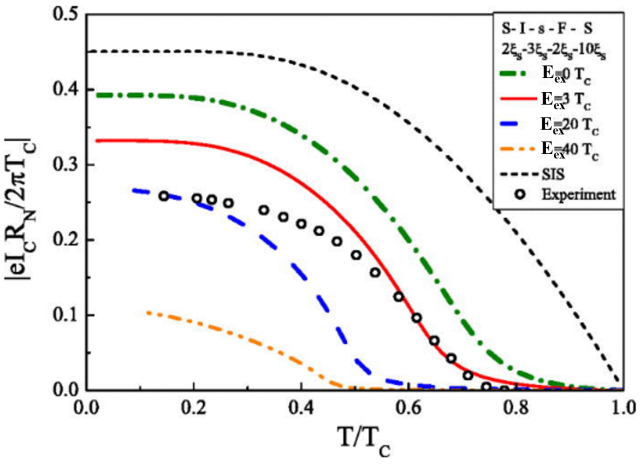

Figure 1.18. The temperature dependence of characteristic voltage I_cR_N of SIsFS structure in the mode 3 for different values of exchange field E_{ex} in the F layer. The circles show I_cR_N measured in Nb-Al/AlO_x-Nb-$Pd_{0.99}Fe_{0.01}$-Nb junctions [60].

regime opens the possibility to realize switchable elements characterized by high quality factor and low-dissipation, which can provide additional functionalities both in digital and quantum superconducting electronics.

Chapter 2

Scalable tunnel magnetic Josephson Junctions

In this Chapter, we discuss in detail our approach to realize scalable tunnel SIsFS JJs with a strong ferromagnetic alloy $Ni_{80}Fe_{20}$ (Permalloy: Py). We have investigated the role of the F and s layer thickness and we have designed these JJs in order to fall into the tunnel limit, while preserving the two-magnetic state behavior of the critical current. To our knowledge, these JJs are the smallest SIsFS memory elements ($\sim 7\mu m^2$) compatible in speed and power dissipation with Single Flux Quantum (SFQ) circuits. In the framework of quantum computing, SFQ cryogenic technology provides supporting functions for superconducting qubit circuits such as read-out, control, and error-correction. Moreover, given the stability of magnetic properties of Py, in principle, there are no limitations in further reducing the cross-section of the JJs down to submicron dimensions.

2.1 State of the art

A ferromagnetic barrier in a JJ generates novel physics, but also is the key for technological advances in fields ranging from digital to quantum electronics. Recently, interest in ultra-low-power, high-density cryogenic memories has spurred new efforts to simultaneously exploit superconducting and magnetic properties to create novel switching elements having these two competing order parameters [61]. The possibility to use SFS JJs as unit cells in Random Access Memory (RAM) has been demonstrated in Nb/PdFe/Nb junctions [55]. In these memory elements, below the saturation field of the F layer, there are two critical current levels, which can correspond to the two memory states. The switch between the two memory states can be performed by applying magnetic field pulses. A magnetic field bias is usually applied to set the optimal working point, i.e., the field at which the difference between the higher and lower critical current levels ΔI is as large as possible. If the initial state is the '0' state, the memory can be switched to the '1' state upon application of a positive magnetic field pulse. In the rising edge of the pulse, the critical current moves along the up curve. On the falling edge of the pulse, the critical current follows the down curves, and, after the pulse, the junction ends up in the '1' state (Fig. 2.1a-b). Read operations are performed using a d.c. current I_R that is intermediate between the two critical current values corresponding to the logic states '0' and '1'. If I_R is larger than the critical current level, than the output signal is a finite voltage, while if I_R is smaller than the critical current level of the logic state then the output signal is a zero voltage (Fig. 2.1a-c) [55, 62].

Since then, several approaches have been proposed, including the use of φ-junctions [63], MJJs with a pseudo-spin valves as weak link [54, 64, 65, 66], and multi-terminal Josephson devices [67]. However, the characteristic frequency of a JJ switching process $\omega_c = (2\pi/\Phi_0)\, I_c R_N$ is determined by the $I_c R_N$ product and it is typically too low in devices based on standard metallic SFS. Indeed, SFQ logic, the main JJ technology for digital and mixed signal circuits [68], predominately relies on tunnel SIS JJs whose $I_c R_N$ product is in the range 0.2 - 0.7 mV

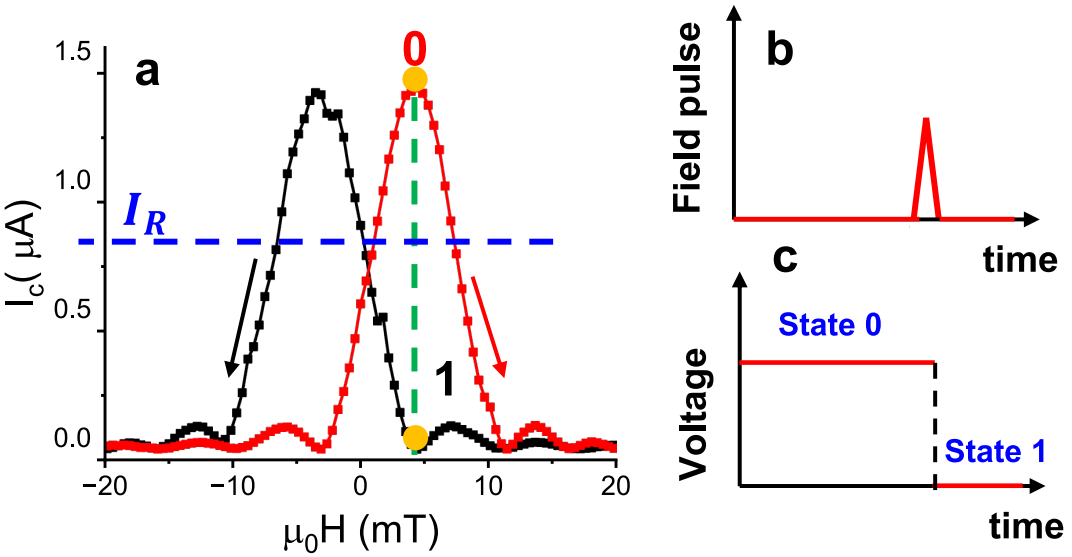

Figure 2.1. Functioning scheme of a MJJ memory element. (a) $I_c(H)$ curve: black and red arrows indicate the sweeping direction of the magnetic field to obtain the corresponding curve. Green vertical line corresponds to the field to set the optimal working point. Blue horizontal line corresponds to the reading current I_R. Orange dots indicate the memory states. (b) Scheme of the pulses used to switch between logic states. (c) Voltage levels corresponding to the two logic states.

resulting in high characteristic frequency $\omega_c/2\pi \approx 100 - 350$ GHz [61].

Nevertheless, the situation can be improved by inserting an additional insulating barrier and superconducting interlayer resulting in a SIsFS stack. The demonstration of tunnel JJs SIsFS-based memory elements with characteristic voltage levels compatible with the standard SFQ circuits have been reported in Ref. [57]. These junctions have been realized using standard Nb/Al technology, with a 10 μm $\times$ 10 μm area, and a magnetically soft $Pd_{0.99}Fe_{0.01}$ as F layer. $Pd_{0.99}Fe_{0.01}$ allows a low-energy and high-speed switch of the JJs [69], but it is not suitable for the realization of devices with reduced area, due to a percolative nature of the exchange interaction between iron atoms, which can result in frustrated magnetic properties when reducing the dimensions [70].

More generally, the use of a magnetically weak F layer, i.e., a ferromagnet with low value of the exchange energy and thus of the magnetization, poses limitations on the scalability of MJJ as switchable elements. Upon the application of magnetic pulses, the Josephson critical current changes and retains its value because of the residual flux due to the F magnetization Φ_r. The residual magnetic flux

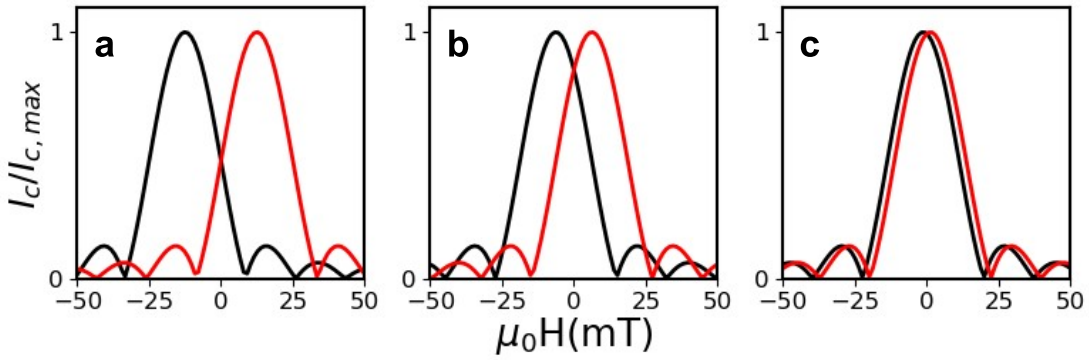

Figure 2.2. Simulated $I_c(H)$ curves for a circular JJs with radius $R = 250$ nm and a 3-nm-thick layer (a) with $\mu_0 M_F = 1$ T, (b) $\mu_0 M_F = 0.5$ T, and (c) $\mu_0 M_F = 0.1$ T. The black curves are obtained by sweeping H from positive to negative fields (down curves), whereas the red curves are obtained from negative to positive fields (up curves).

Φ_r is determined by the product of the residual magnetization M_r, the magnetic layer thickness d_F, and the size of the SIsFS junction L. The latter means that Φ_r goes to zero with the decrease in L and small value of M_r. Therefore, square shaped MJJ with weak F barrier ($\mu_0 M_r \sim 0.1$T for $Pd_{0.99}Fe_{0.01}$) cannot be decreased down to nanoscale since ΔI disappears (Fig. 2.2). Recently, to deal with this issue it has been proposed to use rectangular shaped SIsFS: in this case, the value of critical current is defined by the orientation of magnetic moment at zero magnetic field [71, 72].

2.2 Materials and fabrication of SIsFS JJs

2.2.1 Magnetic characterization of Py films

In view to scale square shaped JJs down to submicron dimensions, strong ferromagnets with significant high remanent magnetization and in-plane anisotropy are required to distinguish the two-critical current states. For thin ferromagnetic films the easy axis of the magnetization usually is parallel to the film plane to minimize the magnetostatic energy contribution due to the shape anisotropy (Section 1.2.1) [28]. However, an out-of-plane anisotropy has been observed for Co/Ni multilayer [73], CuNi [74], PdNi [75] and Co alloy [76], which prevents the shift of the $I_c(H)$ curves. Nevertheless, the requirements listed above can be satisfied using NiFe alloys, which show also desirable switching properties with

relatively low coercive fields [77, 66].

To get information on the direction of the easy axis of our Py films, we have recorded the magnetic moment m versus applied magnetic field H of a 3-nm-thick Py layer within a Nb/ AlO_x/Nb/Py/Nb multilayer (10 mm $\times$ 10 mm). We have performed the measurements by using a Vibrating Sample Magnetometer (VSM) at a temperature $T = 12$ K, i.e., above the critical temperature of the Nb films, in order to measure just the response of the Py layer (Fig. 2.3a).

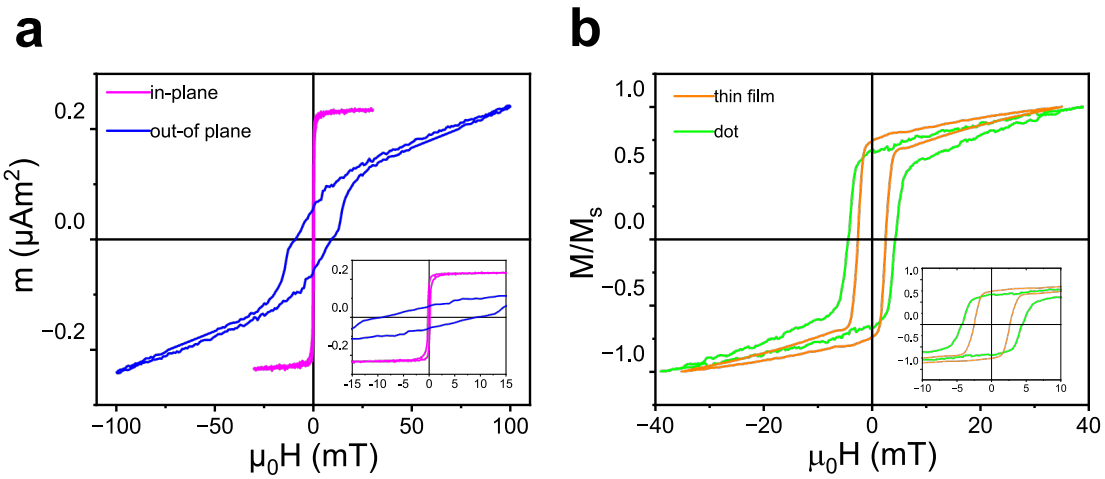

Figure 2.3. (a) Magnetic moment m versus applied magnetic field H of a 3-nm-thick Py layer within a Nb/ AlO_x/ Nb/Py/Nb multilayer (10 mm $\times$ 10 mm) by applying the magnetic field in-plane (pink curve) and out-of-plane (blue curve). (b) Hysteresis loops of a 7-nm-thick, plain Py film (orange line) and of a Py square dot with lateral size of 10 μm (green line) at $T = 12$ K.

An almost rectangular shaped *m(H)* curve is expected for the field applied along the easy axis because the magnetization tries to stay along this preferred direction as long as possible, and then abruptly switches to the opposite direction at the coercive field. In contrast, for the field applied along the hard axis the magnetization is expected to be gradually rotated out of the easy axis direction into the hard axis direction by increasing the applied magnetic field. As shown in Fig. 2.3a, the measured *m(H)* curve is much more rounded and has smaller remanent magnetic moment when the field is applied out-of-plane, whereas it has an almost rectangular shape when the field is applied in-plane. This is clear evidence for an in-plane anisotropy of our films [26]. From Fig. 2.3a, we have estimated a value of the saturation magnetization $\mu_0 M_s \simeq 1$ T that is in agreement with previously

published data [78]. The slight deviation from the bulk value (order of percent) suggests that the dead layer at the S/F interface is almost negligible.

To investigate the effect of patterning of the films on magnetic properties, square Py dots with a lateral size of 10 μm and thickness of 7 nm have been realized by lithography and lift-off technique on Si/SiO_2 wafer. The elements have been arranged on a square lattice with a period of 30 μm so that the dipolar interaction between them is negligible. In this way, the measured hysteresis loop of the overall array is the superposition of the magnetization loop of a single element [79]. We observe an increase up to an order of magnitude of the coercive field for Py films grown directly on Si substrates with respect to the ones grown on the bottom Nb film. An influence of the substrate on the F film is expected in view of elastic strains, surface anisotropy, or magnetostatic interactions [80]. Nevertheless, an increase of only about a factor two of the coercive field with respect to the continuous 7-nm-thick Py film is observed (Fig. 2.3b). Therefore, this preliminary study allows us to conclude that Py is a good candidate for the realization of JJs with reduced area, guaranteeing relative low saturation and coercive fields.

2.2.2 Estimation of the coherence lengths

As illustrated in the Section 1.3, the behavior of tunnel SIsFS strongly depends on the thicknesses of the s interlayer and of the F barrier, which have to be compared to their respective coherence lengths [58, 59]. Therefore, to discuss the transport properties of our JJs within their proper framework, we have first estimated the coherence length of our thin films.

The superconducting GL coherence length at zero temperature $\xi_{GL}(0)$ can be evaluated from the linear temperature of the perpendicular upper critical field [34]:

$$\mu_0 H_{c2\perp}(T) = \frac{\Phi_0}{2\pi\xi_{GL}^2(0))}\left(1 - \frac{T}{T_C}\right). \tag{2.1}$$

In order to obtain the temperature dependence $H_{c2\perp}(T)$, for a 400-nm-thick Nb Nb layer the resistance has been measured as a function of the temperature T at fixed applied field perpendicular to the film. $H_{c2\perp}$ has been defined as the field at

which the resistance value is the 90% of the normal resistance evaluated at $T =$ 10 K. For our samples, $\xi_{GL} \simeq 10$ nm implies a superconducting coherence length $\xi_S(0) \simeq 7$ nm [81].

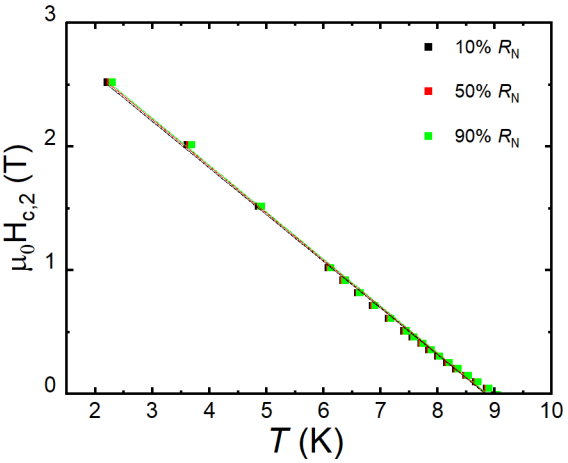

Figure 2.4. Temperature dependence of the upper critical perpendicular field $H_{c2\perp}(T)$ for a 400-nm-thick Nb layer determined by using three different resistive criteria. $H_{c2\perp}$ has been defined as the field at which the resistance value is the 10% (black dots), 50% (red dots) and 90% (green dots) of the normal resistance R_N evaluated at $T = 10$ K.

To estimate the coherence lengths ξ_F, we have measured the resistivity of a 3-nm-thick Py layer by using a four-probe in-line technique and we have found ρ_{Py} = 84 $\mu\Omega$cm. Thus, the diffusion coefficient D_F can be obtained via relations $D_F = \frac{v_F l_F}{3}$ and $\rho l_F = 31.5 \times 10^{-6} \mu\Omega\text{cm}^2$ [82]. For Py, $v_F = 2.2 \times 10^5$ ms^{-1} and $E_{ex} \simeq 200$ meV [49], substituting in Equation 1.39, we obtain $\xi_F(0) = \simeq 1$ nm, in agreement with the values reported in literature [49].

2.2.3 Fabrication of SIsFS JJs

To investigate the tunnel properties of SIsFS JJs with Nb as S layer and Py interlayer as F barrier, we have decided to prepare two sets of SIsFS JJs with two different s thicknesses:

1. Nb (200 nm)/Al-AlO$_x$/Nb (10 nm)/Py (3 nm)/Nb (350 nm) JJs,

2. Nb (200 nm)/Al-AlO$_x$/Nb (30 nm)/Py (3 nm)/Nb (350 nm) JJs.

As reference, we have also fabricated standard SIsS JJs from the same wafer by excluding the F layer deposition step. The lithography steps are outlined in the

following. For further details on the sputtering systems, we refer to Appendix A.1.

I lithography step: Defining the geometry of the bottom contact

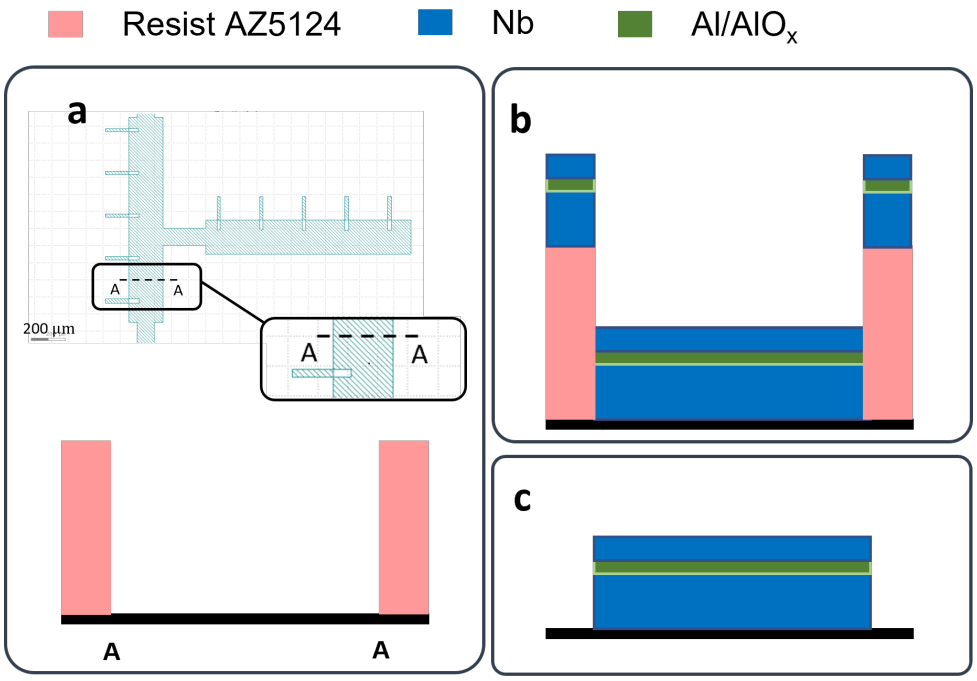

Figure 2.5. (a) Definition of the geometry of the bottom electrode, (b) deposition of the trilayer, and (c) lift-off.

After spinning a HMDS-primer and AZ5214 photoresist onto oxidized 3-inch Si wafers, we have defined the geometry of the bottom contact by optical lithography (Fig. 2.5a). After the resist development procedure, a Nb/Al-AlO$_x$/Nb trilayer has been deposited by DC magnetron sputtering in an ultra-high vacuum chamber (Fig. 2.5b). Before each deposition, a pre-sputtering operation is carried out far from the wafer-device, thus cleaning the target surface from impurities accumulated during the loading and unloading operations of the samples. The base Nb layer having a thickness of 200 nm has been deposited by DC sputtering at a rate of 1.2 nm/s by using argon (Ar) as a process gas at a pressure of 3 mTorr. The working voltage and power of magnetron have been 350 V and 300 W, respectively. To avoid any heating problems, the deposition has been carried out in two identical steps with a wait-time of 2 hours. A tunnel barrier has been

obtained by depositing in the same vacuum chamber a 7-nm-thick Al layer and by filling the chamber with dry oxygen at a pressure of 200 mTorr for 1 hour to obtain a AlO_x barrier. Afterward, a 40- or 20-nm-thick Nb layer has been deposited under the same conditions as the base layer. The lift-off procedure has been performed by dissolving the photoresist in acetone at room temperature for 2 hours (Fig. 2.5c).

II lithography step: SNAP and deposition of SiO_2 layer

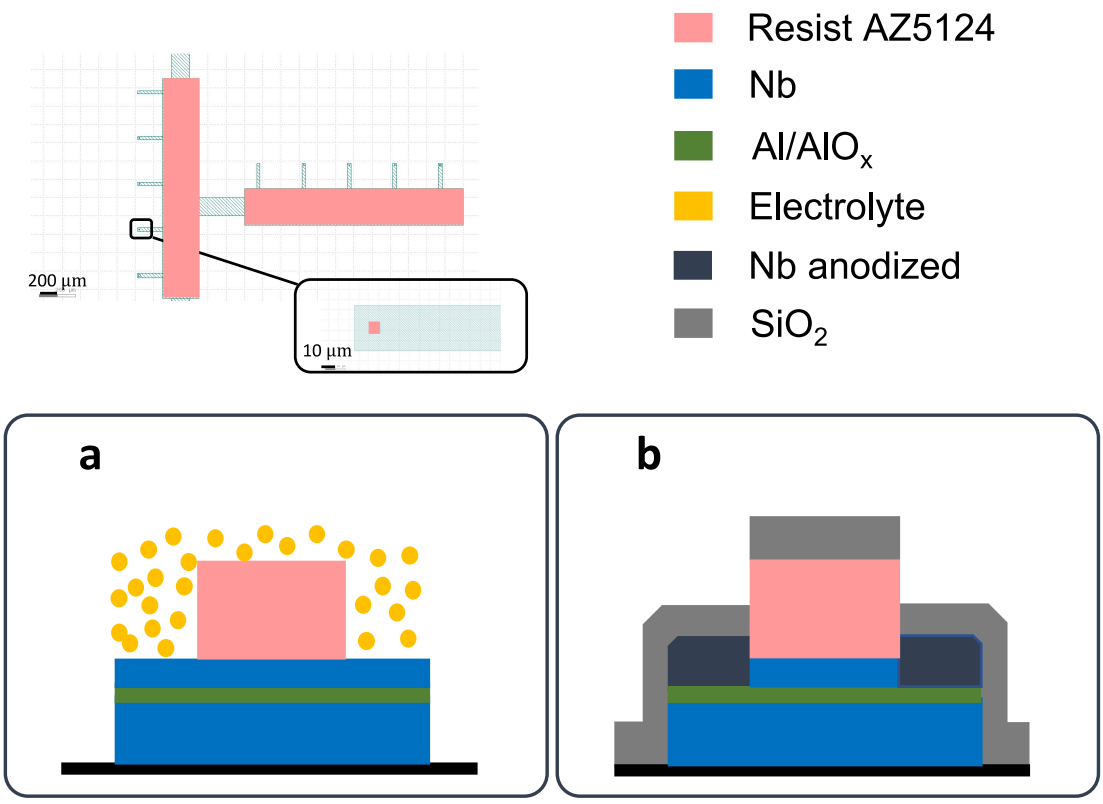

Figure 2.6. Definition of JJ area and insulation by (a) selective anodization process and (b) silicon dioxide deposition.

To define the area of JJs, we have proceeded to the so-called Selective Niobium Anodization Process (SNAP). The trilayers have been patterned by optical photolithography. The areas that will form the weak link between S electrodes and contact banks for electrical wiring have been covered with photoresist (Fig. 2.6). This photoresist is required to block the anodization of the upper electrode of the Josephson devices, as shown in Fig. 2.6a. During the anodization process, the sample has been immersed in an electrolyte solution consisting of 1 part of

deionized water, 1.5 parts of glycoethylene and 20 g of ammonium pentaborate per 100 ml of deionized water. The cathode is made up of a platinum electrode, while the niobium is the only anodic conductor exposed to the electrolyte. The process has been monitored by plotting the time derivative of the voltage across the cell versus the voltage itself. With a constant current source $I \sim 100\ \mu$A, the rate of consumption of Nb is almost constant and a linear relation between cell voltage and time derivative is, thus, observed as long as Nb is being anodized. When the Nb upper electrode is completely consumed, the anodization voltage jumps relatively abruptly by an amount ΔV. The growth rate of the oxide is proportional to the current with which the anodizing cell is biased. We have set the anodization speed at 0.4 V/s corresponding to an oxide growth rate of about 0.6 nm/s. The process has been stopped when the voltage across the cell has reached 40 V, which assures that all the top niobium layer has been anodized. After the anodization process, the samples have been loaded into another high-vacuum system to deposit a further insulating layer (Fig. 2.6b). A 200-nm-thick silicon dioxide layer has been deposited in two steps by using a 2-inch magnetron powered with a RF generator at a rate of 0.5 nm/s with an Ar gas process at a pressure of 3.0 mTorr and a generator power of 150 W. This additional oxide layer guarantees better insulation and therefore reduces the subgap leakage currents improving the quality of the JJs. Again, the photoresist is dissolved in acetone at room temperature for an hour and half.

III lithography: deposition of the F layer

For the SIsFS samples, the resist has been deposited and a window has been opened at the junction area. Then, the surface of Nb layer has been cleaned by a soft etching procedure by using an ion gun. During the ion beam etching, the Ar pressure has been fixed at 3 mTorr and a power discharge of 8 W has been applied for 9 min to remove about 10 nm of Nb oxide layer, so that the effective thickness of the Nb layer is 30 nm (10 nm). After the cleaning process, the sample has been moved into an adjacent vacuum system, and a 3-nm-thick Py layer has been deposited by DC magnetron sputtering at the rate of 0.7 nm/s. Py films have

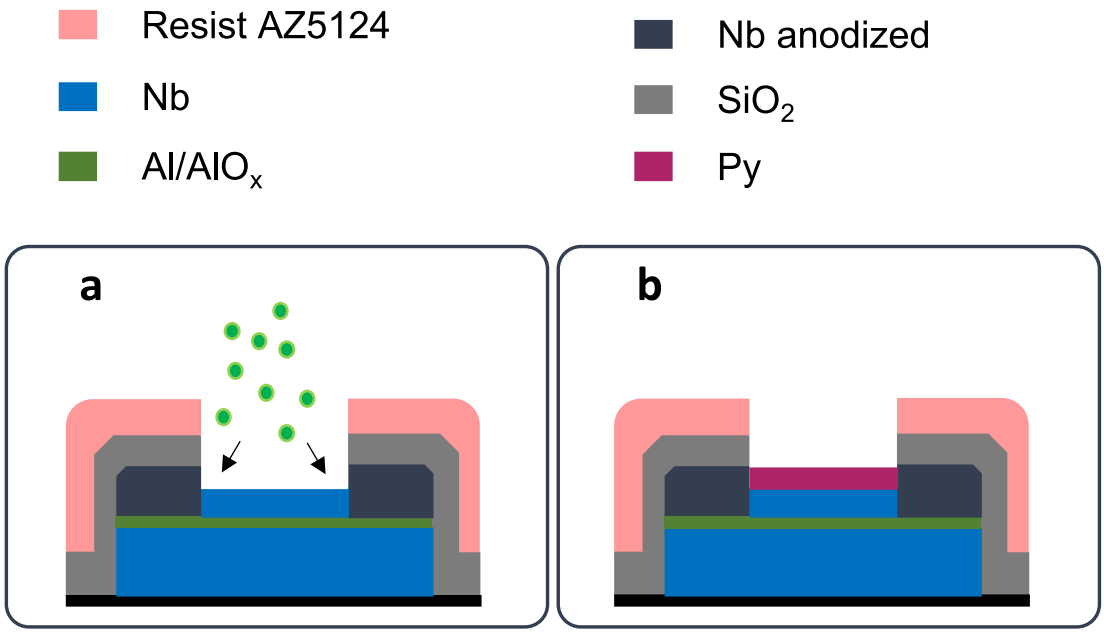

Figure 2.7. (a) Soft etching of the Nb interlayer and (b) deposition of F layer.

been analysed by using a Scanning Electron Microscope (SEM) equipped with a probe for energy dispersion spectometry (EDS) to measure their stechiometry ratio: 83.3 % Ni and 17.7% Fe, respectively.

A structural and morphological analysis of our thin films has been performed by Atomic Force Microsopy (AFM). In Fig. 2.8, we show typical AFM images (2 μm$\times$2 μm) obtained for a 40-nm-thick Nb layer before the etching cleaning (a) and after (b), and for a Nb (30 nm)/ Py (3 nm) bilayer (c). The mean-square-root roughness is $R_q \sim 0.4$ nm, for the Nb film before the etching, whereas $R_q \sim 0.5$

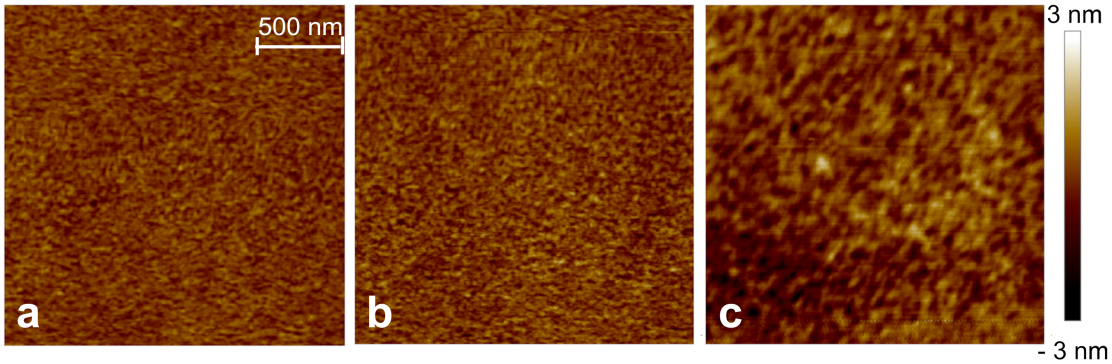

Figure 2.8. Topography maps (2 μm $\times$ 2 μm) obtained by AFM for a 40 nm-thick Nb layer (a) before the etching cleaning and (b) after, and (c) for a Nb (30 nm)/ Py (3 nm).

nm, for the Nb film after the cleaning process and for the 3-nm-thick Py grown on the etched Nb. This result suggests that the etching process does not significantly affect the S/F interface. The overall roughness of the junction S/F interface was thus determined by the roughness of the Nb interlayer in the junction. Grain sizes were so fine that they could not be resolved with our image software.

V lithography: wiring

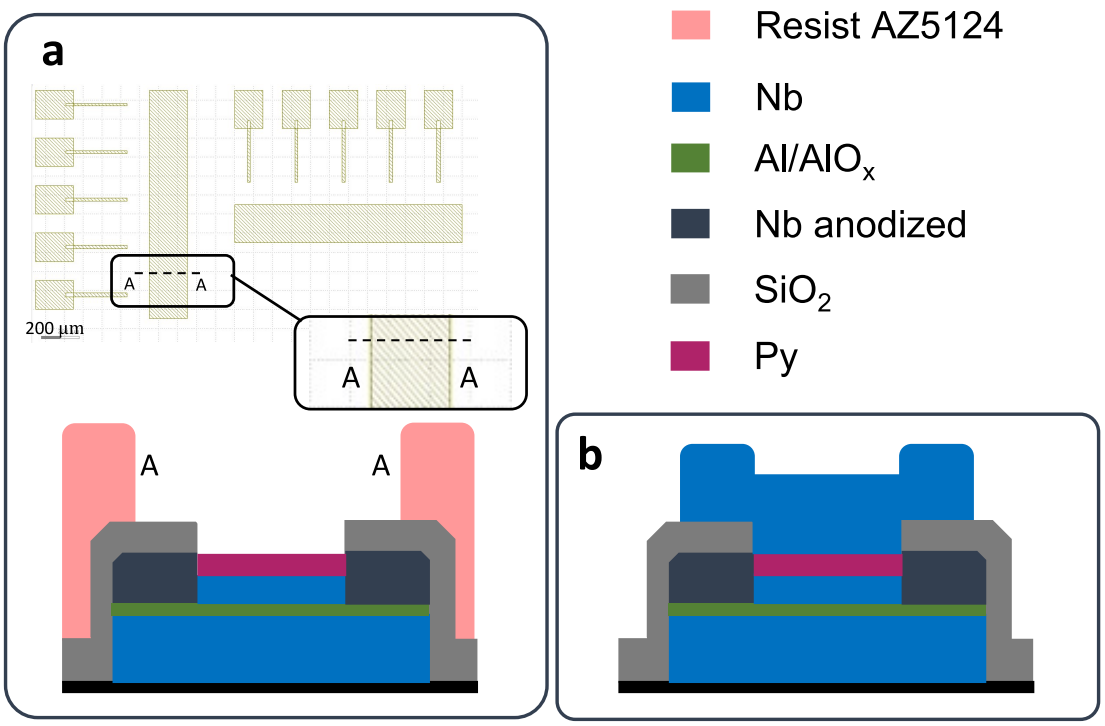

Figure 2.9. (a) Definition of the wiring for the depostion of the top Nb layer and (b) lift-off.

Finally, after a last photolithography step to define the geometry of the device wiring (Figure 2.9a), a thicker layer (350 nm) of the Al film was deposited in the same condition and at the same rate of the base and top Nb layers described above. Again, to avoid any heating problems the deposition was carried out in two steps with a wait-time of 2 hours. In the case of SIsS JJs, a cleaning step was performed before the wiring deposition to remove the surface oxide by using an ion gun working at low power. The process was completed with a lift-off procedure by placing the samples in acetone at room temperature for about 3 hours (Figure 2.9b). In Figure 2.10, we show a picture of a junction set by using

a SEM and a detail showing a circular junction having an area of about 7 μm^2 by using both a SEM and AFM.

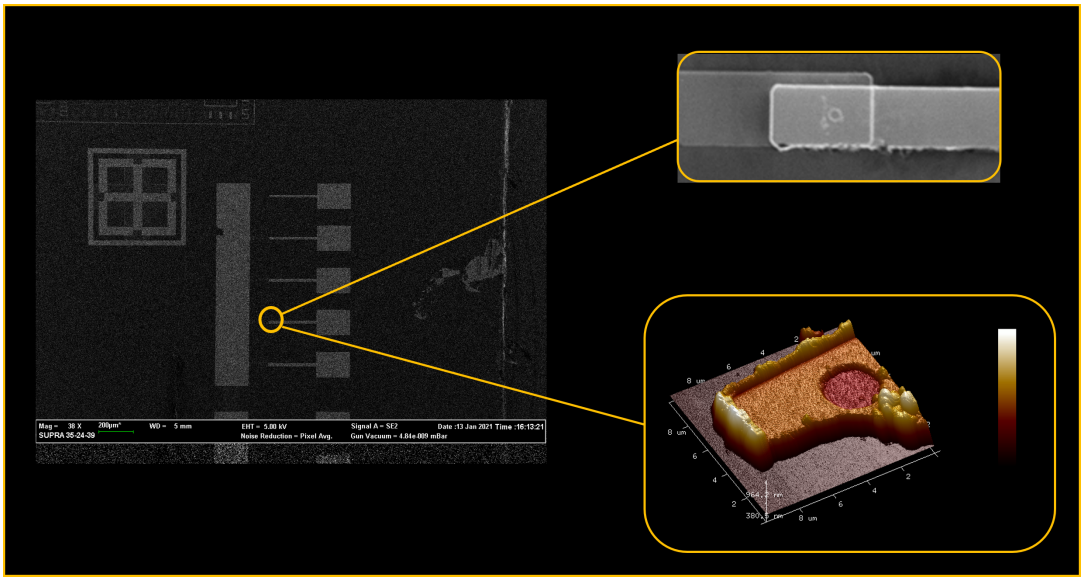

Figure 2.10. SEM image of a set of circular SIsFS having a diameter ranging from 2 to 10 μm. Upper inset: magnification of a circular junction with a diameter of 3 μm. Lower inset: an AFM image of a circular junction with a diameter of 3 μm.

2.3 I-V curves and junction characterization

The samples have been measured by thermally anchoring them to a mixing He^3/He^4 chamber of Triton cryofree dry dilution refrigerator made by Oxford Instruments, with customized low-noise filters anchored at different temperature stages (Appendix A.4). In Fig. 2.11a and 2.11b, we show the I-V curves as a function of temperature for an SIsS and SIsFS, respectively, with $d_S = 10$ nm, i.e., with $d_S \sim \xi_S$. From I-V curves measured up to the resistive branch, we have estimated normal-state resistance to be almost independent of temperature: $R_N = 76 \pm 1\ \Omega$ for the SIsS in Fig. 2.11a and $R_N = 421 \pm 5\ \Omega$ for the SIsFS in Fig. 2.11c. From the I-V curves, we obtain $I_c R_N(T)$ in Fig. 2.11c and 2.11d. In Fig. 2.11c, we observe a deviation from the standard tunnel behavior and to better point out this feature, we plot the expected Ambegaokar-Baratoff dependence of $I_c R_N(T)$ (Equation 1.36) considering that in our sample $2\Delta \sim 2.45$ meV, $T_c \sim 8.8$ K and that the critical current at low temperatures is suppressed

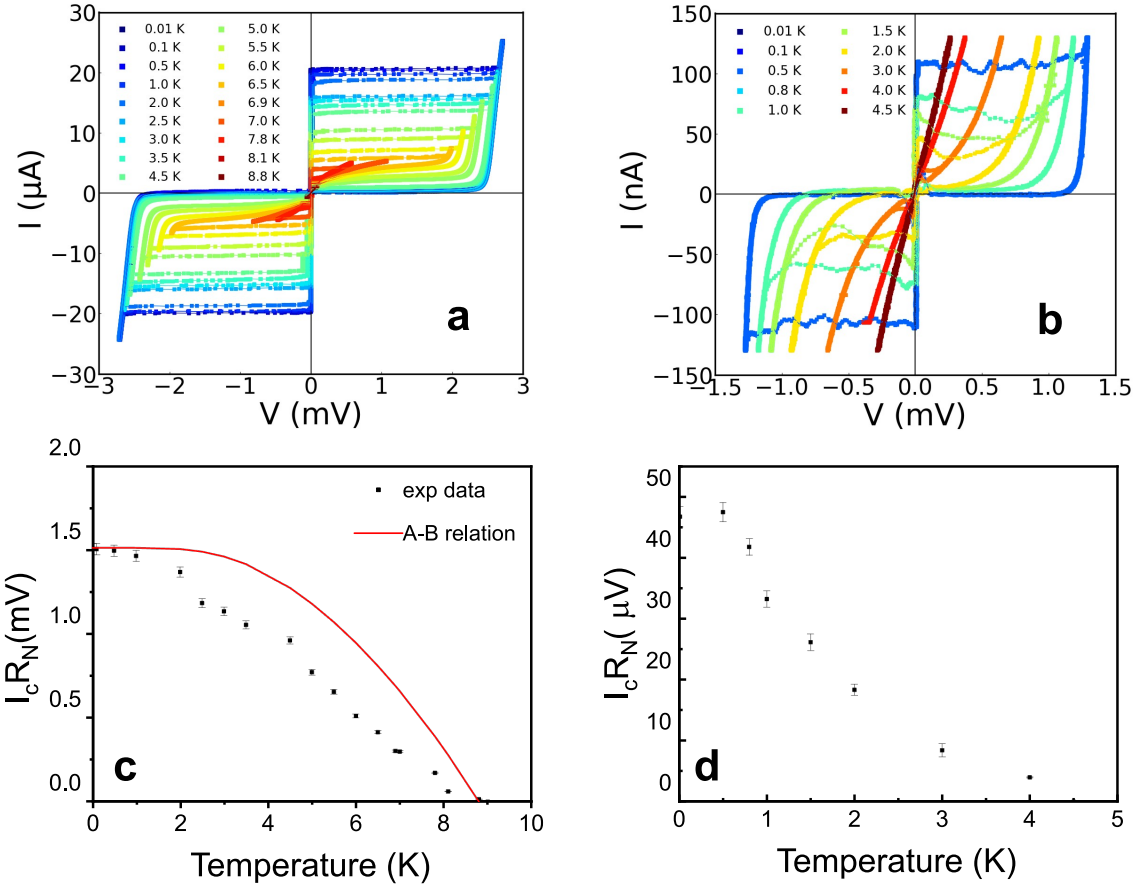

Figure 2.11. I-V curves as a function of the temperature (a) for a SIsS JJs with $D = 4$ μm and (b) for SIsFS JJs with $D = 2$ μm. The I_cR_N product as a function of the temperature (c) for a SIsS JJs with $D = 4$ μm, and (d) for SIsFS JJs with $D = 2$ μm. The thickness of the s interlayer is 10 nm for all the JJs depicted.

of 20% with respect to the ideal value (red line in Fig. 2.11c). This deviation can be reasonably ascribed to the fact that the dielectric barrier in our JJs is produced by the deposition of a thin Al layer that is subsequently oxidized. As a result, some residual metallic Al layer appears adjacent to the tunnel barrier. The critical current and its temperature dependence are strongly influenced by any normal or superconducting surface layer with properties that differ from those of the basis niobium electrode. Indeed, due to the proximity effect, the whole electron system differs from a standard BCS, which leads to considerable deviations of the $I_cR_N(T)$ dependence compared to that predicted by Ambegaokar-Baratoff [83, 84].

However, for our purpose the main point to be stressed in Fig. 2.11 is that critical current density and I_cR_N values in the SIsFS JJs with $d_S \sim \xi_S$ are two orders of

magnitude lower, as compared to the SIsS JJs (compare Fig. 2.11c with 2.11d). In such case, the superconductivity in the s spacer is suppressed due to its small thickness and the proximity with a F film. As a consequence of this weak link through the IsF barrier, we observe a suppression both of $T_c \sim 4.5$ K and Δ ($2\Delta \sim 1.4$ meV at $T = 10$ mK). Another feature of the proximity-like behavior of these SIsFS JJs is an exponential decay of $I_cR_N(T)$ observed in Fig. 2.11d. The reason that we observe values of the critical current and normal resistance even smaller than those reported in literature for SIFS JJs [75, 85, 86, 87] can be ascribed to the fact that we have introduced a strong ferromagnet as F interlayer. Nevertheless, the properties of such ferromagnetic junctions can be dramatically improved by increasing the thickness of the intermediate layer to 30 nm. In this case $d_s \sim 3\ \xi_S$, and the transport regime of the junction is extremely sensitive to temperature. Above the transition temperature of the 30-nm-thick s interlayer ($T \sim 6$ K[88]), a proximity-like tail is observed in Fig. 2.12. At low temperatures, since the s interlayer is sufficiently thicker than the superconducting coherence length ξ_S, the phase mainly drops across the tunnel barrier, while the phase shifts at the s film and in the S electrodes are negligibly small. Thus, this device can be considered as an SIs junction in series with a sFS junction: the SIs JJ with the smaller critical current sets the behavior of the overall structure [59, 58] resulting in $I_cR_N = 1.3$ mV for $D = 4$ μm and $I_cR_N = 1.2$ mV for $D = 3$ μm at $T = 10$ mK. These values are reduced by only 20% with respect to the reference SIsS JJ ($I_cR_N = 1.5$ mV). At $T = 4.2$ K, I_cR_N products decrease down to 800 μm for $D = 4$ μm and to 700 μm for $D = 3$ μm. They are comparable with those reported in Ref. [57, 62, 60] for SIsFS JJs with PdFe and are suitable for SFQ circuits [61].

Moreover, the high-quality of the junctions is evident also from the shape of subgap branch, which is clearly characterized by high values of the subgap resistance and does not show any deviations from the behavior of the reference SIsS JJs (Fig. 2.11a). Finally, according to the established empirical relation [89]: $1/C_s(\mathrm{cm}^2/\mu\mathrm{F}) = 0.2 - 0.0043 \log_{10} j_c(\mathrm{kA/cm}^2)$, a specific capacitance for AlO_x barrier C_s is of the order of ~ 80 fF/μm^2; thus, a quality factor Q of order of

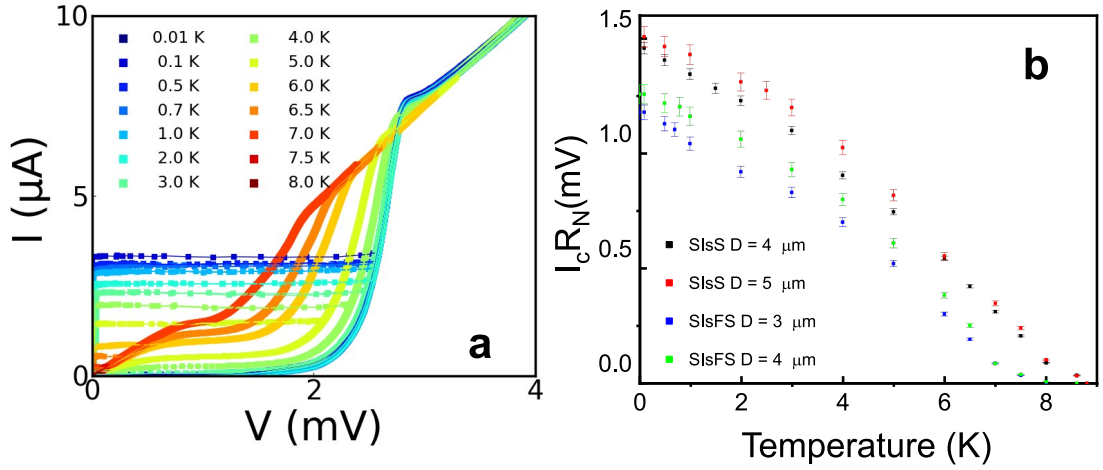

Figure 2.12. (a) I-V curves as a function of the temperature for a SIsFS with $D = 3$ μm. In our experimental setup, the current and voltage are affected by errors of 1 % and 2%, respectively. (b) I_cR_N product as function of the temperature for a SIsS with $D = 4$ μm (black dots) and with $D = 5$ μm (red dots), for a SIsFS with $D = 3$ μm (blue dots) and with $D = 4$ μm (blue dots). The thickness of the s interlayer is 30 nm for all the JJs depicted.

~ 20 for all junctions shown in Fig. 2.12.

We refer to Table 2.1 for a review of the main parameters of these junctions at $T = 10$ mK.

JJ type	d_s (nm)	D (μm)	j_c (A/cm^2)	R_NA (kΩ/μm^2)	I_cR_N (mV)
SIsS	10	4	160 ± 32	0.9 ± 0.2	1.51 ± 0.04
SIsFS	10	2	3.53 ± 0.71	1.3 ± 0.3	0.05
SIsS	30	5	66 ± 13	2.1 ± 0.4	1.50 ± 0.04
SIsFS	30	3	46 ± 9	2.5 ± 0.5	1.18 ± 0.03
SIsFS	30	4	53 ± 11	2.4 ± 0.4	1.26 ± 0.04

Table 2.1. Parameters of circular JJs based on Nb technology at $T = 10$ mK: thickness of the s interlayer d_s, diameter D, critical current density j_c, product of the normal resistance per area R_NA, and product normal resistance per critical current I_cR_N.

2.4 Magnetic dependence of the Josephson critical current

In Fig. 2.13, we report the $I_c(H)$ curves measured at $T = 0.3$ K for SIsFS with different F thickness d_F and diameter D. These measurements have been per-

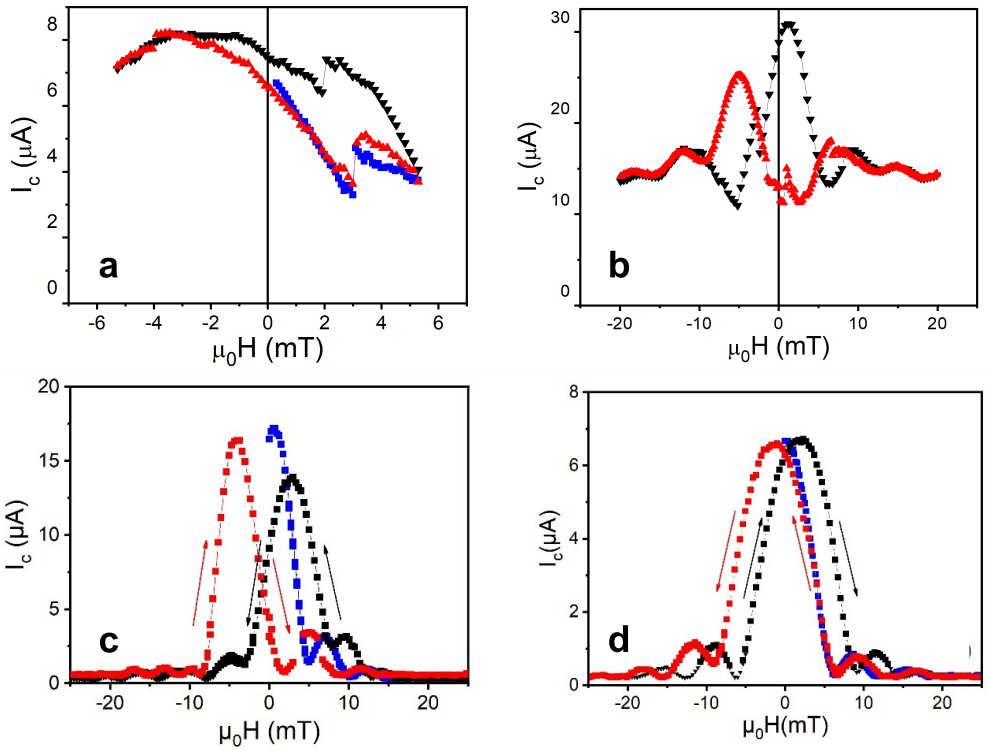

Figure 2.13. *$I_c(H)$* curves measured at $T = 0.3$ K for SIsFS with (a) $d_F = 15$ nm and $D = 5$ μm, (b) $d_F = 10$ nm and $D = 5$ μm, (c) $d_F = 3$ nm and $D = 5$ μm, and (d) $d_F = 3$ nm and $D = 3$ μm. Arrows indicate the sweeping direction of H for each curve: the blue curves are the curves obtained from the demagnetized state *(virgin curve)*, the black curves are obtained by sweeping H from positive to negative fields (down curves), whereas the red curves are obtained from negative to positive fields (up curves).

formed by using the Heliox set-up (Appendix A.3). Since $\xi_F \simeq 1$ nm, the JJs realized with very large Py thicknesses ($d_F \geq 10$ nm) are expected to behave as tunnel SIS junctions in series with an sF bilayer. However, switching between two different critical current states is still feasible since the F stray fields can penetrate sideways the s interlayer, as shown in hybrid SF architectures [67, 90]. Indeed, for these thicknesses, despite the extremely high demagnetizing factor in the perpendicular direction of the F films, the stray fields are not negligible [91, 92], as it will better addressed in the Chapter 3. The presence of F stray fields strongly affects the $I_c(H)$ curves, leading to substantial perturbations in the distribution of critical currents, and hence to significant modifications of the usual Airy pattern (Equation 1.9) [67, 90]. Moreover, when the magnetic field sweep direction is reversed, the shape of the $I_c(H)$ curve does not coincide with

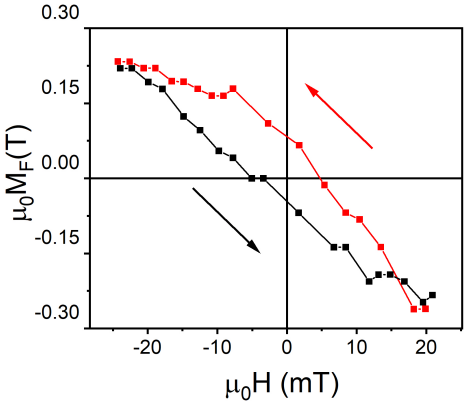

Figure 2.14. *M(H)* curve calculated from the $I_c(H)$ dependence in Fig. 2.13c as described in the the Section 1.2.3. Arrows indicate the sweeping field direction.

the initial one, as a consequence of a non-uniform reversal of the strong magnetization [93, 94].

For JJs with $d_F = 3$ nm, the SIsFS behaves as a series of a SIs and sFS JJs (Fig. 2.12b), but since $d_s < \lambda_L \sim 100$ nm , the whole structure behaves as a single junction with respect to an external field H [59, 58]. Indeed, by reducing the F thickness down to 3 nm we recovered an almost regular Airy pattern (Fig. 2.13c-d). Moreover, in Fig. 2.13d, the nodes in the $I_c(H)$ curves approach zero what indicates a uniform current distribution. Therefore, the scaling down has led to an optimization of our devices as switchable elements, since a large volume of the ferromagnet affects the quality of the JJ.

Furthermore, in our JJs with a 3-nm-thick Py, we observe an inverse hysteresis of the Josephson supercurrent [95, 96]. The central maximum of the up curves (red curves in Fig. 2.13) is shifted at negative H fields, whereas the central maximum of the down curves (black curves) is shifted at positive H fields. To better clarify the observed anomaly, in Fig. 2.14 we report the hysteresis loops of a Py barrier obtained from the $I_c(H)$ curves in Fig. 2.13, according to the Josephson magnetometry (Section 1.2.3). The obtained cycle strongly deviates from the ones reported in Fig. 2.3, where, as usual, a remanent positive magnetization is observed. In Fig. 2.14, the signs of the remanence and coercive fields are inverted indicating that the switching of the magnetization occurs at positive fields for the down sweeping branch of the loop. However, the occurrence of inverse hysteresis

loops in ferromagnetic materials requires the existence of at least two different ferromagnetic phases coupled together by exchange bias or characterized by two competing anisotropy [97, 98]. In our case, for an homogeneous ferromagnetic material, a flux with the opposite sign with respect to that induced by M_F must be considered to explain this curve. The investigation of the mutual interplay of the magnetic interactions at the S/F interface will be the main topic of the Chapter 3. From a practical point of view, the inverse hysteresis does not affect the write operation of our memory elements, since the sequence illustrated in Fig. 2.1 is simply inverted. Indeed, the functionality of the SIsFS with $d_F = 3$ nm and $D = 3$ μm as a switchable element using magnetic pulses as low as 30 mT has been demonstrated [99].

In conclusion, we have demonstrated the smallest JJs compatible in speed and power dissipation with the standard SFQ circuits. In the framework of quantum computing, cryogenic superconducting SFQ logic circuits can be located contiguously to qubit chips, thanks to a very low power dissipation and they can offer supporting functions such as read-out, control, and error-correction [100]. Given the stability of the magnetic properties of Py, there are no particular limitations in reducing the cross section of the ferromagnet, and JJs can be in principle further scaled down to submicron devices, e.g., by using an ion-beam lithography [77, 56, 101, 102]. Furthermore, this could lead to a reduction of the magnetic field required for the control of the switchable elements. Indeed, below a critical volume the transition to the superparamagnetic state occurs and one might expect that the coercive and saturation fields of the junction decrease as the junction size decreases [26, 103].

Chapter 3

Spin polarization phenomena at the S/F interface

While the penetration of superconducting correlations into a ferromagnet has been intensively studied during last decades, further theoretical and experimental efforts are needed to investigate the back-action of the ferromagnet on the superconducting subsystem resulting in the leakage of magnetic moments and fields through the S/F interface. From an application point of view, this effect must be taken into account in the design and optimization of MJJs, in which the induced field can modify their memory properties.

Motivated by this issue, in this Chapter we show a complementary investigation to establish a closer correlation between the magnetic and superconducting properties of our SIsFS JJs. To investigate the role of the F stray fields, we have first performed a magnetic characterization of Nb/Py/Nb trilayers with different F thickness by using a VSM system. By measuring the $I_c(H)$ curves as a function of the temperature down $T = 10$ mK, we have developed a straightforward method to identify the hallmarks of the *inverse proximity effect* (IPE), i.e., the transfer of a ferromagnetic order into a superconductor from the S/F interface in MJJs. Our approach overcomes the lack of experimental tools that are able to probe the magnetization at the S/F interfaces with high spatial resolution and provides a key for further advances in the implementation of these JJs as switchable elements.

3.1 State of the art

At S/F interface, there are three major mechanisms responsible for the leakage of the magnetic induction field from the F to the S layer.

- In SF heterostructures when the superconducting and ferromagnetic parts are assumed to be electrically insulated, there is no proximity effect and the interaction between each subsystem is just through magnetic stray fields [104]. The Meissner effect inside the superconductor acts to screen stray magnetic fields emerging from F. Such stray fields are in some applications considered problematic, e.g., they can significantly distort the MJJs' Fraunhofer pattern [93, 94]. However, it is also possible to engineer structures and devices in which the stray fields provide novel functionality, such as influencing the ferromagnetic domain structure or providing pinning sites for Abrikosov vortices [105, 106, 107]. As an example, it has been proposed to realize Abrikosov vortex-based random access memory (AVRAM) cell, in which a single vortex encodes a classical bit [108].

- In SF proximity-coupled systems, the *inverse proximity effect* (IPE), i.e., the transfer of the magnetic moment m from the F to the S subsystem is possible as well. This phenomenon is related to Cooper pairs localized in proximity of the S/F interface: the electrons with the spin aligned along the exchange field can easily penetrate the F layer, while the electrons with the opposite spin tend to stay in S [109, 110]. As a result, the surface of the S layer down to a depth of the order of the Cooper pair size, i.e., the superconducting coherence length ξ_S ($\sim 10 - 100$) nm, acquires a net magnetic moment m_{SC} with the opposite direction to the F magnetic moment m_F, which it can even fully compensate [110, 111] (Fig. 3.1). In the dirty limit, assuming a ferromagnet with a uniform exchange energy E_{ex}, the normalized induced magnetic moment $\gamma = \frac{m_{SC}}{m_F}$ can be derived in terms of the exchange energy E_{ex}, the superconducting gap Δ and of a parameter that considers the arbitrary transparency of the S/F interface

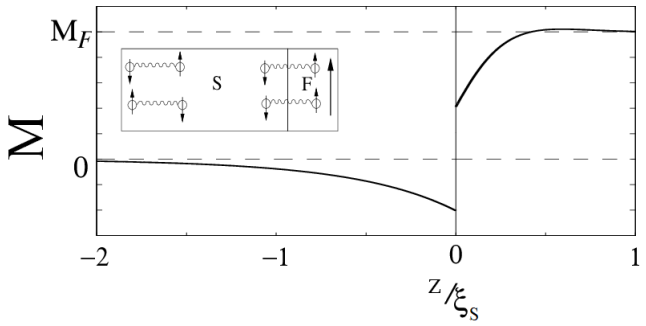

Figure 3.1. Schematic representation of the inverse proximity effect resulting in polarized Cooper pairs. Figure adapted from [109].

$\varepsilon_{b,F} = \hbar D_F/(R_b \sigma_F d_F)$:

$$\gamma(T, E_{ex}, \varepsilon_{b,F}, \Delta) = \frac{\varepsilon_{b,F}}{E_{ex}} 2\pi T \ \mathrm{Im} \sum_{\omega \geq 0} \frac{\Delta^2}{\zeta_\omega^3} \frac{\omega + iE_{ex}}{\tilde{\zeta}_\omega} \tag{3.1}$$

where ω is the Matsubara frequency, G_S and F_S are the normal and anomalous components of the Green's functions, respectively, $\zeta_\omega^3 = (\omega^2 + \Delta^2)^{3/2}$ and $\tilde{\zeta_\omega} = \sqrt{(\omega + \varepsilon_{b,F} G_S + iJ)^2 + (\varepsilon_{b,F} F_S)^2}$ [112].

- More recently, it has been proposed that the direct S/F interface proximity effect is always responsible for the generation of screening supercurrents in response to the F vector potential at the S/F interface, the so-called *electromagnetic proximity effect* [113]. These Meissner supercurrents generate a magnetic induction field B_{SC} in the S film that decays at distance z from the F/S interface of the order of the London penetration depth λ_L:

$$B_x = -4\pi M_F Q e^{z/\lambda_L}, \tag{3.2}$$

where the parameter Q can be derived in the framework of microscopic theories and oscillates with the thickness of the ferromagnetic layer. This feature is related to the spatial oscillations of the singlet and triplet components of superconducting correlations in the ferromagnet. As a result, the direction of the total current in the ferromagnet is determined by the ratio d_F/ξ_F. Accordingly, the magnetic field induced in the superconductor can be directed both anti-parallel and parallel to M_F (Fig. 3.2). Moreover,

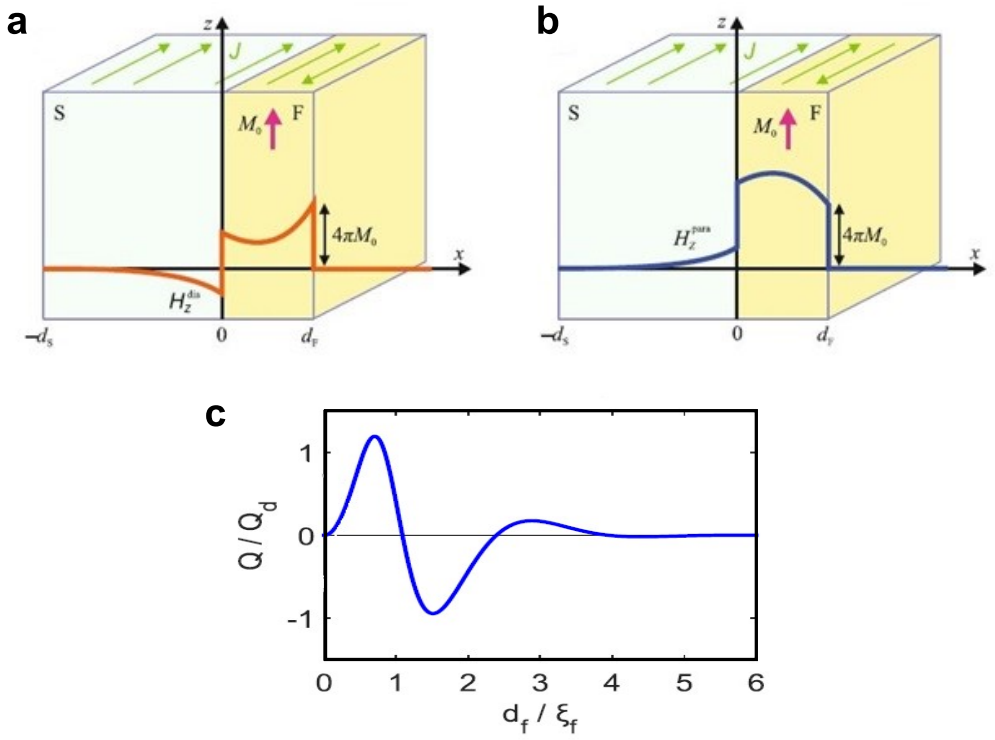

Figure 3.2. Schematic picture of the magnetic field spontaneously arising in a S/F bilayer owing to the electromagnetic proximity effect when the magnetic induction field in the superconductor $B_z = -4\pi M_F Q e^{z/\lambda_L}$ is (a) diamagnetic ($Q > 1$) and (b) paramagnetic ($Q < 1$). (c) Dependence of Q/Q_d on the F thickness derived from microscopic theories in the dirty limit, with $Q_d = \pi^2 \sigma_F \xi_F^2 \tanh(\Delta/2T)/(2\hbar c^2)$. Figure adapted from [113, 114].

> Q is significantly enhanced if the ferromagnet consists of two layers with non-collinear magnetization [114, 115].

In general, the experimental difficulty of studying such phenomena lies in the need for a magnetic probe that is sensitive to fields that decay over distance of 10 - 100 nm. Indeed, there are very few techniques able to reconstruct the profile of the magnetic field across the S/F interface, e.g., the low-energy muon-spin spectroscopy [116] and polarized neutron reflectometry [117]. Indirect evidences of the generation of the induced magnetization M_{SC} have emerged from the measurements of S/F interface thin films across T_c [118, 119]. In the latter case, in order to obtain a measurable signal caused by the spin-polarization, the S layer thickness must be comparable to ξ_S. Nevertheless, discriminating between the spin screening due to the IPE and the Meissner screening in response to the vector potential at S/F interface has been controversial [120] and a direct comparison

with the theoretical model is still missing.

In this context, an unambiguous experiment with the design of appropriate Josephson junction layout enabling to distinguish these two effects is still regarded as a major contribution [115, 121]. In Ref. [115], it has been proposed that the electromagnetic proximity effect can be probed experimentally by measuring the critical current $I_c(H)$ dependence of a SIsFF' JJ, with an s electrode with a thickness of the order of λ_L. From the shift of the Fraunhofer pattern, one can determine experimentally the modulus and the direction of Q (Equation 3.2), both in the case of collinear or non-collinear magnetization of a composite layer FF'.

In Ref. [121], the effect of the induced magnetization due to IPE on the Fraunhofer pattern has been investigated in detail in standard SFS JJs. In this case, the dimensionless induced magnetic moment γ depends on the phase difference ψ across the junction. From Equations 8-10 in Ref. [121], we can write [122]:

$$\gamma(T, E_{ex}, \varepsilon_{b,F}, \Delta) = \frac{\varepsilon_{b,F}}{E_{ex}} 2\pi T \sum_{\omega \geq 0} \frac{\Delta^2 \cos^2(\psi/2)}{\zeta_\omega^3} \mathrm{Im}\left(\frac{\omega + iE_{ex}}{\tilde{\zeta_\omega}}\right). \tag{3.3}$$

Considering this contribution to the magnetic flux through the JJ, the total flux becomes [121]:

$$\Phi = \mu_0 H L(2\lambda_L + d_F) + \mu_0 M_F L d_F (1 - \gamma), \tag{3.4}$$

Hence, in the case of full screening $\gamma = 1$ and the displacement due to the S magnetization cancels out with that due to the F magnetization, thus resulting in zero-centered $I_c(H)$ curves [121]. Moreover, a significant broadening is also expected. In a standard Fraunhofer pattern, the minima occur at the multiple of the flux quanta Φ_0 (Section 1.1.2). In the limit of a strong polarization of the Cooper pairs at the S/F interface, the half width of the central peak of $I_c(H)$ curves should correspond to a flux: $\tilde{\Phi} = \frac{\mu_0 H L d_m + \mu_0 M_F L d_F}{\Phi_0} = p = \frac{2\gamma \mu_0 M_F L d_F}{\Phi_0}$. So the broadening is expected for larger p, i.e., it is determined by the strength of the induced spin polarization [121].

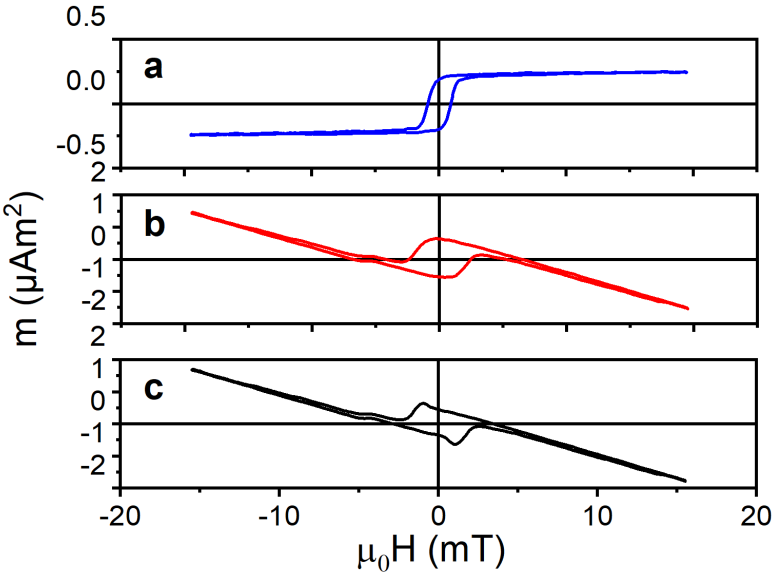

Figure 3.3. Magnetic moment as a function of the applied field *m(H)* at $T = 4$ K (a) and $T = 20$ K (b) of Nb (30 nm)/ Py (3 nm)/ Nb (400 nm) trilayers. (c) Nb hysteresis loops, isolated by taking the difference between the *m(H)* curves of Nb (30 nm)/ Py (3 nm)/ Nb (400 nm) trilayers above and below T_c [96].

3.2 Experimental: the role of the F stray fields

To investigate the mutual magnetic interaction between the F layer and the two adjacent S layers through their respective stray fields, we have performed a magnetic characterization of Nb/Py/Nb trilayers by using a VSM equipped with a He-flow cryostat of Oxford Instruments-MagLab (Appendix A.2). The Nb (30 nm)/ Py (d_F)/ Nb (400 nm) trilayers have been deposited on oxidized Si wafers with lateral dimensions of 10 mm x 10 mm using DC magnetron sputtering in an ultrahigh vacuum chamber. The thickness of the Nb layer is chosen to allow a comparison with the properties of our MJJs with a 30-nm-thick Nb interlayer (Section 2.3), while the Py thickness ranges from 3 to 10 nm.

The magnetometer detects the superposed signal from the F and S films. To distinguish the behavior of every component of the heterostructures, the magnetic measurements have been performed across T_c. It is easy to figure out why by looking at curves *m(H)* in Fig. 3.3. Above T_c, the paramagnetic signal of the Nb in the normal state and of the Si substrate is negligible. Indeed, at

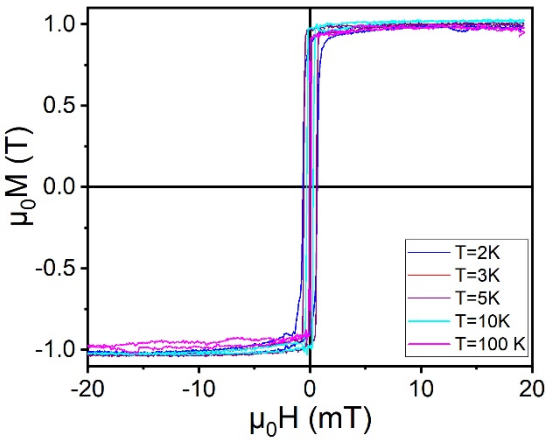

Figure 3.4. Hysteresis cycles of a 14-nm–thick Py layer on a Si/SiO_x wafer taken at different temperatures below 100K.

$T = 20\ K > T_c$, we observe the hysteresis loop of the bare Py layer (Fig. 3.3a). Below the critical temperature T_c, the diamagnetic signal of the Nb contributes to the overall signal of the sample (Fig. 3.3b). Since the Curie temperature of the bulk Py ($T_{\text{Curie}} \cong 872K$) far exceeds the temperature range in Fig. 3.3 [123], we can expect small changes of M_F (Fig. 1.6). However, the Curie temperature can be frustrated in ultrathin ferromagnetic films [124], thus we have verified that the Curie temperature of our Py films is above 100 K. In Fig. 3.4, we report several hysteresis cycles of a layer of Py (14 nm) on Si/SiO_x taken at different temperatures below $T = 100$ K. We cannot observe any substantial difference between the value of the saturation magnetization at this temperature and at low temperatures. Therefore, we can conclude that the magnetization of the F layer is constant in the temperature range across T_c. By assuming a linear contribution to the whole signal by each component of the heterostructure, we can obtain the Nb hysteresis loop by subtracting to the cycle at $T = 4\ K > T_c$ the cycle at T = 20 K [125]. As shown in Fig. 3.3c, the diamagnetic signal of the S layer is the one expected for the Nb layers in the Meissner state. In this case, we are not able to distinguish the induction field in S at the S/F interface, which is masked by the response of the bulk Nb.

To isolate the response of the S/F interface, we have performed thermoremanence measurements across T_c (Fig. 3.5b-d). Since the magnetic moment

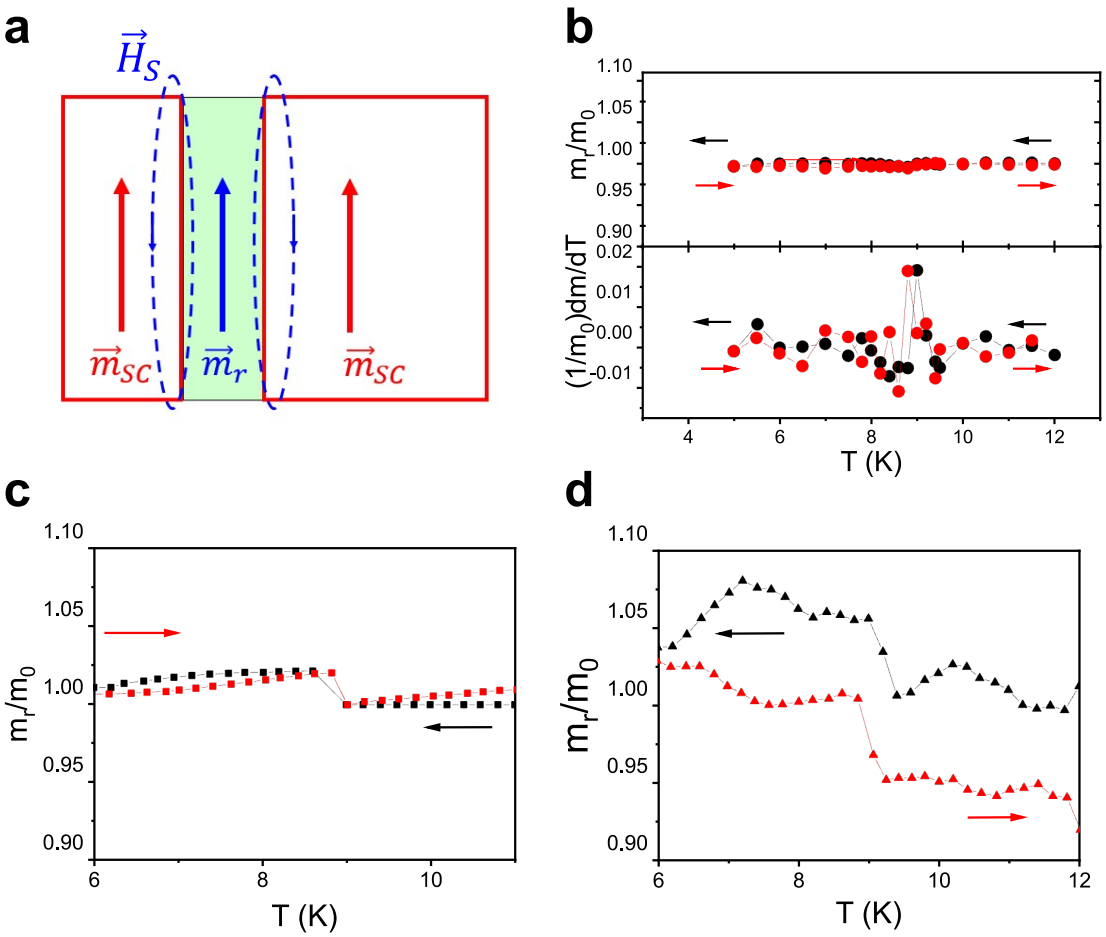

Figure 3.5. (a) Sketch of the F layer stray fields lines H_S with respect to the remanent magnetic moment of the F layer m_r. Panels (b), (c) and (d) report the temperature dependence of the normalized remanent magnetic moment m_r/m_0: (b) $d_F = 3$ nm, (c) $d_F = 7$ nm, and (d) $d_F = 10$ nm [95].

is recorded at zero field, its changes below T_c can be mainly attributed to the Meissner expulsion of the F stray fields. Despite the high demagnetizing factor in the perpendicular direction of the film, the F stray fields can still penetrate the adjacent S layers, inducing a paramagnetic Meissner effect (3.5a). This effect leads to an increase of the measured magnetic moment of a few percent below T_c provided by a sufficient thickness of the F layer [91, 126, 127].
To perform these measurements, at $T = 12$ K we have brought to saturation the trilayers. Then, H has been switched-off and m_r of the trilayers has been scanned from 12 to 6 K (black curves) and then back to 12 K (red curves). Fig. 3.5b-d shows the temperature dependence of the magnetic moment m_r normalized to the initial value at $T = 12$ K m_0. We can point out the following features.

- In the sample with $d_F = 3$ nm, m_r remains almost unchanged across T_c, and only $1/m_0 dm/dT$ allows the determination of the T_c, suggesting the negligible effect of the F layer stray field (Fig. 3.5b).

- The samples with $d_F = 7$ nm (Fig. 3.5c) and the one with $d_F = 10$ nm (Fig. 3.5d) show a clear step in the T dependence of the magnetic moment at ~ 8.8 K, which is taken as T_c value, in good agreement with the previous reports on Nb/Py multilayers [92, 128]. Moreover, in Fig. 3.5d the magnetic moment measured with increasing temperature is lower than the initial one: the flux expulsion of the S layers to F stray fields may presumably lead in turn to an out-of-plane component in F at the S/F interface [92, 128].

The result of the latter measurements is consistent with the scenario suggested in the Section 2.4: for large Py thickness, even if the JJ behaves as a tunnel structure consisting of an SIs JJ and a FS bilayer, the F stray fields can penetrate sideways the s interlayer, thus, leading to a two-magnetic state behavior of the critical current (Fig. 2.13 b-c).

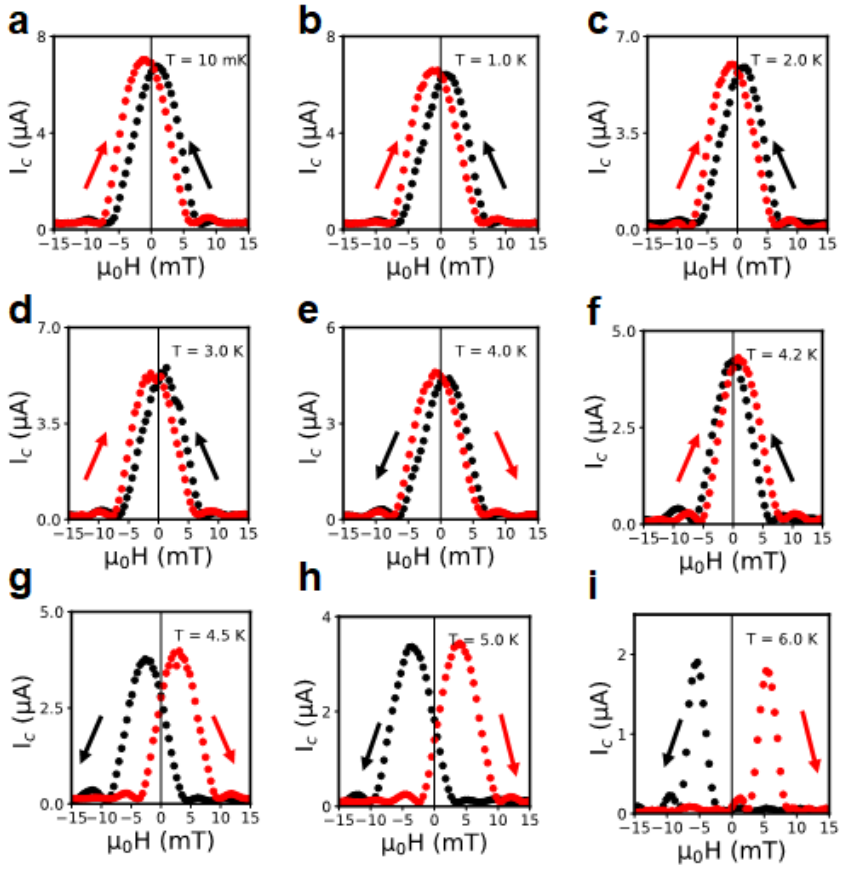

Figure 3.6. Temperature dependence of the magnetic hysteresis for the SIsFS Josephson Junction with $R = 2$ μm. We have measured the $I_c(H)$ curves by sweeping the field in the range (-15, 15) mT at different temperatures T: (a) $T = 1$ K, (b) $T = 2$ K, (c) $T = 3$ K, (d) $T = 4$ K, (e) $T = 4.2$ K (f) $T = 4.5$ K, (g) $T = 5$ K, and (h) $T = 6$ K. The black and red curves are the magnetic pattern in the downward and upward direction of the magnetic field, respectively [129].

3.3 Experimental: the role of the inverse proximity effect

We have experimentally accessed the IPE by exploiting the Josephson effect as a highly sensitive probe to magnetic fields at the nanoscale. In Fig. 3.6, we show the magnetic field patterns for a SIsFS JJ with R= 2 μm measured as a function of the temperature. Below $T = 4$ K, we observe an inverse hysteresis of the $I_c(H)$ curves, i.e., a shift of the $I_c(H)$ curves in the opposite direction to the one due to M_F [95, 96]. Above $T = 4$ K the ordinary behavior is restored, i.e., we observe the maximum of the down curves at a negative field and the maximum of the up curves at a positive field. These measurements allowed us to definitely rule

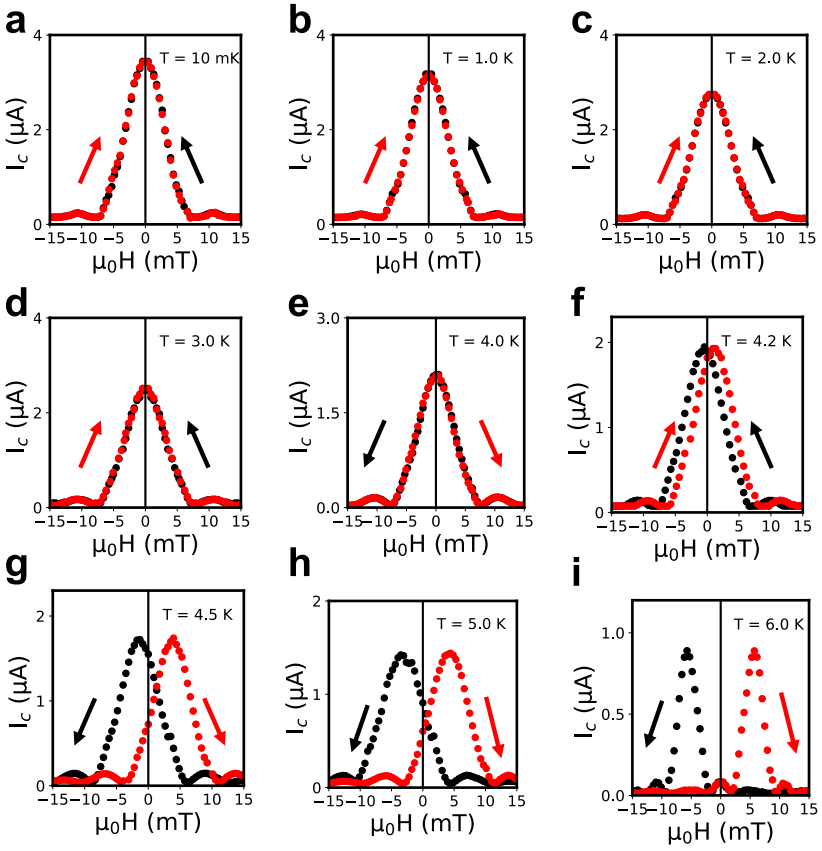

Figure 3.7. Temperature dependence of the magnetic hysteresis for the SIsFS Josephson Junction with $R = 1.5$ μm. we have measured the $I_c(H)$ curves by sweeping the field in the range (-15, 15) mT at different temperatures T: (a) $T = 10$ mK, (b) $T = 1$ K, (c) $T = 2$ K, (d) $T = 3$ K, (e) $T = 4$ K, (f) $T = 4.2$ K (g) $T = 4.5$ K, (h) $T = 5$ K, and (i) $T = 6$ K [129].

out that the main origin of the inverse magnetic hysteresis of the $I_c(H)$ curves is related to the F stray fields (Section 2.4). Since the magnetization of the F layer can be considered constant in temperature (Fig. 3.4), it is unlikely that changes of the hysteresis of the $I_c(H)$ curves can be ascribed to changes of the hysteresis loop of the F layer [95, 96]. Conversely, we expect a significant dependence of the IPE in this temperature range, as predicted in the Ref. [109] and experimentally observed [118].

In Fig. 3.7, we show the magnetic field patterns for a SIsFS JJ with $R = 1.5$ μm. Zero-centered $I_c(H)$ curves can be easily observed below T= 4 K, while above T = 4 K the ordinary hysteresis of the $I_c(H)$ curves is recovered. As mentioned in the Section 3.1, in the case of full screening $\gamma = 1$: the displacement due to the S magnetization cancels out with that due to the F magnetization, thus, resulting

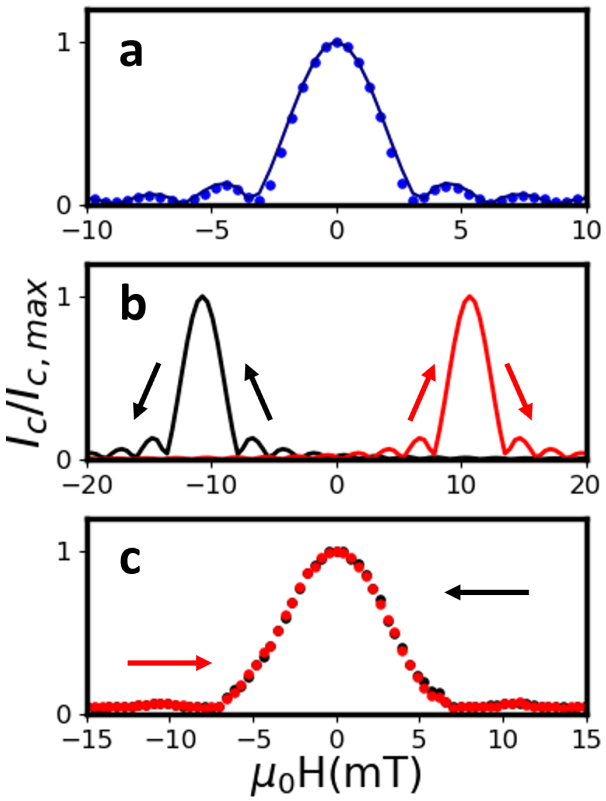

Figure 3.8. (a) Plot of normalized I_c as a function of the magnetic field H for a circular SIsS JJ with radius $R = 1.5$ μm. Data represented by solid symbols have been fitted with the theoretical Airy pattern (Equation 1.9, shown as solid lines). The error bars on the critical current are around 3% (Ref. [99]). (b) Simulated $I_c(H)$ curves in a SIsFS JJ, in case of non-spin polarization, obtained by using the same parameters of the junction reported in panel (a) and F magnetization $\mu_0 M_F = 1$ T. (c) Measured magnetic field pattern of a circular SIsFS JJ with radius $R = 1.5$ μm in the range (-15, 15) mT [129].

in a lack of the hysteresis [121].

Moreover, we also observe a broadening of the central maximum of the $I_c(H)$ curves. To better highlight this feature, in Fig. 3.8a the magnetic field pattern of non-magnetic SIsS JJ with $R = 1.5$ μm is reported. To facilitate the comparison with the SIsFS junctions, the curves have been normalized with respect to their maximum value $I_{c,max}$. The magnetic pattern has been fitted by considering the Airy pattern as the functional form of the $I_c(H)$ curve (Equation 1.9). The fitted values R = 1.52 $\pm$ 0.02 μm and λ_L = 120 $\pm$ 20 nm agree with nominal junction dimensions and the expected magnetic penetration depth for Nb [93, 56]. The

nodes in the Airy pattern approach $I_c = 0$ indicating that the current density is homogeneously distributed throughout the junction, there are no shorts in the surrounding oxide, and no flux is trapped within the junction electrodes [130].
The simulated curves in Fig. 3.8b have been obtained by considering Equation 1.40 and the Py saturation magnetization equal to $\mu_0 M_s = 1$ T (Section 2.2.1) and junction dimensions as those of the JJ reported in Fig. 3.8a.
In Fig. 3.8c we show the experimental pattern for the ferromagnetic SIsFS JJ containing a 3-nm-thick Py interlayer and $R = 1.5$ μm. One can easily observe a widening of the central peak of about a factor 2.5. For circular junctions with the current flowing out-of-plane and the field applied in-plane, I_c follows an Airy pattern in flux with its first minimum at $\Phi = 1.22\ \Phi_0$ [131]. Hence for MJJs, the first minimum should occur at $\mu_0 H_{min} = \frac{1.22\Phi_0 - \mu_0 M_F d_F}{d_m} = \frac{1.22\Phi_0}{d_m} + \mu_0 H_{shift}$. The half-width of the central peak $\mu_0 \Delta H = \mu_0 (H_{min} - H_{shift})$ should not depend on additional flux, but only on geometrical parameters of the JJs: the half-width of *$I_c(H)$* curves simulated in Fig. 3.8b is nearly the same of non-magnetic SIsS JJ in Fig. 3.8a. Moreover the effect of the magnetic hysteresis and domain structure of the F layer usually reveals itself in a narrowing of the central peak: because of the separation of the interlayer into domains in the magnetic field range close to the coercive field, the experimental curves can degenerate into a set of very narrow peaks [55, 93]. Conversely, in apparent contradiction with the existing literature, we observe that the central peak in the SIsFS JJs is two times as wide as the corresponding non-magnetic SIsS JJs. Both the broadening of the magnetic field pattern and the zero-shift of the *$I_c(H)$* curves are strong signatures of the inverse proximity effect [121].

3.4 Discussion

In Ref. [121], the effect of the spin polarization of the Cooper pairs in S on the Fraunhofer pattern is evaluated in SFS JJs. The problem must be reformulated considering that our JJs are a series connection of a SIs and sFS JJs, as shown in the Section 2.3 (Fig. 2.12). For this reason, we need to find the relation between an applied magnetic field **H** and the in-plane gradient of the phase difference

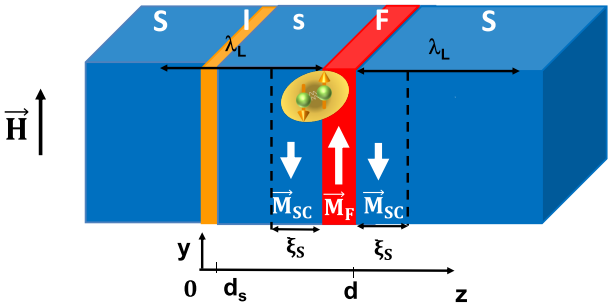

Figure 3.9. Schematic representation of the SIsFS JJs and reference system axis.

across the SIs Junction $\nabla\varphi$ and the in-plane gradient of the phase difference across the sFS JJ $\nabla\psi$ [122]. Considering the reference system in Fig. 3.9, we set an in-plane magnetic field $\mathbf{H} = \Big(0, H, 0\Big)$ and an in-plane F magnetization $\mathbf{M_F} = \Big(0, M_F, 0\Big)$. We assume that the x dependence of all the quantities of interest is weak on the length scale of λ_L. Spatial distributions of the magnetic induction $\mathbf{B}$ and of the magnetic field $\mathbf{H}$ obey the Maxwell equations in both the F and S films:

$$\nabla \times \mathbf{B} = \mu_0 \left(\mathbf{j} \; + \; \nabla \times \mathbf{M}\right) \tag{3.5}$$

$$\nabla \times \mathbf{H} = \mathbf{j}, \tag{3.6}$$

where the density of the Meissner current $\mathbf{j}$ is connected to the vector potential $\mathbf{A}$ and to the phase χ of the order parameter via the standard gauge invariant expression:

$$\mathbf{j} = \frac{1}{\mu_0}\frac{1}{\lambda_L^2}\left(\frac{\Phi_0}{2\pi}\nabla\chi - \mathbf{A}\right). \tag{3.7}$$

We obtain the following equation for $\mathbf{H}$ in the S region:

$$\partial_{zz}^2 H - \frac{1}{\lambda_L^2} H = \frac{1}{\lambda_L^2} M_{sc,SC}(z), \tag{3.8}$$

where $M_{sc,SC}$ are the induced magnetization in the s and S superconductors. The solution of the Equation 3.8 in each region is:

$$H(z) = \begin{cases} H_0 \exp(\kappa_L z) & z < 0 \\ H_0 \cosh(\kappa_L z) + S \sinh(\kappa_L z) + \tilde{M}_s(z) & 0 < z < d_s \\ H_F & d_s < z < d \\ H_d \exp(-\kappa_L (z-d)) + \tilde{M}_S(z) & d < z, \end{cases} \tag{3.9}$$

where H_0 is the magnetic field in the insulator layer, S is an integration constant and $\kappa_L = \frac{1}{\lambda_L}$. The continuity of $\mathbf{H}$ at the interfaces yields:

$$H_F = H_0 \cosh(\theta_s) + S \sinh(\theta_s) + \tilde{M}_{sc}(d_s) \tag{3.10}$$

$$H_d = H_0 \cosh(\theta_s) + S \sinh(\theta_s). \tag{3.11}$$

In order to find H_0 and S, one can write the matching conditions:

$$[\partial_z H]\,|_{z=0} = \frac{1}{\mu_0}\frac{1}{\lambda_L^2}\left([A]_0 - \frac{\Phi_0}{2\pi}\partial_x \varphi\right), \tag{3.12}$$

$$[\partial_z H]\,|_{z=d} = \frac{1}{\mu_0}\frac{1}{\lambda_L^2}\left([A]_d - \frac{\Phi_0}{2\pi}\partial_x \psi\right). \tag{3.13}$$

Here $[A]$ is a variation of the vector potential $\mathbf{A}$ at the insulating layer $[A]_0 = H_0 d_I$ and at sFS junction $[A]_d = (H_F + M_F)\, d_F$.

By considering Equations 3.12 -3.13 and that the field $\mathbf{H}$ is continuous at the interfaces $z = d_s$ and $z = d$, we arrive at the following equation for φ and ψ:

$$\mu_0 H\ 2\lambda_L + \mathcal{M}_{eff} = \frac{\Phi_0}{2\pi}\left(\partial_x \varphi + \partial_x \psi e^{-\theta_s}\right), \tag{3.14}$$

where $\theta_s = \frac{d_s}{\lambda_L}$ and $\mathcal{M}_{eff}$ is the effective magnetic moment:

$$\mathcal{M}_{eff} = \mu_0 M_F d_F\,(1-\gamma)\, e^{-\theta_s}. \tag{3.15}$$

Again, γ is the ratio of the overall magnetic moment induced in the superconductors over the magnetic moment of the F layer and can be derived by Equation 3.3.

We can immediately observe that due to the geometry of our system, both the F film magnetization and S film induced magnetic moment are reduced by a factor $e^{-\theta_s}$ (~ 0.7 in our JJs). Moreover, in our JJs Equation 3.14 can be simplified by considering that the phase difference φ the phase difference ψ are coupled via the relation:

$$I_c^{SIs} \sin\varphi = I_c^{sFS} \sin\psi, \tag{3.16}$$

where I_c^{SIs} and I_c^{sFS} are the critical current in the SIs JJ and sFS JJ, respectively. Since I_c^{SIs} is much smaller than I_c^{sFS}, as evidenced by the fact that the I-V curve in Fig. 2.12 corresponds to the curve on the insulating side SIs, the phase drop ψ across the sFS side of the JJ is negligible $\left(\psi \approx I_c^{SIs}/I_c^{sFS} \sin\varphi \ll 1\right)$. Hence, the Equation 3.14 can be simplified as [122]:

$$\partial_x \varphi = \frac{2\pi}{\Phi_0} \left(2\mu_0 H \lambda_L + \mathcal{M}_{eff}\right). \tag{3.17}$$

In Ref. [121], the deviation of the $I_c(H)$ curves from the standard Fraunhofer pattern has been evaluated for the SFS junction in which M_{SC} is a function of the phase difference ψ on this junction. The Equation 3.17 points out that we observe the Airy pattern on the SIs side of our SIsFS JJs and that the phase difference φ is not coupled directly to $\mathcal{M}_{eff}$, which is rather a function of ψ. Therefore, calculations on the shape of the magnetic field pattern reported in Ref. [121] cannot be applied to our system, while the evident broadening of the central peak at low temperatures can be qualitatively discussed in terms of the IPE. Indeed, at $T = 6$ K, when the effects of the spin polarization are expected to be negligible, the width of the central peak is halved, while a reduction of only 20% compared to the temperature $T = 10$ mK is expected if we consider only the GL temperature dependence of the London penetration depth λ_L, while it returns to be consistent with the measurement of the reference SIs in Fig. 3.8a. The shift of the maximum of $I_c^{SIs}(\varphi)$ from zero is given by $\mathcal{M}_{eff}$, which depends on the temperature dependent magnetization $M_{SC}(\psi)$. Hence, in analogy with the notation used in Ref. [121], we can still claim that the total flux through the

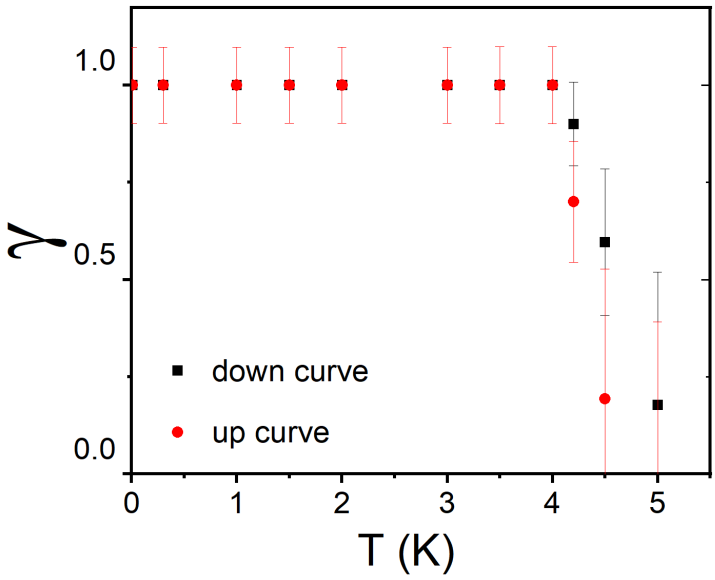

Figure 3.10. Experimental temperature dependence of the dimensionless magnetic moment γ for the set of measurements in Fig. 3.7. γ, introduced in Equation 3.15, is the magnetic moment of the S layers normalized to the F layer expressed in absolute value [129].

junction Φ is:

$$\Phi = 2\mu_0 H 2R\lambda_L + \mu_0 M_F 2Rd_F \left[1-\gamma\right] e^{-\theta_s}, \tag{3.18}$$

where, as discussed above, the exponential factor $e^{-\theta_s}$ has been introduced to take into account the effective geometry of our system. For the measurements reported in Fig. 3.7, by considering that in correspondence of $\mu_0 H_{shift}$ the total flux Φ through the junction is equal to zero we can derive the temperature dependence of γ (Fig. 3.10). As mentioned above, we can assume that at $T = 6$ K the induced magnetization has reached zero and we can derive the value of M_F for this sweeping range field. We have obtained that $M_F \sim 0.5$ T for this set of measurements. With this value of the F magnetization we have estimated $\gamma\,(T)$ dependence shown in Fig. 3.10 (black dots for the down curves and red dots for the up curves). The error bars in Fig. 3.10 have been evaluated by considering an error of 20% on the magnetic thickness d_m and on the F magnetization M_F, and as error on $\mu_0 H_{shift}$ the spacing between the points of the $I_c(H)$ curves.

The temperature dependence reported in Fig. 3.10 can be discussed in the frame

of the IPE theory [109, 110, 112]. Following the Equation 3.3, γ has been eval-

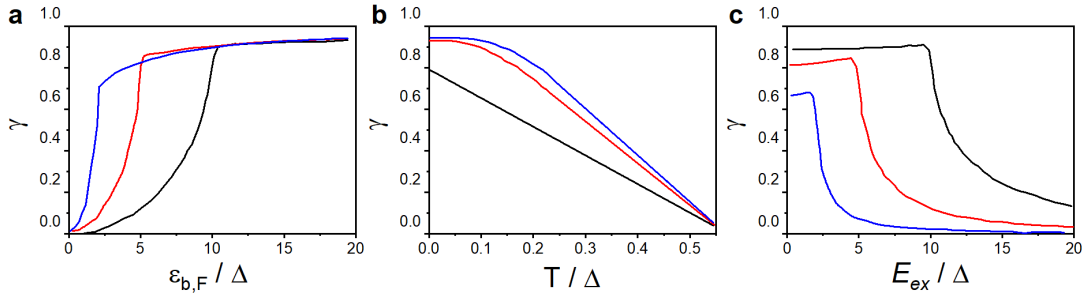

Figure 3.11. Theoretical dependence of γ (a) at $T/\Delta = 0.01$ on $\varepsilon_{b,F}/\Delta$ for $E_{ex}/\Delta =$ 10, 5, 2 (black, red, blue curve, respectively); (b) on the reduced temperature T/Δ for $J/\Delta = 10$, and for different value of $\varepsilon_{b,F}/\Delta(0) = 10,\ 5,\ 2$ (black, red, blue curve, respectively); (c) at $T/\Delta = 0.01$ on the ratio E_{ex}/Δ for $J/\Delta = 10, 5, 2$ (black, red, blue, respectively). The curves have been obtained from Equation 3.3 [122].

uated at the normalized temperature $T/\Delta = 0.01$ as function of $\varepsilon_{b,F}/\Delta$ for $E_{ex}/\Delta = 10,\ 5,\ 2$ (black, red, blue curve, respectively) (Fig. 3.11a [129]). For Nb/Py proximity-coupled system, for which $E_{ex}/\Delta \sim 10$ [49], our value of the γ at low temperatures is in agreement with the theory if we assume a value of $\varepsilon_{b,F}/\Delta$ at least equal to 10 (black curve in Fig. 3.11a). Since we observe a saturation of γ down to $T/\Delta \sim 0.5$, $\varepsilon_{b,F}/\Delta$ is expected to be even larger (Fig. 3.11b). For our values of conductivity σ_F and F diffusion coefficient D_F (Section 2.2.2), $\varepsilon_{b,F}/\Delta$ of order of 10 corresponds to a value of R_b of the same order of magnitude (fΩm^2) of MJJs with Nb/Py interface [132]. In conclusions, these calculations confirm that the main origin of the temperature dependence of the $I_c(H)$ curves can be ascribed to the spin polarization of the Cooper pairs at the S/F interface [129].

Moreover, the numerical calculations shown above, not only provide a fine theoretical framework for the experiments described in this work, but they also give an insight in how to get into the experimental conditions to observe the IPE. First, a very low temperature is required to provide ineluctable proof of the complete screening of the F layer (Fig. 3.11b). To date, the $I_c(H)$ measurements have been performed at the liquid-helium temperature to demonstrate the functionality of magnetic JJs as switchable elements for digital electronics [61] and for spintronic devices [51]. At that temperature, the induced magnetization is significantly re-

duced and the effects of the spin polarization become hard to distinguish (Fig. 3.11b). In regards to the choice of materials, weak ferromagnets, e.g., PdFe [55, 57], PdNi [46, 93], and CuNi [43, 45, 48, 85], allow to realize SFS JJs with F thickness of order of tens of nanometers because of their low values of the exchange energy. However, the large value of F thickness reduces $\varepsilon_{b,F}$, and hence γ even at low temperatures (Fig. 3.11c). On the other hand, strong ferromagnets have been mostly employed in spin valve JJs configurations, where the presence of buffer layers improve the switching properties of the F layer but prevents the direct contact between the F and S layers and, hence, the polarization of the S interface [64, 65, 66, 131, 132, 133, 134]. Thus, our new approach of using a thin layer of a strong ferromagnet, directly in contact with superconducting layers in SIsFS JJs is a fundamental issue to obtain clear signatures of IPE in the $I_c(H)$ curves at low temperatures.

Moreover, the measurements of the $I_c(H)$ curves by varying the temperature allow to identify the presence of the spin polarization of the Cooper pairs, even when different magnetic interactions coexist at the S/F interface. Indeed in this framework, we can explain the inversion of the magnetic patterns in Fig. 3.6: if we compare Fig. 3.6 and Fig. 3.7, the trend of the $I_c(H)$ curves is practically the same unless a temperature-independent deviation of 1 mT. We can ascribe this behavior to a two-fold effect: i) a temperature dependent effect due to the spin polarization of the S/F interface as in Fig. 3.7 and ii) a response to the F stray fields that can arise, during the magnetization reversal of a larger volume of F, from the edges of the devices, from domain walls, and from surface roughness [135]. The F stray fields can induce a paramagnetic-like Meissener effect [95, 128] or the pinning of the Abrikosov vortexes [105]. Since the phase drop ψ across the sFS side of the JJ is negligible, the resulting induced fields lead just to a phase shift φ in the same sweeping direction of the applied field [136]. Nevertheless, these contributions do not depend on the temperature in the range of the measurements in Fig. 3.6 (compare with Fig. 3.5), whereas we expect a strong dependence of the magnetization induced in the superconductor M_{SC} for this range of temperature. Therefore, the temperature behavior of the $I_c(H)$ curves

allows to distinguish the source of magnetic interactions at the S/F interface. Finally, these findings are not only an important step forward in improving the description and understanding of proximity-coupled systems, but are also critical in implementation of these JJs in memory applications. An improvement for the memory test can be seen also as an increasing of the spacing between the higher and lower critical current levels at a fixed field, as it can be easily seen in Fig. 3.7. For this junction at $T = 4.2$ K, the maximum distance between the two critical current levels is just of about 20%, whereas by increasing the temperature just by a 1 K degree, at $T = 5$ K the difference between the two critical current levels increases up to more than 90%.

However, with a view of exploiting MJJs switches as active elements in quantum circuits down to $T = 10$ mK, the full screening of the F magnetic moment and the resulting lack of the hysteresis can be regarded as a drawback. In the next Chapter, we will show that this issue has been solved by realizing SIsFS JJs based on Al technology. In this case, a thin natural AlO_x barrier forms at the S/F interface and decouples the s and F layers: as a consequence, the spin polarization of the S/F interface is weakly induced resulting in an ordinary hysteresis of the $I_c(H)$ curves even at $T = 10$ mK. This experimental observation is in agreement with the theoretical predictions that emphasize that a highly transparent S/F interface is a decisive factor to observe the full screening at low temperatures (Fig. 3.11c). In more general terms, these results show how important the study of magnetic interactions at the interface S/F interface is for the correct use and design of MJJs as magnetic switches.

Chapter 4

Tunnel MJJs for hybrid quantum architectures

MJJs have been mostly used as passive elements in quantum circuits because of their intrinsic high quasiparticle dissipation. However, recent capabilities in coupling ferromagnetic layers with an insulating barrier and in exploiting intrinsic insulating ferromagnetic materials inside MJJs have opened the possibility to implement JJs in hybrid quantum architectures.

In this Chapter, we first examine the principal notions of the *transmon*, the most extensively adopted superconducting qubit, and we show that the memory properties of MJJs can provide an alternative tuning of the qubit frequency by means of magnetic field pulses in the so-called *ferro-transmon* configuration [137]. Since most of the superconducting qubits rely on Al JJs, we have transferred the notions and the recipe optimized for Nb tunnel SIsFS JJs (Chapter 2) to realize JJs with aluminum electrodes. We demonstrate that Al/AlO_x/Al/Py/Al JJs combine the very high-quality of tunnel Al SIS junctions, which are suitable for the integration in a trasmon, with the magnetic hysteretic behavior of the Josephson critical current. Moreover, this configuration ensures easy integration of JJs in a wide variety of digital and quantum circuits through standard fabrication process, since the F layer can be deposited *ex-situ* without affecting the quality of the tunnel barrier and of the deposition system. Therefore, our results represent fundamental advances in integrating JJs in today's quantum architectures.

4.1 Superconducting qubits

Research on low-temperature JJs has been boosted by application demands [5] for superconducting digital circuits [61], highly sensitive magnetometers [138], and radiation detectors [139]. More recently, JJs have emerged as prominent building elements in large-scale superconducting quantum processors [140, 141]. One of the main advantages of the superconducting qubit, as compared to qubits made with atoms or ions, all well-known quantum system, is that its fabrication is fully compatible with the well-established integrated-circuit technology. In addition, such electrical circuits enable to design the parameters of qubits to a much greater extent, and sometimes also to tune these parameters *in situ* during an experiment [142].

In order to realize a superconducting qubit, the idea is to make a non-linear oscillator out of a JJ and use as computational basis only the two lowest energy states of the circuit. To understand this concept, consider the linear LC resonant circuit in Fig. 4.1a. The total energy of this circuit is:

$$H = \frac{Q^2}{2C} + \frac{\Phi^2}{2L}, \tag{4.1}$$

where Q is the total charge on the capacitor C. It is convenient to represent the total charge in terms of number of Cooper pairs $n = Q/2e$. Therefore, the total energy can be written in this form:

$$H = 4E_C n^2 + \frac{1}{2}E_L \varphi^2, \tag{4.2}$$

where $E_C = e^2/2C$ is the charging energy required to accumulate one Cooper pairs on the capacitor and $E_L = (\Phi_0/2\pi)^2/2L$ is the inductive energy. In order to proceed to a quantum-mechanical description of the system, we need to promote φ and n coordinates to quantum operators satisfying the *commutation relation*:

$$[\hat{\varphi}, \hat{n}] = i, \tag{4.3}$$

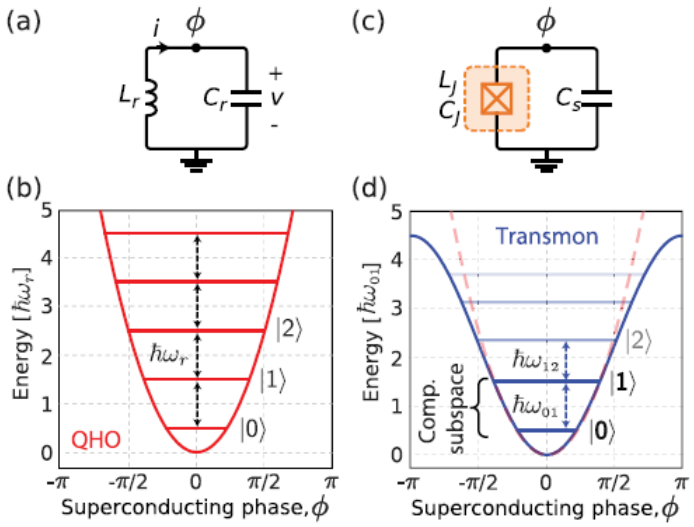

Figure 4.1. (a) Circuit for a parallel LC oscillator, with inductance L in parallel with capacitance C. (b) Energy potential for the QHO, where energy levels are equidistantly spaced $\hbar\omega_r = 1/\sqrt{LC}$ apart. (c) Josephson qubit circuit, where the non-linear inductance L_J (represented by the Josephson subcircuit in the dashed orange box) is shunted by a capacitance C_s. (d) The Josephson inductance reshapes the quadratic energy potential (dashed red) into sinusoidal (solid blue), which yields non-equidistant energy levels [143].

where the hat $\hat{}$ is used to indicate an operator. The quantum LC Hamiltonian resembles the form of a quantum harmonic oscillator (QHO) where the canonical operators of position and momentum are replaced by $\hat{\varphi}$ and $\hat{n}$, respectively, and the capacitance C and the inductance L play the role of an inertial mass and elastic constant. The quadratic potential energy in Equation 4.2 leads to eigenstates of equally spaced energy levels, i.e., $E_{k+1} - E_k = \hbar\omega_r$ with $\omega_r = 1/\sqrt{LC}$ (Fig. 4.1a). Thus, the LC resonator is not a good qubit, because we need to define a computational subspace consisting of only two energy states, which can be uniquely addressed at a frequency ω_{01} without exciting higher-level states.

We can modify the form of the potential energy by replacing the linear inductance of the QHO with a JJ playing the role of a non-linear inductor. As a matter of fact, combining the two Josephson relations (Equations 1.1 -1.3) with the standard definition of inductance $V = L(dI/dt)$, we obtain the Josephson inductance:

$$L_J = \frac{\Phi_0}{2\pi I_c \cos\varphi}, \tag{4.4}$$

which is non-linear with respect to phase φ. Similarly to quantization of QHO (Equation 4.2), we can write down the Hamiltonian:

$$\hat{H} = 4E_{C\Sigma}\hat{n}^2 + E_J\left[1 - \cos\hat{\varphi}\right], \tag{4.5}$$

where $E_{C\Sigma} = e^2/(2C_\Sigma)$, with $C_\Sigma = C_S + C_J$ is the total capacitance including the intrinsic Josephson capacitance C_J and the shunt capacitance C_S, and E_J is the Josephson coupling energy (Equation 1.13). The introduction of the non-linear Josephson inductance breaks the energy level degeneration of the LC circuit, thus, allowing to isolate the ground and the first excited states, characterized by a transition frequency ω_{01}, from the higher-energy levels (Fig. 4.1b).

As quantum mechanical objects, superconducting qubits can be coherently controlled, placed into quantum superposition states, exhibit quantum interference effects, and become entangled with one another. The time scale over which a superconducting qubit maintains this type of quantum mechanical behavior, and thereby remains viable for quantum information applications, is generally called the *coherence time*. The rate at which the qubit loses coherence is related to its interactions with the uncontrolled degrees of freedom in its environment [144]. The system dynamic and the sensitivity to specific noise sources are governed by the dominant energy in Equation 4.5. When $E_J/E_C \ll 1$, the charge number n is well defined and φ has large quantum fluctuations, and the qubit becomes thus highly sensitive to charge-noise. While for $E_J/E_C \gg 1$, the qubit is more sensitive to phase or flux-noise. However, it has been proven that charge-noise is more challenging to mitigate than flux-noise [143]. Thus, over time, the superconducting qubit community has converged towards circuit designs within the opposite limit ($E_J/E_C \gg 1$). To access the $E_J/E_C \gg 1$ regime, one preferred approach is to make the charging E_C small using large shunt capacitances, a circuit commonly known as the *transmon* qubit [145].

However, the protection to charge-noise costs a decrease in the anharmonicity of the system, defined as:

$$\alpha = \omega_{12} - \omega_{01}. \tag{4.6}$$

In the limit $E_J/E_C \gg 1$, the energy levels E_m of the transmon are well-approximated by [145]:

$$E_m = -E_J + \sqrt{8E_J E_C}\left(m + \frac{1}{2}\right) - \frac{E_C}{12}\left(6m^2 + 6m + 3\right). \tag{4.7}$$

From this, we obtain the qubit transition frequency:

$$\omega_{01} = \sqrt{8E_J E_C} - E_C \tag{4.8}$$

and the anharmonicity:

$$\alpha \sim -E_C. \tag{4.9}$$

A detailed analysis using a perturbation theory shows that the decrease in sensitivity to charge-noise is exponential in $\sqrt{E_J/E_C}$, while the anharmonicity only decreases linearly in $\sqrt{E_J/E_C}$ when scaled by ω_{01} [145]. Therefore, the trade-off is favorable. Typically, for a transmon with a qubit frequency ω_{01} in the range of 4 - 6 GHz, E_C is usually designed to be 200 – 300 MHz, while E_J/E_C is kept sufficiently large ($E_J/E_C \geq 50$) to suppress charge sensitivity [143].
Within this reasonable anharmonicity, we can consider the transmon circuit as a two-level system and describe it as a pseudo-spin with the Pauli operator σ_z:

$$\hat{H} = -\frac{\omega_{01}}{2}\sigma_z. \tag{4.10}$$

In the standard Bloch-Redfield picture, a qubit can be represented on the Bloch sphere as a quantum vector (Fig. 4.2):

$$|\psi> = \alpha\ |0> + \beta\ |1> = \cos\frac{\theta}{2}\ |0> + e^{i\phi}\sin\frac{\theta}{2}\ |1> \tag{4.11}$$

where $|\alpha|^2 + |\beta|^2 = 1$ for a pure quantum state, and $\theta \in [0, \pi]$ is the longitudinal angle, and $\phi \in [0, 2\pi)$ is the transverse angle. In a stationary frame, the Bloch vector precesses around the z-axis at the qubit frequency ω_{01}. It is easier to visualize the Bloch sphere in a reference frame where the x and y-axes rotate around the z-axis at the qubit frequency. In this rotating frame, the Bloch vector

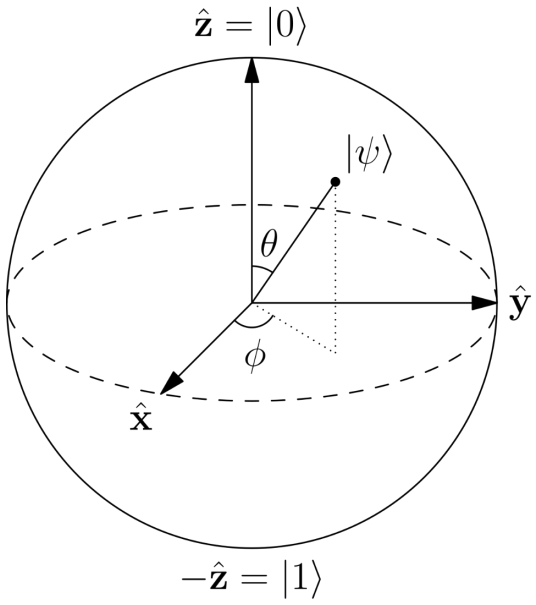

Figure 4.2. Bloch sphere representation of a quantum state: $|\alpha|^2 + |\beta|^2 = 1$.

appears stationary as in Equation 4.11.

Although the transmon qubit has addressed the fundamental issue of charging noise suppression, thus, increasing the coherence time from a few hundred nanoseconds to a few microseconds [146], it remains affected by various sources of noise that lead to decoherence and limit its performance and thereby the implementation of a scalable quantum processor. There are two decay rates that characterize decoherence processes:

$$\Gamma_1 = \frac{1}{T_1}, \tag{4.12}$$

$$\Gamma_2 = \frac{1}{T_2} = \frac{1}{2T_1} + \frac{1}{T_\phi}. \tag{4.13}$$

The longitudinal relaxation rate Γ_1 describes qubit energy loss to the environment in processes of relaxing from the excited state to the ground state. Therefore, noise sources in resonance with the qubit frequency mediate spurious decays between the excited and the ground state of the qubit. Typically, qubits relaxation noise sources are related to dielectric losses and two-level defects from materials, substrates or tunnel barrier junction [147, 148, 149, 150, 151, 152] and quasiparticle dissipation [23, 153, 154, 155].

The transverse relaxation rate Γ_2 is associated with the loss of the relative phase of the qubit state. Pure dephasing is characterized by $\Gamma_\phi = \frac{1}{T_\phi}$, and it can be due to noise sources in a wide range of frequencies, including $1/f$ charge, flux and current noise [143, 144, 156, 157, 158]. In this process, the frequency of the qubit fluctuates stochastically, and the Bloch vector precesses forward or backward in the rotating frame. This, eventually, leads to a complete depolarization of the azimuthal angle ϕ. Additionally, longitudinal relaxation also leads to decoherence, since losing the excited-state component of a quantum superposition state is a phase-breaking process [144].

4.2 Hybrid superconducting qubits

The study of relaxation and dephasing processes in transmon qubits made possible to understand the effect of different noise and microscopic physical phenomena occurring in superconducting devices: from the importance of material defects and losses to the quasiparticles dynamic in Josephson junctions. This study not only led to an improvement of circuit design, material quality and fabrication techniques, thus, increasing the coherence time from few microseconds to hundreds of microseconds [146], but most importantly it provides a powerful platform for investigating the rich phenomenology of Josephson devices. For instance, the voltage-controlled transmon, also known as a *gatemon*, employs semiconductor-coupled Josephson weak links as the non-linear element in the trasmon circuit. In this hybrid qubit the Josephson coupling energy can be tuned by changing the electron density in the semiconductor with a nearby side gate voltage V_G (Fig. 4.3). Voltage-controlled transmons have been realized with semiconducting nanowires [159, 160], two-dimensional (2D) electron gas proximitized by epitaxially grown superconductors [161], and recently graphene-based van der Waals heterostructures [162]. Over time, these systems have achieved temporal coherence comparable to that of typical transmon qubits based on SIS JJs [160].

For what concern the use of MJJs in quantum architectures, they have been mainly suggested as π-phase shifters for self-biasing quantum circuits and theoretically proposed as quiet qubits [163, 164, 165, 166, 167, 168]. For long time,

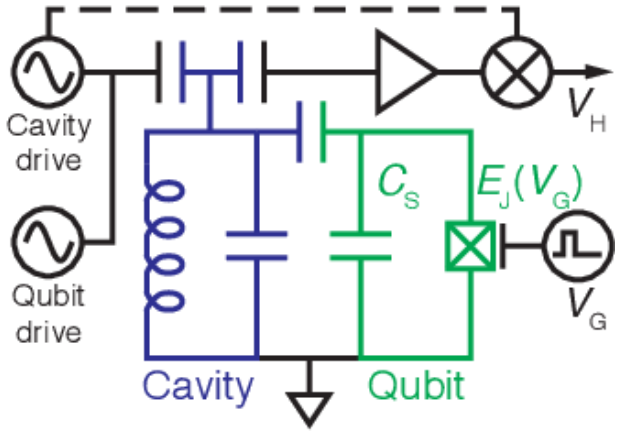

Figure 4.3. Schematic of the read-out and control circuit [159].

they have not been considered as active elements in quantum circuits, because of their intrinsic high dissipation that derives from the metallic nature of standard ferromagnetic barriers.

The dissipation in JJs is one of the major bottlenecks in the implementation of highly coherent quantum devices. Depending on the circuit design, it has a different impact on the system. For example, in phase qubits [169], the information is encoded as the ground and first excited states of a current-biased JJ and the qubit measurement relies on escape process that are governed by MQT phenomena. However, as shown by Caldeira and Leggett, in the presence of dissipation, MQT is suppressed [14] and high-dissipative JJs cannot be implemented as a phase qubit. As regards the charge qubit, non-equilibrium quasiparticles are known as an important decoherence mechanism, since quasiparticles hopping on and off the qubit island produce an unpredictable change in state. Engineering a Cooper pair box into the transmon regime ($E_J \ll E_C$) [145] exponentially suppresses the sensitivity of ω_{01} to charge-parity and background charge fluctuations. However, quasiparticle tunnelling remains a relevant source of relaxation and pure dephasing [22, 154, 170].

Recent advances in realizing MJJs by coupling ferromagnetic layers with insulating barriers inside (SIsFS or SIFS JJs) [57, 75, 85, 99] and by exploiting intrinsic

insulating ferromagnetic materials (SI_FS JJs) [171, 172, 173] have allowed both low quasiparticle damping and the transition to the MQT regime at low temperatures [174]. Therefore, the integration of JJs as active components in quantum circuits becomes an interesting perspective. In Ref. [137], a novel hybrid ferromagnetic transmon qubit, namely, a *ferro-trasmon*, has been proposed. After a brief introduction on the standard flux-tunable transmon, we examine the possible advantages of this novel hybrid circuit design [137].

Split-transmon

Qubit energies are mostly determined by the circuit parameters, but the possibility to tune the qubit energies post fabrication can be useful in order to adjust the transition frequencies and to implement multiple-qubit gates [175, 176]. For instance, in some cases, we need to bring two qubits into resonance to exchange energy, while we also need the capability of separating them during idling periods to minimize their interactions. To do this, we need an external tunable parameter [143]. One widely-used technique is to replace the single JJ with a loop interrupted by two JJs, forming a SQUID. Due to the fluxoid quantization condition:

$$\varphi_1 - \varphi_2 + 2\varphi_e = 2\pi m, \tag{4.14}$$

where $\varphi_{1(2)}$ are the phase drop across the JJs forming the loop, $\varphi_e = \pi\Phi_{ext}/\Phi_0$ is the normalized external flux and m is an integer number. The effective Hamiltonian of the so-called *split transmon* is:

$$H = 4E_C n^2 - 2E_J \left|\cos\varphi_e\right| \cos\varphi. \tag{4.15}$$

We can see that Equation 4.15 is analogous to Equation 4.5 with E_J replaced by $E_{J'}\left(\varphi_e\right) = 2E_J \left|\cos\varphi_e\right|$. The magnitude of the net effective Josephson energy $E_{J'}$ has a period of Φ_0 in applied flux. While the split transmon enables frequency tunability by the externally applied magnetic field, it also introduces sensitivity to random flux fluctuations. In the case of the split transmon, the external magnetic field threading the loop couples longitudinally to the qubit and modulates the

transition frequency via the Josephson energy E_J resulting in pure dephasing. At any working point, the slope of the qubit spectrum, $\partial\omega_{01}/\partial\Phi_{ext}$ indicates, to first order, how strongly this flux-noise affects the qubit frequency. The sensitivity is generally non-zero, except at multiples of the flux quantum $\Phi_{ext} = m\Phi_0$.
One recent development has focused on reducing the qubit sensitivity to flux-noise while maintaining sufficient tunability to operate quantum gates. The idea is to make two junctions in the split transmon asymmetric geometry by varying the junction area in the SQUID [157, 158] (Fig. 4.4). The total flux-dependent Josephson energy E_J varies according to the following expression [157]:

$$E_J(\varphi_e) = E_{J\Sigma}(\Phi_L)\cos(\varphi_e)\sqrt{1 + d^2(\Phi_L)\tan^2(\varphi_e)}, \tag{4.16}$$

where $E_{J\Sigma} = E_{J1} + E_{J2}$ and $d = (\gamma - 1)/(\gamma + 1)$ is the junction asymmetry parameter with $\gamma = E_{J1}/E_{J2}$. As we can see from the qubit spectra in Fig. 4.4d, the flux sensitivity is suppressed across the entire tunable frequency range. Therefore, by using a split transmon, one can maintain a sufficiently large tunability range, while reducing the susceptibility to flux-noise and, thus, improving coherence [158].

Ferro-transmon

The main idea of the *ferro-transmon* consists in integrating a MJJ in the SQUID loop of a transmon, schematically shown in Fig. 4.5a. The SQUID loop of the transmon is threaded as usual by an external flux, which is directed along the z-axis Φ_z and sets the standard cosinusoidal modulation of the SQUID Josephson energy [158]. However, compared to a conventional SQUID, the MJJs offer the possibility to tune I_c, and hence E_J, by acting with an external magnetic field pulse in the xy plane Φ_L (Section 2.1). Formally, the dependence of E_J on Φ_z and Φ_L is given by:

$$E_J(\Phi_z, \Phi_L) = E_{J\Sigma}(\Phi_L)\cos(\pi\Phi_z/\Phi_0)\sqrt{1 + d^2(\Phi_L)\tan^2(\pi\Phi_z/\Phi_0)}, \tag{4.17}$$

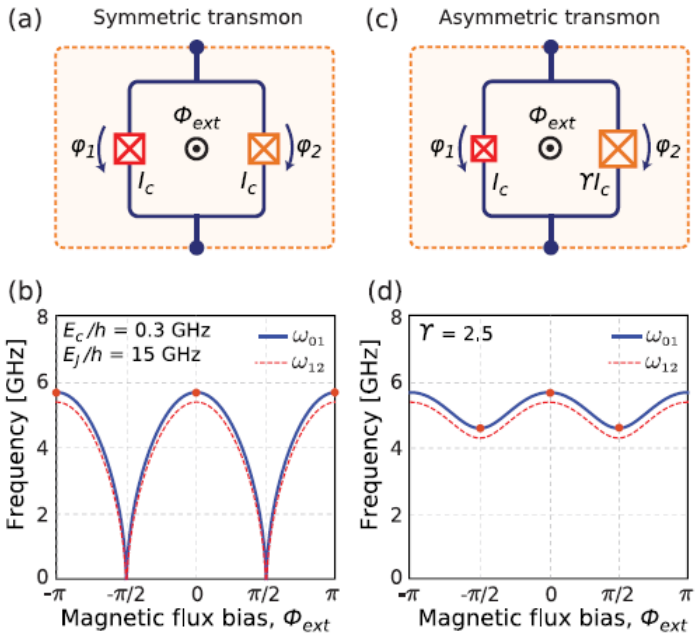

Figure 4.4. Modular representations for capacitively shunted SQUID and the corresponding qubit transition frequencies for the two lowest energy states as a function of the applied magnetic flux in units of Φ_0. (a) and (b) Symmetric split-transmon qubit, with Josephson energy E_J is shunted with a capacitor yielding a charging energy E_C. (c) and (d) Asymmetric split-transmon qubit, with junction asymmetry $\gamma = E_{J1}/E_{J2} = 2.5$ [143].

where $E_{J\Sigma}(\Phi_L) = E_J^{SIS} + E_J^{SFS}(\Phi_L)$.

The use of MJJs as memory element usually requires a magnetic field bias to set the optimal working point in order that ΔI is as large as possible. However, for this kind of application it is better to try to engineer the F barrier in order to exploit asymmetric minor loops, thus achieving finite ΔI at a zero-field working point [99]. In this way, it is possible to avoid application of the static magnetic field during qubit operations that may be detrimental for qubit coherence. This means that it may be worth exploring circuit design with a single JJ SFS, thereby completely eliminating the effect of flux-noise due to the static field [137]. Moreover, given the fact that tunnel SIsFS have been already demonstrated to be compatible with fast energy-efficient SFQ technology, this design allows the possibility to confine the control circuitry at cryogenic stages, and possibly improving scalability of the quantum processor.

Clearly, for the effective implementation of this design, the field pulses need to

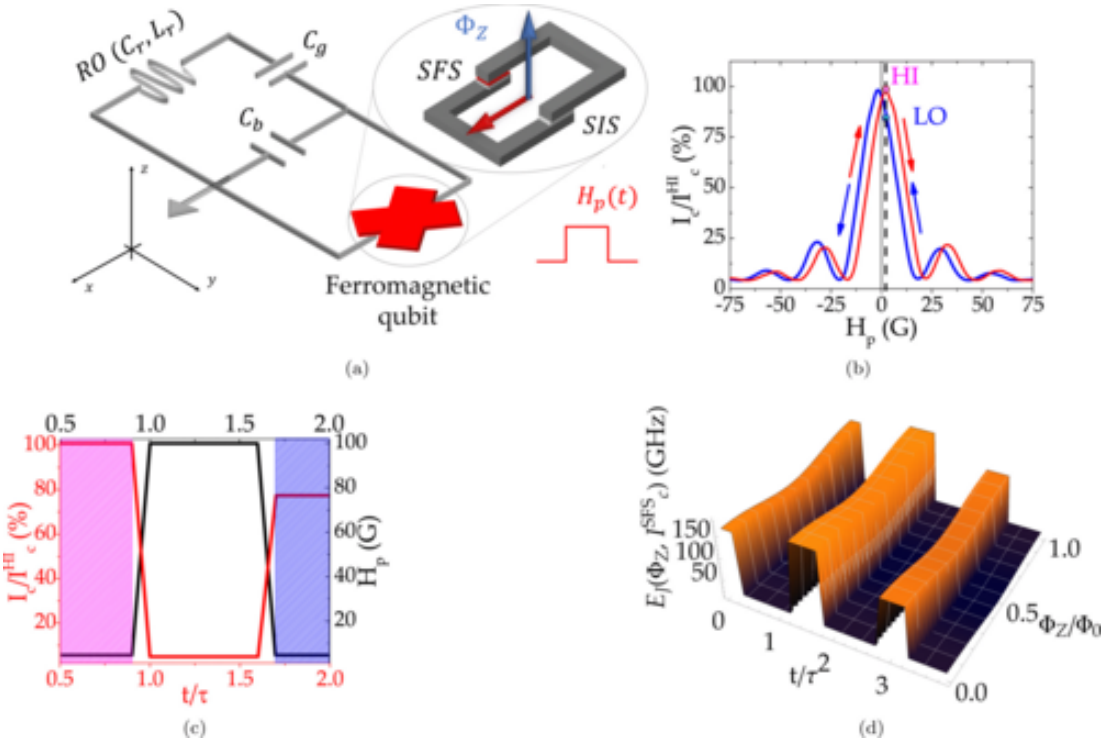

Figure 4.5. (a) Ferro-transmon circuit design: the read-out (RO) resonator is capacitively coupled to the qubit through C_g. The qubit is schematized as a hybrid SQUID in parallel with a bias capacitor C_b. Blue and red arrows indicate magnetic fields applied along the z-axis and the x-axis, respectively. (b) $I_c(H)$ modulation in a tunnel SI$_F$S JJ normalized to the maximum $I_c^{HI} = 350$ nA. Blue and red curves refer to the down and up curves, respectively. (c) Example of a magnetic field pulse sequence H_p (black line), and maximum digital tuning of the critical current I_c/I_c^{HI} (red line) for the MJJ shown in the panel (b). The blue and magenta dashed boxes refer to LO and HI levels, respectively. The time t is normalized to a magnetic pulse timescale τ. (d) Calculated total Josephson energy E_J of a hybrid SQUID characterized by a ratio $E_J^{SFS}/E_J^{SIS} \sim 10$ as function of the external flux Φ_z and of the magnetic field pulsed sequence $H_p(t)$ in panel (c) [137].

be longer than the time scale of the magnetization dynamics and shorter than time scale of the qubit operations. Typical magnetization dynamics occurs on a time scale $\tau <$ ns, which is far lower than the coherence time of trasmon qubit and current state-of-the-art single and two-qubit gate operations.

A first circuit analysis of the ferro-transmon in Ref. [137] provided an estimation of the charging energy $E_{c\Sigma}$, the ratio E_J/E_c, the qubit frequency ω_{01}, and the read-out coupling g, as a function of I_c^{SFS} and standard capacitances in the circuit. The analysis suggests the following ranges of values for the tunnel MJJs critical current in order to guarantee the transmon read-out, and suitable

frequency and anharmonicity values [137]:

- I_c^{MJJ} ranges from 40 to 65 nA for the hybrid d.c. SQUID configuration with $E_{c\Sigma} = 260$ MHz and $I_c^{SIS} = 30$ nA;

- I_c^{MJJ} ranges from 25 to 35 nA for the single tunnel MJJ configuration, once $E_{c\Sigma} = 200$ MHz is set.

These values guarantee a robust transmon regime, i.e., with E_J/E_c of the order of 50 – 100. Furthermore, as occurs in conventional transmon circuits based on the Al or Nb technology, $\omega_{01} < 10$ GHz, i.e., easily detected using standard qubit measurement equipment. Charging energies above ~ 200 MHz ensure sufficiently large anharmonicity to isolate a quantum two-level system [137]. Most importantly, the qubit frequency tunability through a pulsed local magnetic field ranges from $\Delta\omega_{01} \sim$ 0.8 GHz for the single tunnel-SFS JJ to 1 GHz for the hybrid d.c. SQUID configuration, as in typical flux-tunable transmons [158]. Such a tunability range corresponds to $\Delta I \sim 30\%$, which can be properly engineered even by exploiting minor magnetization loops.

4.3 MJJs with Al electrodes

With this proof of concept in mind, we have thus taken the first step towards the actual realization of a *ferro-trasmon* qubit: we have dealt with the fabrication and characterization of the building block of the circuit mentioned above, i.e., a tunnel switchable MJJ with suitable values of the critical current.

4.3.1 Fabrication

As addressed in the Chapter 2, our approach to use a strong ferromagnet allows in principle to scale our SIsFS JJs based on Nb technology down to submicron dimensions, thus, achieving the critical current values for the design mentioned above. However, in Fig. 3.7a, we haven't observed a magnetic hysteresis at very low temperatures: the full screening of the F magnetization is a drawback for this kind of application. Moreover, while Nb serves as the base material for most

of conventional superconducting digital circuits, quantum coherence times of Nb-based qubits are significantly shorter than those of their Al-based counterparts [177, 178, 179].

Two-angle evaporation process using a suspended electron-beam resist mask is presently the most widely used process for making submicron JJs [144] for a variety of superconducting qubit types [144, 180]. It appears to be most suitable for obtaining well-defined submicron Al/AlO_x/Al JJs, as the native oxide results in high-quality and reproducible tunnel barriers with reliable characteristics and low density of microscopic two-level systems. Indeed, the reproducibility of JJs is an important issue to ensure predictability of qubit frequencies, in order to enable pulsed-microwave control while avoiding cross-talk, a necessary requirement for scaling up beyond a few coupled qubits [143, 181].

Therefore, considering that superconducting quantum circuits rely almost exclusively on Al based JJs, for an integration of JJs in actual quantum circuits, we have adapted the recipe for Nb tunnel SIsFS JJs (Chapter 2) to the fabrication of JJs with aluminum electrodes. As far as we know, the Josephson effect in JJs based on Al technology has not yet been reported [182]. Moreover, also this procedure, known as SNAP, is well-established for niobium [183, 184] and is an element of novelty to use for realizing aluminum JJs [185]. The process has been discussed in detail in Section 2.2.3, here we recall just the main steps.

- An Al/AlO_x/Al trilayer has been deposited in an ultra-high vacuum system by DC magnetron sputtering onto an oxidized 3-inch Si wafer and patterned by optical lithography. The thicknesses of the base and top Al layers are 200 and 35 nm, respectively. The AlO_x tunnel barrier is obtained by filling the chamber with dry oxygen up to 200 Torr after the bottom layer deposition.

- After the lift-off procedure, the JJ areas have been defined by optical lithography and obtained by an anodization process in which the top Al layer has been completely anodized at a constant current value. A further insulation is given by a 150-nm-thick film of SiO_2, deposited by RF magnetron sputtering. The nominal dimension of the area of the JJs ranges from 80 to 12

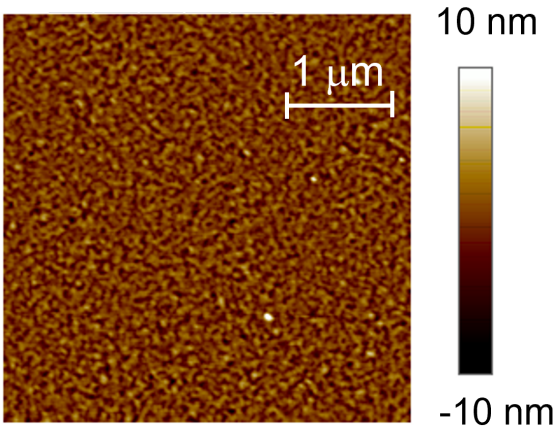

Figure 4.6. Topography maps (4μm $\times$ 4μm) obtained by AFM for a Al (30 nm) /Py (3 nm) bilayer after the etching cleaning as described in the text.

μm^2.

- In the following step, the 3-nm-thick Py layer has been deposited by DC magnetron sputtering after soft Ar ion cleaning to remove $\sim$ 5 nm of the top Al surface after vacuum breaking. In contrast to the niobium process (Fig. 2.8), the ion-etching deteriorates the Al/Py interface resulting in a mean-square-root roughness $R_q \sim 1.4$ nm (Fig. 4.6). However, as we will see in the next Section, a poor S/F interface does not affect the transport properties of the JJ, but rather decouples the SIs JJ from the side sFS, leading to an almost ideal tunnel-like behavior of the overall structure.

- Finally, a 350-nm-thick Al counter electrode has been deposited by a further DC sputtering and patterned by lift-off processes obtaining the overall SIsFS structure.

As a reference, we have also fabricated conventional SIsS JJs from the same wafer by excluding the F layer deposition step. In Fig. 4.7, we report an optical image of a junction set and a circular junction having an area of about 12 μm^2 in the inset.

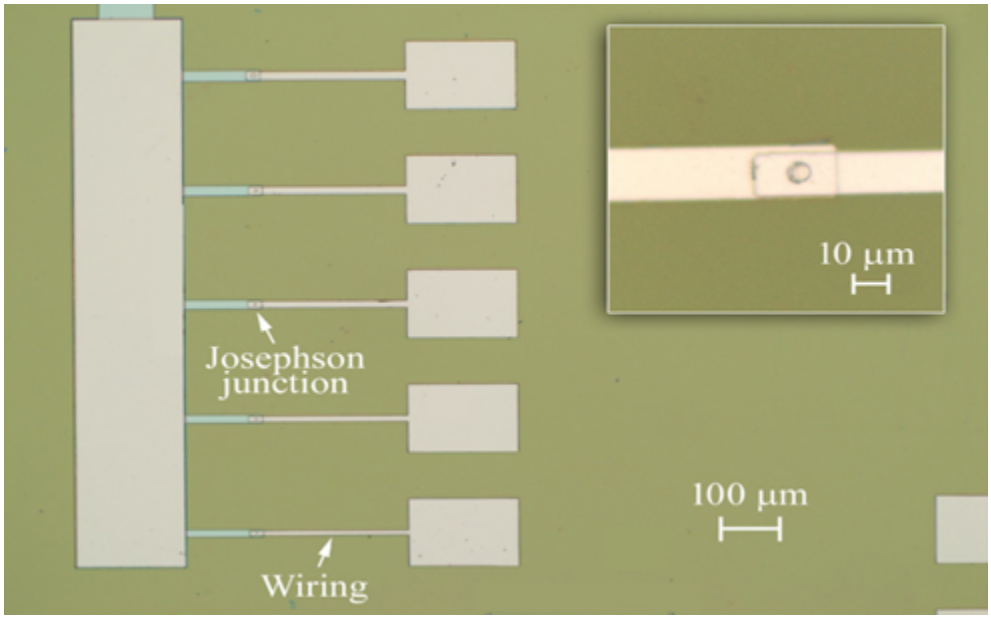

Figure 4.7. Optical microscope image of a set of circular SIsFS having a diameter D ranging from 2 to 10 μm. In the inset, the magnification of a circular junction with $D = \mu$m is displayed [185].

4.3.2 I-V curves and temperature dependence

Typical I–V curves and conductance measurements for SIsS and SIsFS junctions with a diameter $D = 4$ μm at $T = 10$ mK are reported in Fig. 4.8. The critical current density j_c is about 0.4 A/cm^2, which is almost independent of the junction area. Both SIsS and SIsFS JJs show the high-quality of the tunnel barrier that is evident from the shape of the subgap branch and that can be described in the frame of the TJM model (Section 1.1.3). By fitting the I–V characteristics in Fig. 4.8 with the TJM model, we have estimated a subgap resistance R_{sg} of the order of a few MΩ for both the SIsS and SIsFS JJs [182]. This estimation is in agreement with the conductance measured in the subgap region and values of retrapping currents, measured to be lower than 0.5 nA, which is the resolution limit of our experimental setup. The R_{sg} values are of the same order of magnitude as those of conventional SIS junctions commonly used as components in quantum circuits [186]. In the conductance measurements shown in Fig. 4.8b, we observe an appearance of two symmetric structures at $V \sim 200$ μm; i.e., at a voltage $V \sim V_{gap}/2$ with V_{gap} the voltage gap of the junction. These structures are not specific features of MJJs and can be found in standard tunnel JJs as

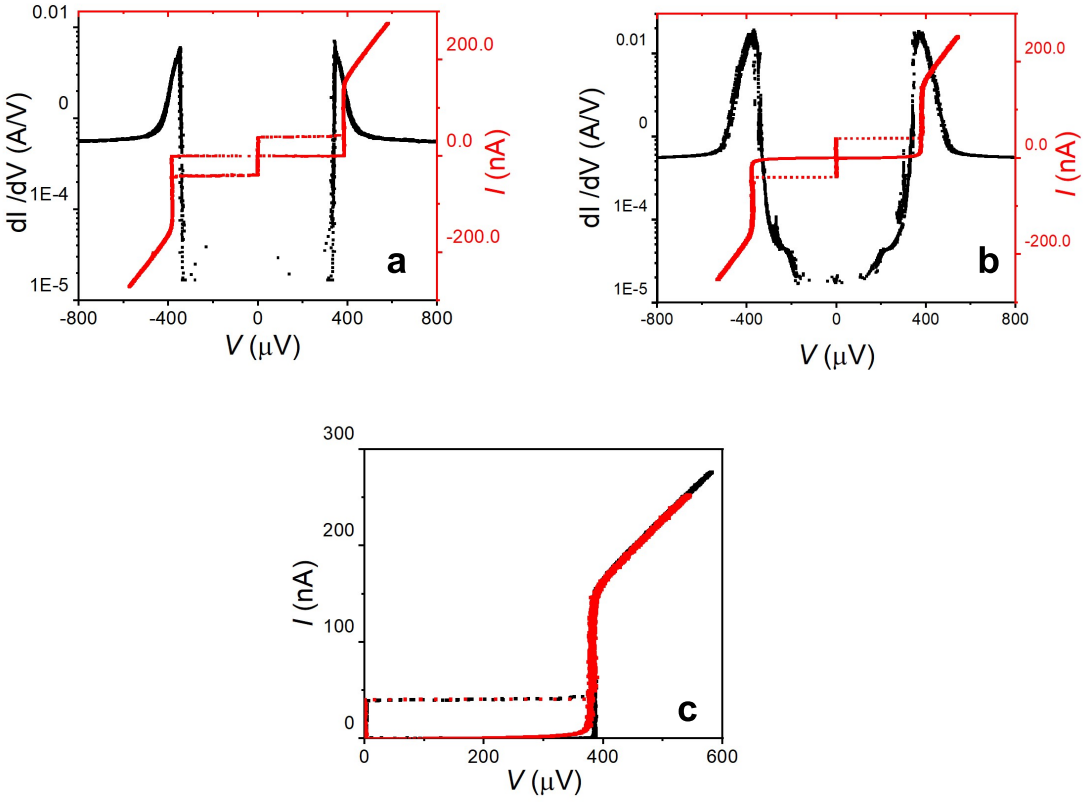

Figure 4.8. Conductance dI/dV measurement and I–V curve for (a) the SIsS JJ with $D = 4$ μm and (b) SIsFS JJ with $D = 4$ μm. The conductance measurements have been performed by applying a magnetic field of 10 mT to suppress the Josephson supercurrent. (c) Magnification of the positive part of the I–V curve for both the SIsS (black curve) and the SIsFS (red curve).

JJs	D (μm)	j_c (A/cm^2)	R_N (kΩ)	I_cR_N (μV)	R_NA (k$\Omega\mu$m^2)	Q	E_J (μeV)
SIsS	4	0.32 $\pm$ 0.07	1.7	66 $\pm$ 5	21 $\pm$ 4	12	82 $\pm$ 5
SIsFS	4	0.33 $\pm$ 0.07	1.8	76 $\pm$ 4	23 $\pm$ 05	12	83 $\pm$ 0.4
SIsFS	10	0.43 $\pm$ 0.09	0.2	65 $\pm$ 7	15.3 $\pm$ 3.2	9	700 $\pm$ 70

Table 4.1. Parameters of circular JJs based on Al technology at $T = 10$ mK: type of JJs, diameter D, critical current density j_c, normal resistance R_N, product normal resistance per critical current I_cR_N, product of the normal resistance per area R_NA, quality factor Q, and Josephson energy E_J.

well [187], where they are typically ascribed to a coherent tunneling mechanism of multiple quasiparticles [188, 189]. By comparing the I-V characteristics it is evident that the presence of the Py layer does not affect the transport properties of the measured junctions (Fig. 4.8c).

The characteristic voltage I_cR_N is about 25% of the expected AB value (Equation 1.36). The suppression of I_c could be related to the presence of paramagnetic impurities [190] or oxygen vacancies in the insulating barrier [191]. However, it is precisely this small value of I_c that leads to the value of the Josephson energy $E_J(\sim 80\ \mu\text{eV} = 20$ GHz) compatible with the ferro-transmon design in Section 4.2 [137]. Moreover, the suppression of I_c has been already observed in JJs employed in quantum circuits and does not seem to affect their coherence time [186]. Finally, according to the established empirical relation [89]: $1/C_s(cm^2/\mu F) = 0.2 - 0.0043 \log_{10} j_c(kA/cm^2)$, a specific capacitance for AlO_x barrier C_s is determined to be $\sim 80 fF/\mu\text{m}^2$; thus, a quality factor Q, of order of ~ 10, for all the junctions is obtained. We refer to Table 4.1 for a review of the main parameters of these junctions at $T = 10$ mK.

Measurements as function of temperature up to T_c ($\sim$ 1.3 K) are reported in Fig. 4.9. Panel (a) shows the temperature behavior of the I–V characteristics: from each curve, the gap voltage $V_{gap} = 2\Delta/e$ (Fig. 4.9b) and the I_cR_N product (Fig. 4.9c) have been extracted. The experimental temperature dependence $V_{gap}(T)$ follows the BCS approximation in the weak-coupling limit: $V_{gap}(T) = \frac{2\Delta_0}{e} \tanh\left(1.74\sqrt{1 - \frac{T}{T_c}}\right)$ [1]. The fit reported in Fig. 4.9b provides the zero temperature $2\Delta/e = 390\ \mu$eV and $T_c = 1.3$ K, which are the same

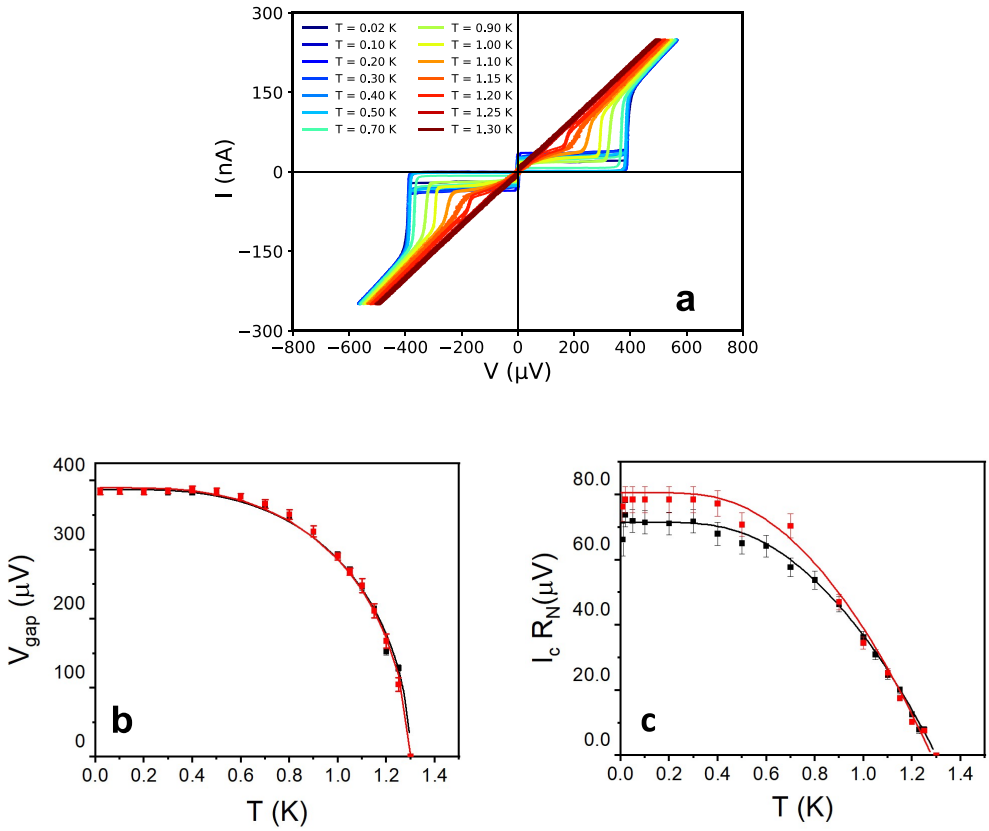

Figure 4.9. (a) Measurements of the I–V characteristics for a circular SIsFS junction with $D = 4$ μm as a function of the temperature T. For each curve, the values of the superconducting gap V_{gap} [panel (b)] and the characteristic voltage I_cR_N [panel (c)] have been determined. In both panels (b) and (c), the behavior of SIsFS JJ (red points) has been compared with non-magnetic SIsS JJ with $D = 4$ μm (black dots) and fitted (red curves) by using the BCS equation for the superconducting gap [panel (b)] and the AB relation for the I_cR_N product [panel (c)].

for SIsFS and SIsS junctions. The $I_cR_N(T)$ curves follow the AB relation [42]: $I_cR_N(T) = A\frac{\pi}{2e}\Delta(T)\tanh\left(\frac{\Delta(T)}{2k_BT}\right)$. In this case, we have introduced a coefficient A to taken into account the suppression of the critical current with to respect to the ideal case (Equation 1.36).

JJs	D (μm)	$2\Delta_0$ (μV)	T_c K	A
SIsS	4	390 ± 2	1.30 ± 0.01	0.23 ± 0.01
SIsFS	4	391 ± 2	1.28 ± 0.02	0.27 ± 0.04

Table 4.2. Parameters of the fit in Fig. 4.9b and 4.9c for circular JJs based on Al technology with diameter D: the energy gap at $T = 0$ K Δ_0, the critical temperature T_c and the coefficient A that takes into account the suppression of I_cR_N product compared to the AB expected value (Equation 1.36).

From the parameters in Table 4.1 and the fitting parameters reported in Table 4.2, we can conclude that the developed multi-step fabrication procedure allows building magnetic tunnel JJs preserving all the features of Al tunnel JJs. There are two possible scenarios for this experimental observation.

- For thin Al films, it is well known that the superconducting critical temperature T_c and hence the energy gap $\Delta = 1.764\ k_BT_c$ depend on the film thickness [192, 193]. For thicknesses greater than ∼3 nm, the phenomenological dependence of the Al gap on thickness d is of the form $\Delta(d) = \Delta_{bulk} + ad^{-1}$, where the $\Delta_{bulk} \simeq$ 180 μeV is the gap in the bulk limit and a is a parameter that depends on the details of the deposition process [194]. For the set of measurements in Fig. 4.9, the pair potential in the s interlayer is even larger than the one in electrodes and the SIsFS can be considered as a serial connection of a tunnel SIs JJ and a ferromagnetic sFS. Since $I_c^{SIs} \ll I_c^{sFS}$, the I-V curve of the overall SIsFS device is determined by its SIs part and the product I_cR_N can reach its maximum value corresponding to a standard SIS JJ [58, 59] (Section 1.3).

- Another scenario, which would explain the almost identical behavior of magnetic and non-magnetic JJs, is based on the fact that the Al interlayer

s does not experience any exchange field, since a thin natural AlO_x barrier decouples the Al from the ferromagnetic layer and eliminates the exchange coupling at the interface, as previously studied from the tunneling conductance of junctions formed on thin films of Al in contact with films of the ferromagnetic semiconductors europium oxide (EuO) and europium sulfide (EuS) [195, 196].

As a result, the SIsFS JJs with Al electrodes ensures an easy integration of JJs in a variety of digital and quantum circuits through standard fabrication procedures, since the F layer can be deposited afterword without affecting the overall transport behavior of the SIS JJs.

4.3.3 Magnetic hysteresis of the Josephson critical current

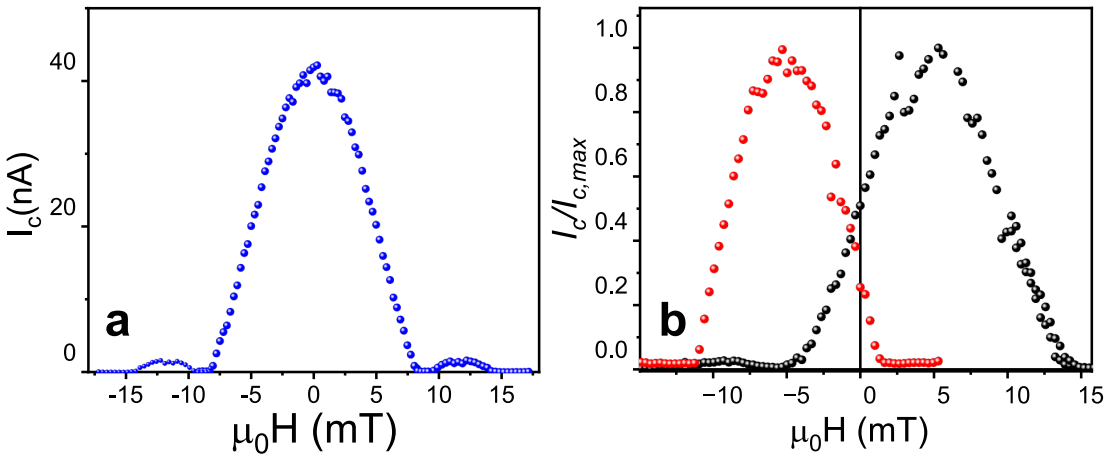

Figure 4.10. (a) Magnetic field patterns measured for the SIsS junction with $D = 4$ μm, showing the familiar Airy diffraction pattern. (b) Hysteretic behavior of the $I_c/I_{c,max}$ vs H curve for a SIsFS with $D = 4$ μm. The black and the red curves are the magnetic patterns in the downward and upward direction of the magnetic field, respectively. All the measurements have been performed at $T = 10$ mK.

In order to realize a magnetic switching device with hysteretic behavior of the critical current, it is crucial that $d_s < \lambda_L$. The dependence of I_c as a function of H at the base temperature of about 10 mK is shown in Fig. 4.10 for a SIsS JJs with diameter $D = 4$ μm, from which the Al London penetration depth can be determined $\lambda_L \sim 40\text{nm} > d_s$. Therefore, a hysteretic behavior of the $I_c(H)$

curves is expected.

Fig. 4.10 shows *$I_c(H)$* curves for a SIsFS junction with a diameter of 4 μm. We have first applied a field larger than 30 mT at $T = 4$ K $> T_c$ so that the F layer acquires a remanent magnetization and the Al electrodes don't trap flux. Thus, after cooling down to $T = 7$ mK in zero field, the *$I_c(H)$* curves acquire a magnetic hysteresis due to the F magnetization reversal [57, 62, 99](Fig. 4.10 b). These measurements demonstrate that SIsFS junctions based on Al technology can be used as switchable magnetic elements. Moreover, in these junctions an ordinary hysteresis of the $I_c(H)$ curves is observed. In this case, a thin natural AlO_x barrier may form at the S/F interface and decouple the s and F layers: as a consequence, the I-V characteristics are not affected by the exchange field in F and the spin polarization of the S/F interface is weakly induced, resulting in an ordinary hysteresis of the *$I_c(H)$* curves even at $T = 10$ mK. This result is in agreement with theoretical predictions. Also a high-transparent S/F interface is a decisive factor to observe a full screening at low temperatures (Fig. 3.11c). Moreover, we, clearly, move along a minor loop, since at the zero field we observe a distance between the two critical current levels $\Delta I \sim 50\%$. As a result, we can tune E_J of MJJ just with magnetic field pulses. To achieve a larger tunability, we may use a static field of ~ 5 mT in order to set a maximum distance between the two critical current levels $\Delta I \sim 95\%$.

In conclusion, we have realized and characterized tunnel MJJs based on Al technology. The use of a fabrication protocol typically employed for Nb based junctions, with JJs definition by the anodization process, represents an innovative procedure to obtain high-quality tunnel MJJs with Al electrodes. Typical hysteretic and switchable behavior as a function of the external magnetic field has been observed, preserving at the same time the high-quality transport properties of non-magnetic Al tunnel junctions, with quality factor larger than 10 and subgap resistance of the order of a few MΩ. These JJs have value of the Josephson coupling energy compatible with the *ferro-trasmon* design. Moreover, given the flexibility of an *ex-situ* deposition of a large variety of ferromagnetic materials without affecting the SIs side of the JJs, we can engineer *ad hoc* magnetic loops

to get the right tunability depending on the other circuit parameters.

In parallel, we are working to the design and fabrication of a resonator to couple with these MJJs [197]. These are fundamental steps towards the realization of hybrid S/F quantum platform, which may provide also new insights into the physics of hybrid JJs devices. In Ref. [137], a noise detection protocol has been proposed in order to distinguish the noise due the flux field and the one due the F magnetization. The magnetization noise spectrum at frequencies on-resonance with the qubit can be accessed through relaxation measurements at $d \sim 0$ and $\Phi_z \neq 0$. Magnetization fluctuations in a wider range of frequencies, including $1/f$ magnetization noise, can be instead accessed through dephasing measurements at the sweet-spots for the flux-field. Therefore, this platform can be potentially exploited as a magnetization-noise detector.

Conclusions and perspectives

In the pursuit of realizing a hybrid ferromagnetic quantum architecture, in this thesis we have designed, fabricated and fully characterized tunnel SIsFS JJs.

In Chapter 2, we have shown that the use of a strong ferromagnet, such as Py, in a SIsFS JJ allows to scale the junction dimensions to few μm^2. To our knowledge, our Nb-based SIsFS JJs are the smallest memory elements compatible in speed and power dissipation with SFQ logic [99]. Moreover, given the magnetic stability of Py, there are no particular limits for attaining submicron MJJs, e.g., by means of focused ion beam lithography [77, 56, 101, 102]. The achievement of a scalable energy-efficient memory is an important result for further developments of SFQ electronics, whose applications are still limited because of the lack of high-density RAM [61].

In the framework of quantum computing, SFQ circuits can provide supporting functions, such as read-out and control [198, 199], with the great advantage that can be located contiguously to the qubit chips. The implementation of a cryogenic co-processor represents indeed a key approach for the realization of a scalable quantum computer [100].

To date, the functionality of MJJs as switchable elements for digital electronics [61] and for spintronic devices [51] has been demonstrated mostly at liquid-helium temperature. However, novel phenomena can emerge at temperatures of the dilution refrigerator. In Chapter 3, we have shown that in MJJs with a thin layer of a strong ferromagnet and with highly transparent S/F interface, the inverse proximity effect can lead to a lack of hysteresis and a broadening of the magnetic field pattern [121]. By measuring the $I_c(H)$ curves as a function of the temperature down to $T = 10$ mK, we have ascribed these unconventional features to the

spin polarization of the S/F interface [95, 96]. The thermal behavior of the $I_c(H)$ dependence shifts finds a direct correspondence with the theoretical predictions, confirming a consistent picture based on the crucial role of the characteristic scaling energies, i.e., superconducting gap Δ and magnetic exchange energy E_{ex} [129]. Our method overcomes the lack of experimental tools able to probe the magnetization at the S/F interface with a high spatial resolution and provides evidence that the temperature alone can be an additional knob for digital control of MJJs. Therefore, these findings are not only important steps forward in improving the description and understanding of proximity-coupled systems, but also for implementation of MJJs as switchable elements [129].

Finally, we have transferred the fabrication protocol employed for Nb based junctions, with JJs definition by selective anodization process to obtain MJJs with Al electrodes. The main result is the demonstration of the magnetic hysteretic behavior of the critical current and, at the same time, preservation of the high quality transport properties of Al tunnel junctions. These MJJs, characterized by a very low damping, present value of the Josephson coupling energy suitable for the actual integration into the ferro-transmon architecture [182, 185]. We believe that it is a first fundamental step towards the actual integration of MJJs as active elements in quantum circuits. Moreover, since the F layer can be deposited *ex-situ*, without affecting the SIs side of the JJs, we can employ a large variety of ferromagnetic materials and engineer *ad hoc* magnetic loops to get the right tunability depending on the other circuit parameters. For instance, we consider to dilute Permalloy with copper in order to the reduce the switching field of the ferromagnet [200]. Presently, in our group we are working on the design and fabrication of a resonator to couple to our SIsFS in order to investigate their RF response and then proceed to the realization of a ferro-transmon [197]. Finally, we expect that this hybrid quantum architecture will provide a novel spectroscopic tool for the ferromagnetic barrier dynamics and for investigation of magnetization fluctuations [137].

List of Publications

- H. G. Ahmad, V. Brosco, A. Miano, L. Di Palma, M. Arzeo, **R. Satariano**, R. Ferraiuolo, P. Lucignano, A. Vettoliere, C. Granata, L. Parlato, G. Ausanio, D. Montemurro, G. P. Pepe, R. Fazio, F. Tafuri and D. Massarotti, "Competition of Quasiparticles and Magnetization Noise in Hybrid Ferromagnetic Transmon Qubits". In: *IEEE Trans. Appl. Supercond.* 33 (2023), pp. 1-6.
  DOI: 10.1109/TASC.2023.3243197

- A. Vettoliere, **R. Satariano**, R. Ferraiuolo, L. Di Palma, H. G. Ahmad, G. Ausanio, G. P. Pepe, F. Tafuri, D. Massarotti, D. Montemurro, C. Granata, and L. Parlato, "High-Quality Ferromagnetic Josephson Junctions Based on Aluminum Electrodes". In: *Nanomaterials* 1.23 (2022).
  DOI: 10.3390/nano12234155.

- L. Parlato, D. Salvoni, M. Ejrnaes, F. Mattioli, A. Gaggero, F. Martini, D. Massarotti, D. Montemurro, **R. Satariano**, R. Ferraiuolo, F. Chianese, F. Tafuri, R. Cristiano, and G. P. Pepe, "Investigation of Superconducting Molybdenum Silicide Nanostrips and Microstrips for Single Photon Detectors". In: *J. Low Temp. Phys.* (2022).
  DOI: 10.1007/s10909-022-02821-w.

- D. Salvoni, M. Ejrnaes, A. Gaggero, F. Mattioli, F. Martini, H. G. Ahmad, L. Di Palma, **R. Satariano**, X. Y. Yang, L. You, F. Tafuri, G.P. Pepe, D. Massarotti, D. Montemurro, and L. Parlato, "Activation Energies in MoSI/Al Superconducting Nanowire Single-Photon Detectors". In: *Phys.*

Rev. Appl. 18 (2022), pp. 014006.
DOI: 10.1103/PhysRevApplied.18.014006.

- Vettoliere, **R. Satariano**, R. Ferraiuolo, L. Di Palma, H. G. Ahmad, G. Ausanio, G. P. Pepe, F. Tafuri, D. Montemurro, C. Granata, L. Parlato, and D. Massarotti, "Aluminum-ferromagnetic Josephson tunnel junctions for high quality magnetic switching devices". In: *Appl. Phys. Lett.* 120 (2022), pp. 262601.
  DOI: 10.1063/5.0101686.

- **R. Satariano**, L. Parlato, A. Vettoliere, R. Caruso, H. G. Ahmad, A. Miano, L. Di Palma, D. Salvoni, D. Montemurro, C. Granata, G. Lamura, F. Tafuri, G. P. Pepe, D. Massarotti and G. Ausanio, "Investigation of the Inverse Magnetic Hysteresis of the Josephson Supercurrent in Magnetic Josephson Junctions". In: *IEEE Trans. Appl. Supercond.* 32 (2022), pp. 1800105.
  DOI: 10.1109/TASC.2021.3129983.

- **R. Satariano**, L. Parlato, A. Vettoliere, R. Caruso, H. G. Ahmad, A. Miano, L. Di Palma, D. Salvoni, D. Montemurro, C. Granata, G. Lamura, F. Tafuri, G. P. Pepe, D. Massarotti and G. Ausanio, "Inverse magnetic hysteresis of the Josephson supercurrent: study of the magnetic properties of thin Niobium/Permalloy ($Fe_{20}Ni_{80}$) interfaces". In: *Phys. Rev. B* 103 (2021), pp. 224521.
  DOI: 10.1103/physrevb.103.224521.

- **R. Satariano**, L. Parlato, A. Vettoliere, R. Caruso, H. G. Ahmad, A. Miano, L. Di Palma, D. Salvoni, D. Montemurro, C. Granata, G. Lamura, F. Tafuri, G. P. Pepe, D. Massarotti and G. Ausanio, "Unconventional magnetic hysteresis of the Josephson supercurrent in magnetic Josephson Junctions". In: *2021 IEEE 14th Workshop on Low Temperature Electronics (WOLTE)* (2021), pp. 1-4.
  DOI: 10.1109/WOLTE49037.2021.9555441

- L. Parlato, D. Salvoni, M. Ejrnaes, A. Gaggero, F. Mattioli, F. Martini, H. G. Ahmad, D. Massarotti, D. Montemurro, R. Ferraiuolo, L. Di Palma, **R. Satariano**, F. Tafuri and G. P. Pepe, "Superconducting Molybdenum Silicide nanowires for single photon detectors".
  In: *2021 IEEE 14th Workshop on Low Temperature Electronics (WOLTE)* (2021)

- H. G. Ahmad, D. Massarotti, V. Brosco, A. Pal, A. Miano, L. Di Palma, **R. Satariano**, R. Caruso, D. Montemurro, P. Lucignano, G. P. Pepe, R. Fazio, M. Blamire, F. Tafuri, "Electrodynamics of tunnel ferromagnetic Josephson junctions: dissipation mechanisms and study of noise fluctuations".
  In: *APS March Meeting*, S47. 007 (2021)

- L. Parlato, R. Caruso, A. Vettoliere, **R. Satariano**, H. G. Ahmad, A. Miano, D. Montemurro, D. Salvoni, G. Ausanio, F. Tafuri, G. P. Pepe, D. Massarotti and C. Granata, "Characterization of scalable Josephson memory element containing a strong ferromagnet". In: *J. Appl. Phys.* 127 (2020), vol. , pp. 193901.
  DOI: 10.1063/5.0004554.

- L. Parlato, D. Salvoni, M. Ejrnaes, D. Massarotti, R. Caruso, **R. Satariano**, F. Tafuri, X. Y. Yang, L. Zou, Z. Wang, G. P. Pepe and R. Cristiano, "The Role of Multiple Fluctuation Events in NbN and NbTiN Superconducting Nanostrip Single-Photon Detectors". In: *J. Low Temp. Phys.* 199 (2020), pp. 6–11.
  DOI: 10.1007/s10909-020-02395-5.

Appendix A

Experimental set-up

In this Appendix, we present experimental setups used for fabrication, magnetic characterization, and transport measurements of thin-film heterostuctures and Josephson Junctions studied in this thesis.

A.1 Thin-films deposition systems

We have used mainly sputtering for the deposition of uniform metallic thin films during sample fabrication. Sputtering is a kinetic process where energetic particles, in our case ionized Ar atoms, are bombarded into a metallic target material of interest, ejecting a vapor of metallic atoms onto a nearby sample. The deposition rate can be made appreciable by confining the Ar ions using magnetrons that produce strong magnetic and electric fields. The ions undergo helical cyclotron motion along the magnetic field lines, leading to a cascading chain of ionization events with the surrounding gas, which at moderately low pressures ($< 10^{-2}$ Torr) can form a sustained plasma. Sputtering a mixture of elements or compounds will not result in a change of composition of the target and the vapor phase will be thus the same as the that of the target during the deposition [201]. We have used two different deposition systems: one for superconducting materials and another for ferromagnetic materials.

- The vacuum chamber, in which we deposit superconducting materials, e.g., Al or Nb, is equipped with two-inch magnetron sources powered by a DC

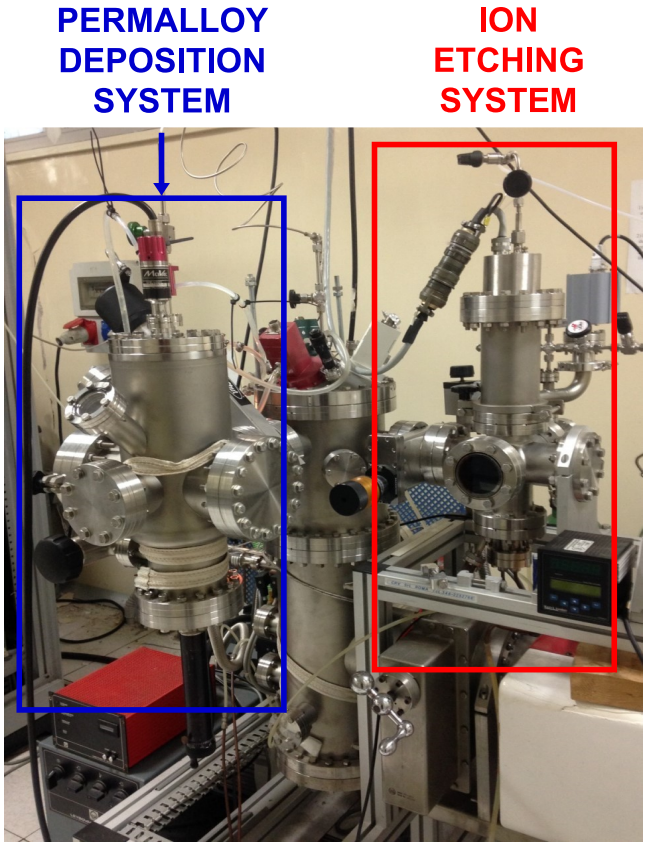

Figure A.1. Vacuum chamber for the Py deposition and for the ion etching.

or RF generator with a maximum power of 500 W. Inside the chamber, three-inch silicon wafers are placed on a rotating platform, driven by a programmable stepping motor and provided of six positions. Between the magnetrons and the rotating platform there is a fixed stage that allows to place only one sample at a time in correspondence with the source, thus, avoiding the others to be contaminated. The pumping system consists of a turbomolecular group with an ion pump and a titanium sublimator that allow to reach the base vacuum of about 10^{-9} torr.

- The second system consists of three vacuum chambers, connected by a valve, one for the etching process, one equipped with three magnetron sources, and the third containing a single magnetron source for the deposition of the Py (Fig. A.1). The distance between the target and the sample holder can be varied and it has been fixed at 15 cm. The sputtering chamber is equipped with a turbomolecular pump (assisted by a rotary pump) used to reach a

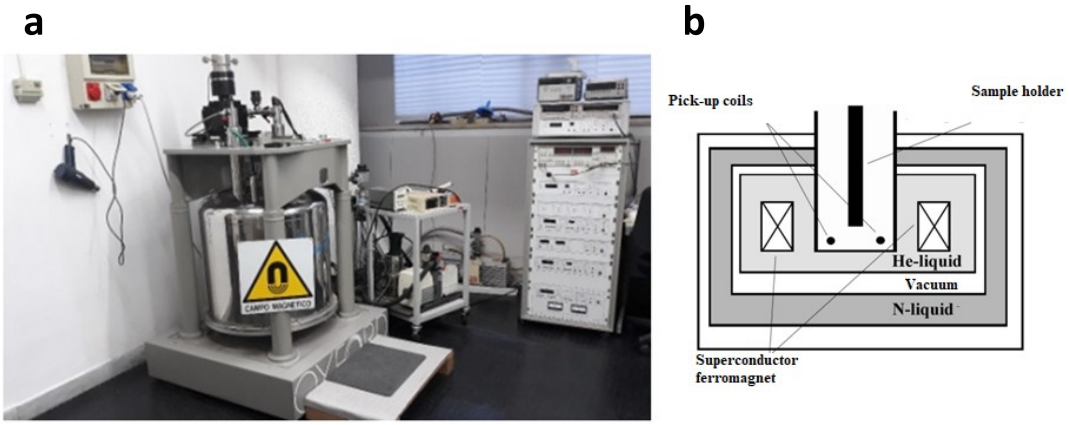

Figure A.2. (a) VSM and (b) sketch of the principle of working.

base pressure of $\sim 10^{-7}$ Torr.

A.2 Vibrating Sample Magnetometer

The magnetic moment of thin-film heterostrucures have been measured using a commercial Vibrating Sample Magnetometer (VSM) equipped with a He-flow cryostat of Oxford Instruments-MagLab (Fig. A.2a). The operating principle of the VSM is based on Faraday's induction law [202]. The sample is attached by thin strips of Teflon to the end of a non-magnetic rod, whose other end is fixed to a mechanical vibrator (Fig. A.2b). The specimen is oscillated between two pick-up coils in an environment, whose temperature is controlled by regulating the flow of helium gas from the cryostat filled with liquid helium, in which a superconducting magnet is immersed. The latter is a coil of Niobium-Titanium (NbTi) filaments embedded in a copper stabilizing matrix, and provides a magnetic field up to 9 T oriented parallel to the direction of oscillation. The oscillating magnetic field of the moving sample thus induces an alternating electromotive force (*emf*) in the detection coils, whose magnitude is proportional to the magnetic moment of the sample. The alternating *emf* is detected with a lock-in amplifier, which is sensitive only to the signal at the vibration frequency of the specimen (typically 55 Hz), recognized using a reference signal from the vibrator controller. The Oxford Instruments VSM allows measurements between 4 and 300 K via a heater, with a sensitivity of about 10^{-6} emu.

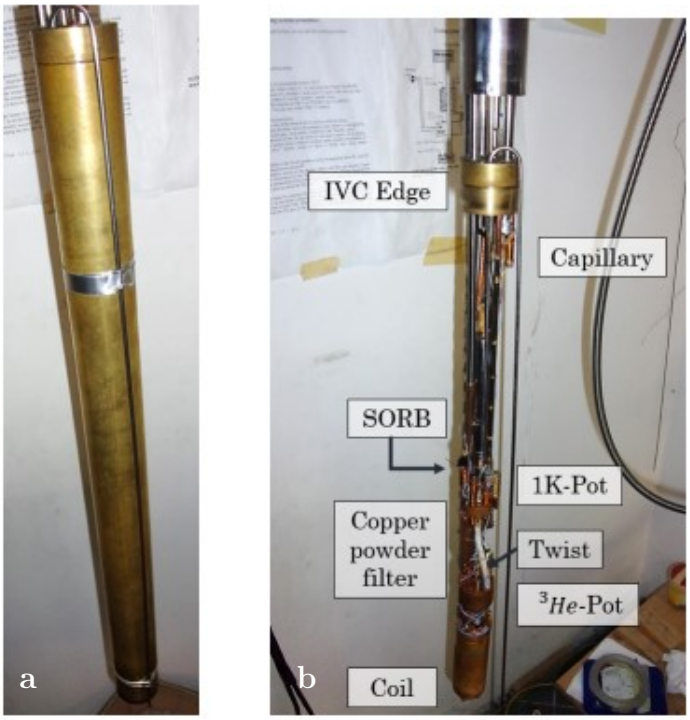

Figure A.3. (a) Outer and (b) inner view of IVC of the Heliox system.

A.3 The evaporation cryostat

Some cryogenic d.c. measurements down to 300 mK have been performed by using an evaporation cryostat HelioxVL provided by Oxford Instruments (Fig. A.3). During the measurements, the cryostat is sealed and vacuum is created inside the inner vacuum chamber (IVC) to provide thermal insulation from the main liquid ^{4}He bath (Fig. A.3a). The cryostat uses a ^{3}He closed dump to reach a base temperature of about 0.3 K. A thin capillary draws ^{4}He from bath to the 1-K-pot, where it is pumped with an external rotatory pump through a needle valve, thus reaching a temperature around 1.8 K. At this temperature, ^{3}He gas in the ^{3}He-pot liquefies. When most of the gas has condensed into the insert, the 1 K-pot needle valve is closed completely so that the pot cools to the lowest possible temperature for optimal condensation. At this stage, the ^{3}He pot is full of liquid ^{3}He at approximately 1.2 K. The sorption pump, made of a zeolitic material, the so-called *SORB*, is cooled below 30 K to absorb gas and begins thus to reduce

the vapour pressure above the liquid ^{3}He, so that the sample temperature drops. As the limiting pressure is approached, the temperature of the liquid ^{3}He can be reduced to 0.3 K.

A.4 The dilution refrigerator

To preform d.c. measurements down to $\sim$ 10 mK, we employ a Triton refrigerator system provided by Oxford Instruments. The fridge consists of several stages of progressively lower temperatures, enclosed in a cylindrical high vacuum chamber, referred as outer vacuum chamber (OVC). High vacuum is needed to prevent thermal exchange with the environment, and the pressure inside the chamber is lower than 10^{-5} mbarr. The stages are made copper gold-and silver-covered plates, thermally decoupled one from another by means of stainless-steel supports. As illustrated in Fig. A.4, starting from the top of the cryostat, we have:

- the RT-plate, at room temperature;
- the PT1, at $\sim$ 70 K;
- the PT2, at $\sim$ 4.2 K;
- the still-plate, at $\sim$ 0.7 K ;
- the IAP-plate, or cold-plate, at $\sim$ 0.1 K;
- the MC-plate, at $\sim$ 10 mK, which has a mixing chamber where the helium dilution process takes place.

The temperature of each plate is constantly monitored through semiconducting-resistor thermometers positioned on it. The vacuum cans are suspended from a shock damped top plate, which is at room temperature. There are several layers of heat shields protecting the inner layers from thermal radiation. The heat shields are brass cylinders mounted on the still plate, PT2 plate and PT1 plate, with which they are at thermal equilibrium.

There are two methods of cooling operations in the cryostat. The bulk of the heat removal from room temperature to cryogenic temperatures is achieved with a Pulse Tube Refrigerator (PTR), which removes heat by expansion of helium

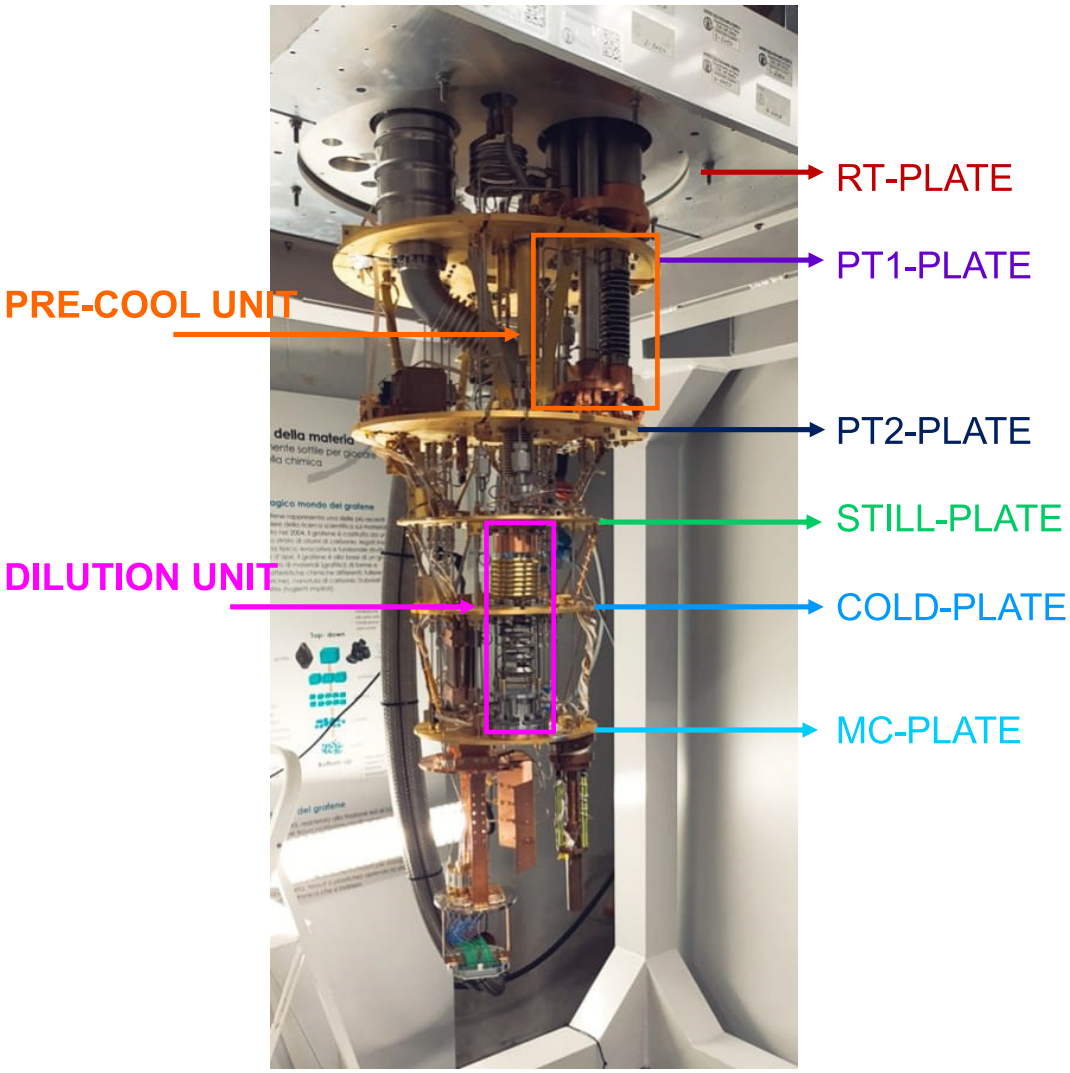

Figure A.4. Triton inner view.

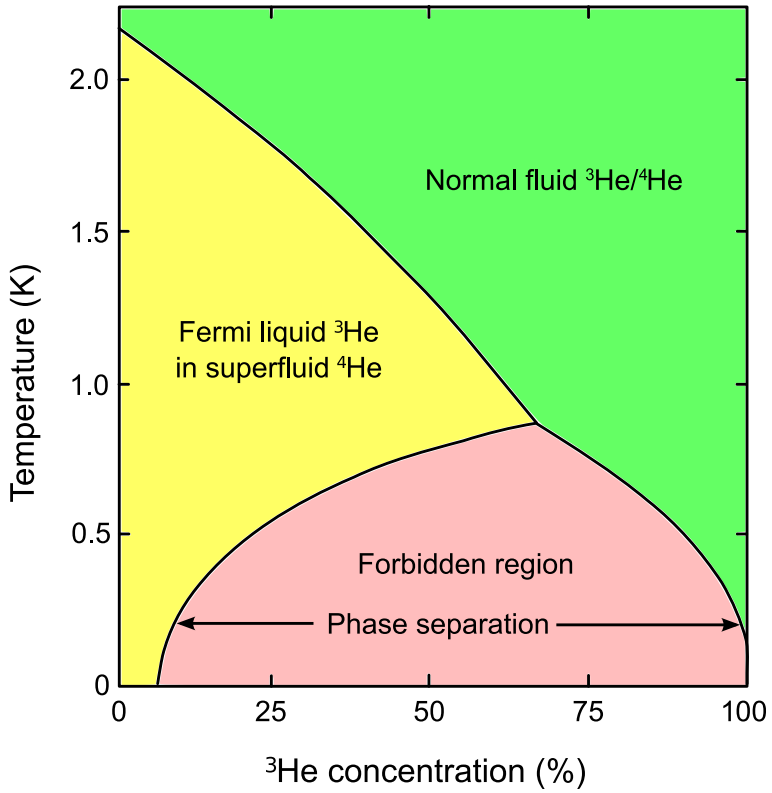

Figure A.5. Phase diagram of ^{3}He -^{4}He in terms of temperature and concentration of the mixture.

gas. The final cooling is done with helium dilution process, in which heat is removed by diluting liquid ^{3}He into liquid ^{4}He [203].

In the Pre-Cooling (PC) phase, a small amount of ^{3}He -^{4}He mixture gas stored in a tank is first cooled and purified in liquid nitrogen, and then is circulated through the pre-cool unit. A series of heat-exchangers improves the cooling efficiency. When the MC temperature reaches $\sim 10\ K$, the cooling of the MC will switch from using pre-cool unit to dilution unit. The system control will recollect mixture from the pre-cool lines. Then, the mixture is compressed using a high pressure ($\sim$ 2.5 bar) pump. The mixture is thus passed through a sequence of pressure impedance that exploits the Joule-Thompson effect to lower the temperature of the mixture to values of the order of 1 K.

At approximately 0.8 K, a mixture of ^{3}He and ^{4}He in the mixing chamber separates into two phases: a concentrated phase, consisting of mostly of ^{3}He and a dilute phase, composed mostly of superfluid ^{4}He with a small percentage of ^{3}He depending on the temperature. If the dilute phase is pumped on, ^{3}He boils

off preferentially to ^{4}He. To restore equilibrium, ^{3}He from the concentrated phase will diffuse into the dilute phase, and in crossing the phase boundary will extract heat from the MC, which is thermally connected to the sample. Temperatures as low as 10 mK can be reached in the cryostat using this method.
The control of the pumps, pressures, temperatures and valves in the cryostats is achieved with the use of an Intelligent Gas Handling system (IGH), driven by an Oxford Instruments LabVIEW software.

A.5 Filtering system and electronic set-up

Accurate measurement of the transport properties of JJs requires filters to reduce the electrical and thermal noise. The scheme of the d.c. lines in the Triton is inspired to the Heliox configurations. In the Heliox system, we can measure just two samples at time in a four-contact configuration. The Triton instead is equipped with 48 d.c. lines, 24 current-carrying lines and 24 voltage lines. Half of these lines (12 current lines and 12 voltage lines) are designed to be filtered and we can thus measure up to 6 samples at a time. The other lines can be used for other DC sample-stages that do not require a strong filtering, or for the monitoring of additional thermometers.
The materials used for electrical connections have been chosen in order to avoid the heating of the sample. From the RT-plate to the 4 K-Plate, I-lines and V-lines are twisted pairs in copper and constantan d.c. looms from Oxford instruments, respectively. From the 4-K-Plate to the MC-plate, instead, I-lines are in a NbTi d.c. loom from Oxford Instruments, while the V-lines are homemade manganin twisted cables. It has been chosen to use manganin at the coldest stages of the cryostat for the voltage lines due to its low heat conductivity [204]. Copper lines are, instead, characterized by a lower resistance compared with the voltage-lines, thus reducing heating when current-biasing the devices, whereas the NbTi is superconducting below 10 K, thus ensuring no heat dissipation at the coldest stages of the cryostat.
At the room temperature stage, electromagnetic interference filters have been mounted in order to reduce electromagnetic high frequency peaks such as the

ones coming from mobile phones. The next filtering stage consists in 12 RLC-π filters, one for each line, with a cut-off frequency of 1.6 MHz. These filters are anchored to the 1 K-pot in the Heliox system, whereas they are anchored to the still plate in the Triton.

At low temperature and above 10 MHz, the RC-filters losses in attenuation, so we need another filtering stage able to cut-off the signals at higher frequencies and install, at the IAP-Plate, two filters stages. In this case, both RC-filtered and unfiltered lines pass through the brass-powder filters. For both cryogenic systems, the first Copper powder filter is connected to the cold plate (about 50 mK), the second is thermally anchored to the MC.

Josephson devices must be shielded from external magnetic fields. While in the Heliox this is guaranteed by the screened dewar of the main bath, which is composed of a first screen of cryoperm and by a second one in lead, in the Triton the magnetic field screening is installed directly on the sample stage. The Triton sample-holders are designed to allocate lead and cryoperm magnetic field screens (Fig. A.4) around the samples.

All measurements are performed using a four-wire connection using aluminum wires, in order to exclude all the contribution to the resistance not due to the sample.

The junctions are current biased using an Agilent 33120A arbitrary wave-form generator. The frequency of the input signal is usually of about 1 Hz. The generated voltage difference passes through a unitary gain amplifier that decouples it from external noise and then goes on a tunable shunt resistance, usually much larger than the lines impedance, so that the measured device is current biased. Since a return current path is provided, it is also possible to directly measure the current passing through the junction. The measured output signal is the voltage across the junction, amplified using a variable gain amplifier.

Current versus voltage characteristics can be measured as a function of temperature and/or magnetic field, in order to obtain a wide characterization of the sample. Magnetic field is generated using a source meter Keithley 2400 connected to the superconducting coil.

For the differential conductance data dI/dV, the input current is the sum of two signals: a small sinusoidal excitation (dI), given by the internal oscillator of the lock-in amplifier with frequency of about 30 Hz, superimposed on a triangular ramp with a frequency of about 1 mHz (I) by using a summing amplifier. The quasi-d.c. output V due to the low frequency component of the bias is read using a standard multimeter. The output dV is read using a lock-in amplifier, which is used to compute the conductance dI/dV. A magnetic field, which corresponds to one of the minima of the $I_c(H)$ pattern, is applied to suppress the Josephson current in the junction.

Acronyms

AB Ambegaokar-Baratoff. 31, 32, 53, 54, 98–100

AFM Atomic Force Microsopy. 51, 53, 95

BCS Bardeen-Cooper-Schrieffer. 31, 32, 54, 98, 99

DOS density of states. 21, 29, 30

F Ferromagnet. 2, 4, 9, 27, 33–39, 42–44, 46, 47, 50–52, 55–59, 61–69, 71–81, 91, 93, 95, 101–103, 105, 106

GL Ginzburg-Landau. 27, 34, 46, 76

IPE inverse proximity effect. 61–65, 70, 71, 73, 76, 78, 79, 105

IVC inner vacuum chamber. 114

JJ Josephson Junction. 10, 12–14, 16, 17, 27, 31, 35–38, 42, 49, 55, 58, 65, 69, 71–73, 76, 79, 82, 83, 88, 89, 91–95, 97, 99, 100, 105

JJs Josephson Junctions. 1–4, 9, 13, 14, 17–19, 31, 32, 35–38, 41–44, 46, 47, 49, 50, 52, 54–59, 61, 65, 73, 74, 76, 78–82, 87–89, 93–96, 98, 100–103, 105, 106, 111, 118

MC mixing chamber. 115, 117–119

MJJ Magnetic Josephson Junction. 3, 43, 44, 90, 92, 93, 102

MJJs Magnetic Josephson Junctions. 2–4, 9, 35, 42, 61, 62, 66, 73, 80, 81, 87, 88, 90–92, 96, 102, 103, 105, 106

MQT Macroscopic Quantum Tunneling. 3, 18, 88, 89

N Normal metal. 19, 27–31

QHO quantum harmonic oscillator. 83, 84

RAM Random Access Memory. 3, 42, 105

RCSJ Resistively and Capacitively Shunted Junction. 14, 18

S Superconductor. 2, 4, 10, 19, 27–31, 33–36, 46, 47, 52, 57, 59, 61–65, 67, 69, 71, 76–80, 95, 102, 103, 105, 106

SEM Scanning Electron Microscope. 51, 53

SFQ Single Flux Quantum. 3, 41–43, 55, 59, 91, 105

SFS Superconductor/ Ferromagnet/ Superconductor. 3, 9, 35, 36, 38, 42, 65, 73, 76, 79, 91

sFS thin superconductor/ Ferromagnet/ Superconductor. 3, 9, 37, 38, 55, 58, 73–76, 79, 95, 100

SI$_F$S Superconductor/Ferromagnetic Insulator/ Superconductor. 3

SIFS Superconductor/ Insulator/ Ferromagnet/ Superconductor. 2, 36, 38, 55, 88

SIS Superconductor/ Insulator/ Superconductor. 2, 3, 9, 31, 32, 35, 37, 38, 42, 57, 81, 87, 96, 100, 101

SIs Superconductor/ Insulator/ thin superconductor. 3, 9, 37, 38, 55, 58, 69, 73, 74, 76, 95, 100, 102, 106

SIsFS Superconductor/ Insulator/ thin superconductor/ Ferromagnet/ Superconductor. 2–4, 9, 36–39, 41, 43, 44, 46, 47, 50, 53–59, 61, 70–74, 76, 79–81, 88, 91, 93–97, 99–102, 105, 106

SIsS Superconductor/ Insulator/ thin superconductor/ Superconductor. 47, 52–56, 72, 73, 95–97, 99–101

SNAP Selective Niobium Anodization Process. 49, 94

SNS Superconductor/ Normal metal/ Superconductor. 27, 31, 32

SQUID Superconductor Quantum Interference Device. 2, 89–93

SQUIDs Superconductor Quantum Interference Devices. 2

TJM Tunnel Junction Microscopic. 18, 19, 96

VSM Vibrating Sample Magnetometer. 45, 61, 66, 113

Bibliography

[1] A. Barone and G. Paterno. *Physics and Application of the Josephson Effect*. John Wiley & Sons, New York, 1982.

[2] V. V. Schmidt, P. Müller, and A. V. Ustinov. *The Physics of Superconductors: Introduction to Fundamentals and Applications*. Springer Berlin Heidelberg, Berlin, Heidelberg, 1997.

[3] P. W. Anderson and A. H. Dayem. "Radio-Frequency Effects in Superconducting Thin Film Bridges". In: *Phys. Rev. Lett.* 13 (6 1964), pp. 195–197. DOI: 10.1103/PhysRevLett.13.195. URL: https://link.aps.org/doi/10.1103/PhysRevLett.13.195.

[4] B. D. Josephson. "Possible new effects in superconductive tunnelling". In: *Physics Letters* 1.7 (1962), pp. 251–253. ISSN: 0031-9163. DOI: https://doi.org/10.1016/0031-9163(62)91369-0. URL: https://www.sciencedirect.com/science/article/pii/0031916362913690.

[5] F. Tafuri. *Fundamentals and Frontiers of the Josephson Effect*. Springer Series in Materials Science, 2019.

[6] A. A. Golubov, M. Yu. Kupriyanov, and E. Il'ichev. "The current-phase relation in Josephson junctions". In: *Rev. Mod. Phys.* 76 (2 2004), pp. 411–469. DOI: 10.1103/RevModPhys.76.411.

[7] S. Shapiro. "Josephson Currents in Superconducting Tunneling: The Effect of Microwaves and Other Observations". In: *Phys. Rev. Lett.* 11 (2 1963), pp. 80–82. DOI: 10.1103/PhysRevLett.11.80. URL: https://link.aps.org/doi/10.1103/PhysRevLett.11.80.

[8] W. C. Stewart. “Current-voltage characteristics of Josephson Junctions”. In: *Appl. Phys. Lett.* 12.8 (1968), pp. 277–280. DOI: 10.1063/1.1651991.

[9] D. E. McCumber. “Effect of ac Impedance on dc Voltage-Current Characteristics of Superconductor Weak-Link Junctions”. In: *J. Appl. Phys.* 39.7 (1968), pp. 3113–3118. DOI: 10.1063/1.1656743.

[10] W. J. Johnson. “Non linear propagation on superconducting tunneling junctions”. PhD thesis. Madison: University of Wisconsin, 1968.

[11] K. K. Likharev. *Dynamics of Josephson Junctions and Circuits*. Gordon and Breach,New York, 1986.

[12] T. A. Fulton and L. N. Dunkleberger. “Lifetime of the zero-voltage state in Josephson tunnel junctions”. In: *Phys. Rev. B* 9 (11 1974), pp. 4760–4768. DOI: 10.1103/PhysRevB.9.4760.

[13] H. A. Kramers. “Brownian motion in a field of force and the diffusion model of chemical reactions”. In: *Physica* 7.4 (1940), pp. 284–304. DOI: https://doi.org/10.1016/S0031-8914(40)90098-2.

[14] A. O. Caldeira and A. J. Leggett. “Influence of Dissipation on Quantum Tunneling in Macroscopic Systems”. In: *Phys. Rev. Lett.* 46 (4 1981), pp. 211–214. DOI: 10.1103/PhysRevLett.46.211.

[15] R. F. Voss and R. A. Webb. “Macroscopic Quantum Tunneling in 1-μm Nb Josephson Junctions”. In: *Phys. Rev. Lett.* 47 (4 1981), pp. 265–268. DOI: 10.1103/PhysRevLett.47.265.

[16] Mi. H. Devoret, J. M. Martinis, and J. Clarke. “Measurements of Macroscopic Quantum Tunneling out of the Zero-Voltage State of a Current-Biased Josephson Junction”. In: *Phys. Rev. Lett.* 55 (18 1985), pp. 1908–1911. DOI: 10.1103/PhysRevLett.55.1908.

[17] J. M. Martinis, M. H. Devoret, and J. Clarke. “Experimental tests for the quantum behavior of a macroscopic degree of freedom: The phase difference across a Josephson junction”. In: *Phys. Rev. B* 35 (10 1987), pp. 4682–4698. DOI: 10.1103/PhysRevB.35.4682.

[18] J. M. Martinis and R. L. Kautz. “Classical phase diffusion in small hysteretic Josephson junctions”. In: *Phys. Rev. Lett.* 63 (14 1989), pp. 1507–1510. DOI: 10.1103/PhysRevLett.63.1507.

[19] J. Männik et al. “Crossover from Kramers to phase-diffusion switching in moderately damped Josephson junctions”. In: *Phys. Rev. B* 71 (22 2005), p. 220509. DOI: 10.1103/PhysRevB.71.220509.

[20] W. C. Scott. “Hysteresis in the dc switching characteristics of Josephson Junction”. In: *Appl. Phys. Lett.* 17.4 (1970), pp. 166–169. DOI: 10.1063/1.1653350.

[21] N. F. Pedersen and K. Saermark. “Analytical solution for a Josephson-Junction model with capacitance”. In: *Physica* 69.2 (1973), pp. 572–578. DOI: https://doi.org/10.1016/0031-8914(73)90089-X.

[22] K. Serniak et al. “Hot Nonequilibrium Quasiparticles in Transmon Qubits”. In: *Phys. Rev. Lett.* 121 (15 2018), p. 157701.

[23] A. Bilmes et al. “Resolving the positions of defects in superconducting quantum bits”. In: *Sci. Rep.* 10 (1 2020), p. 3090.

[24] P. M. Chaikin and T. C. Lubensky. *Principles of Condensed Matter Physics*. Cambridge: Cambridge University Press, 1995.

[25] S. Blundell. *Magnetism in Condensed Matter*. Oxford University Press Inc, New York, NY, 2001.

[26] B. D. Cullity and C. D. Graham. *Introduction to Magnetic Materials*. Wiley-IEEE Press, New York, 2008.

[27] E. C. Stoner. “Collective electron ferromagnetism”. In: *Proc. R. Soc. Lond. A* 165.922 (1938), pp. 372–414. DOI: 10.1098/rspa.1938.0066.

[28] O. Fruchart and A. Thiaville. “Magnetism in reduced dimensions”. In: *Comptes Rendus Physique* 6.9 (2005), pp. 921–933. DOI: https://doi.org/10.1016/j.crhy.2005.10.011.

[29] T. Trunk et al. “Domain wall structure in Permalloy films with decreasing thickness at the Bloch to Néel transition”. In: *J. Appl. Phys.* 89.11 (2001), pp. 7606–7608. DOI: 10.1063/1.1355357.

[30] C. Kittel. *Introduction to Solid State Physics*. John Wiley & Son, New York, NY, 2004.

[31] S. Chikazumi. *Physics of Ferromagnetism*. Oxford University Press, Oxford, 1997.

[32] L. F. Yin et al. “Magnetocrystalline Anisotropy in Permalloy Revisited”. In: *Phys. Rev. Lett.* 97 (6 2006), p. 067203. DOI: 10.1103/PhysRevLett.97.067203. URL: https://link.aps.org/doi/10.1103/PhysRevLett.97.067203.

[33] F. Fiorillo et al. “Soft Magnetic Materials”. In: *Wiley Encyclopedia of Electrical and Electronics Engineering*. John Wiley & Sons, Ltd, 2016, pp. 1–42. DOI: https://doi.org/10.1002/047134608X.W4504.pub2.

[34] M. Tinkham. *Introduction to superconductivity*. McGraw-Hill,New York, 1975.

[35] A. I. Buzdin. “Proximity effects in superconductor-ferromagnet heterostructures”. In: *Rev. Mod. Phys.* 77 (3 2005), pp. 935–976. DOI: 10.1103/RevModPhys.77.935.

[36] G. Deutscher and P. G. de Gennes. “Proximity Effects”. In: *Superconductivity*. Ed. by R. D. Parks. Marcel Dekker, New York, 1969, p. 1005.

[37] M. Yu. Kurpianov and V. F. Lukichev. “Influence of boundary transparency on the critical current of dirty SS’S structures”. In: *Sov. Phys.-JETP v.(6); p.* 67 (6 1988), pp. 1163–1168.

[38] Schäpers. *Superconductor/Semiconductor Junctions*. Springer Berlin, Heidelberg, 2001.

[39] B. A. Aminov, A. A. Golubov, and M. Yu. Kupriyanov. "Quasiparticle current in ballistic constrictions with finite transparencies of interfaces". In: *Phys. Rev. B* 53 (1 1996), pp. 365–373. DOI: 10.1103/PhysRevB.53.365. URL: https://link.aps.org/doi/10.1103/PhysRevB.53.365.

[40] A. F. Andreev. "The Thermal Conductivity of the Intermediate State in Superconductors". In: *Soviet Physics-JETP* 19 (6 1964), pp. 1228–1232.

[41] K. K. Likharev. "Superconducting weak links". In: *Rev. Mod. Phys.* 51 (1 1979), pp. 101–159. DOI: 10.1103/RevModPhys.51.101. URL: https://link.aps.org/doi/10.1103/RevModPhys.51.101.

[42] V. Ambegaokar and A. Baratoff. "Tunneling Between Superconductors". In: *Phys. Rev. Lett.* 10 (11 1963), pp. 486–489.

[43] V. V. Ryazanov et al. "Coupling of Two Superconductors through a Ferromagnet: Evidence for a π Junction". In: *Phys. Rev. Lett.* 86 (11 2001), pp. 2427–2430.

[44] S. M. Frolov et al. "Measurement of the current-phase relation of superconductor/ferromagnet/superconductor π Josephson junctions". In: *Phys. Rev. B* 70 (14 2004), p. 144505.

[45] H. Sellier et al. "Half-Integer Shapiro Steps at the $0-\pi$ Crossover of a Ferromagnetic Josephson Junction". In: *Phys. Rev. Lett.* 92 (25 2004), p. 257005.

[46] T. Kontos et al. "Josephson Junction through a Thin Ferromagnetic Layer: Negative Coupling". In: *Phys. Rev. Lett.* 89 (13 2002), p. 137007.

[47] Y. Blum et al. "Oscillations of the Superconducting Critical Current in Nb-Cu-Ni-Cu-Nb Junctions". In: *Phys. Rev. Lett.* 89 (18 2002), p. 187004.

[48] V. A. Oboznov et al. "Thickness Dependence of the Josephson Ground States of Superconductor-Ferromagnet-Superconductor Junctions". In: *Phys. Rev. Lett.* 96 (19 2006), p. 197003.

[49] J. W. A. Robinson et al. "Critical Current Oscillations in Strong Ferromagnetic π Junctions". In: *Phys. Rev. Lett.* 97 (17 2006), p. 177003.

[50] A. Pal et al. “Pure second harmonic current-phase relation in spin-filter Josephson junctions”. In: *Nat. Commun.* 5 (2014), p. 4340.

[51] J. Linder and J. W. A. Robinson. “Superconducting spintronics”. In: *Nat. Phys.* 11 (2015), pp. 307–315.

[52] J. Linder and J. W. A. Robinson. “Superconducting spintronics”. In: *Nat. Phys.* 11 (2015), pp. 307–315.

[53] N. Banerjee et al. “Evidence for spin selectivity of triplet pairs in superconducting spin valves”. In: *Nat. Commun.* 5 (2014), p. 3048.

[54] N. Banerjee, J. W. A. Robinson, and M. G. Blamire. “Reversible control of spin-polarized supercurrents in ferromagnetic Josephson junctions”. In: *Nat. Commun.* 5 (2014), p. 4771.

[55] V. V. Bol’ginov et al. “Magnetic switches based on Nb-PdFe-Nb Josephson junctions with a magnetically soft ferromagnetic interlayer”. In: *JETP Lett.* 95 (2012), p. 366.

[56] O. M. Kapran et al. “Crossover between short- and long-range proximity effects in superconductor/ferromagnet/superconductor junctions with Ni-based ferromagnets”. In: *Phys. Rev. B* 103 (9 2021), p. 094509. DOI: 10.1103/PhysRevB.103.094509. URL: https://link.aps.org/doi/10.1103/PhysRevB.103.094509.

[57] T. I. Larkin et al. “Ferromagnetic Josephson switching device with high characteristic voltage”. In: *Appl. Phys. Lett.* 100 (2012), p. 222601.

[58] S. V. Bakurskiy et al. “Theory of supercurrent transport in SIsFS Josephson junctions”. In: *Phys. Rev. B* 88 (14 2013), p. 144519. DOI: 10.1103/PhysRevB.88.144519. URL: https://link.aps.org/doi/10.1103/PhysRevB.88.144519.

[59] S. V. Bakurskiy et al. “Theoretical model of superconducting spintronic SIsFS devices”. In: *Appl. Phys. Lett.* 102.19 (2013), p. 192603. DOI: 10.1063/1.4805032.

[60] I. V. Vernik et al. “Magnetic Josephson Junctions With Superconducting Interlayer for Cryogenic Memory”. In: *IEEE Trans. Appl. Supercond.* 23.3 (2013), pp. 1701208–1701208. DOI: 10.1109/TASC.2012.2233270.

[61] I. I. Soloviev et al. “Beyond Moore’s technologies: operation principles of a superconductor alternative”. In: *Beilstein J. Nanotechnol.* 8 (2017), pp. 2689–2710. DOI: doi:10.3762/bjnano.8.269.

[62] R. Caruso et al. “RF assisted switching in magnetic Josephson junctions”. In: *J. Appl. Phys.* 123 (2018), p. 133901.

[63] E. Goldobin et al. “Memory cell based on a Josephson junction”. In: *Appl. Phys. Lett.* 102.24 (2013), p. 242602. DOI: 10.1063/1.4811752.

[64] C. Bell et al. “Controllable Josephson current through a pseudospin-valve structure”. In: *Appl. Phys. Lett.* 84.7 (2004), pp. 1153–1155. DOI: 10.1063/1.1646217.

[65] B. Baek et al. “Hybrid superconducting-magnetic memory device using competing order parameters”. In: *Nat. Commun.* 5.1 (2014), p. 3888. DOI: 10.1038/ncomms4888.

[66] M. Abd El Qader et al. “Switching at small magnetic fields in Josephson junctions fabricated with ferromagnetic barrier layers”. In: *Appl. Phys. Lett.* 104.2 (2014), p. 022602. DOI: 10.1063/1.4862195.

[67] I. P. Nevirkovets and O. A. Mukhanov. “Memory Cell for High-Density Arrays Based on a Multiterminal Superconducting-Ferromagnetic Device”. In: *Phys. Rev. Applied* 10 (3 2018), p. 034013. DOI: 10.1103/PhysRevApplied.10.034013.

[68] O. A. Mukhanov et al. “Josephson Junctions for Digital Applications: Single Flux Quantum Logic”. In: *Springer Series in Materials Science*. Springer Series in Materials Science. Springer Verlag, 2019, pp. 611–701. DOI: 10.1007/978-3-030-20726-7_16.

[69] I. A. Golovchanskiy et al. “Magnetization dynamics in dilute Pd_{1-x} Fe_x thin films and patterned microstructures considered for superconducting electronics”. In: *J. Appl. Phys.* 120.16 (2016), p. 163902. DOI: 10.1063/1.4965991.

[70] V. V. Bol’ginov, O. A. Tikhomirov, and L. S.. Uspenskaya. “Two-component magnetization in $Pd_{99}Fe_{01}$ thin films”. In: *JETP Letters* 105 (2017), pp. 169–173. DOI: 10.1134/S0021364017030055.

[71] I. A. Golovchanskiy et al. “Micromagnetic modeling of critical current oscillations in magnetic Josephson junctions”. In: *Phys. Rev. B* 94 (21 2016), p. 214514. DOI: 10.1103/PhysRevB.94.214514.

[72] L. N. Karelina et al. “Scalable memory elements based on rectangular SIsFS junctions”. In: *J. Appl. Phys.* 130.17 (2021), p. 173901. DOI: 10.1063/5.0063274.

[73] E. C. Gingrich et al. “Spin-triplet supercurrent in Co/Ni multilayer Josephson junctions with perpendicular anisotropy”. In: *Phys. Rev. B* 86 (22 2012), p. 224506. DOI: 10.1103/PhysRevB.86.224506. URL: https://link.aps.org/doi/10.1103/PhysRevB.86.224506.

[74] A. Ruotolo et al. “Perpendicular magnetic anisotropy and structural properties of NiCu/Cu multilayers”. In: *J. Appl. Phys.* 96.1 (2004), pp. 512–518. DOI: 10.1063/1.1757658.

[75] G. Wild et al. “Josephson coupling and Fiske dynamics in ferromagnetic tunnel junctions”. In: *EPJ B* 78 (2010), pp. 509–523. DOI: 10.1140/epjb/e2010-10636-4.

[76] N. Satchell et al. “Pt and CoB trilayer Josephson π junctions with perpendicular magnetic anisotropy”. In: *Sci. Rep.* 27.11 (2021), p. 11173. DOI: 10.1038/s41598-021-90432-y.

[77] B. M. Niedzielski et al. “S/F/S Josephson junctions with single-domain ferromagnets for memory applications”. In: *Supercond. Sci. Technol.* 28.8 (2015), p. 085012.

[78] M. Volmer and J. Neamtu. "Simulated and measured hysteresis curves for thin films". In: *Physica B Condens.* 372.1 (2006), pp. 198–201. DOI: https://doi.org/10.1016/j.physb.2005.10.047.

[79] M. Schneider and H. Hoffmann. "Magnetization loops of submicron ferromagnetic permalloy dot arrays". In: *J. Appl. Phys.* 86.8 (1999), pp. 4539–4543. DOI: 10.1063/1.371399.

[80] L. S. Uspenskaya et al. "Domain structure and magnetization of the permalloy/niobium bilayers". In: *J. Appl. Phys.* 113.16 (2013), p. 163907. DOI: 10.1063/1.4803051.

[81] C. Cirillo et al. "Long-range proximity effect in Nb-based heterostructures induced by a magnetically inhomogeneous permalloy layer". In: *New J. Phys.* 19.2 (2017), p. 023037. DOI: 10.1088/1367-2630/aa5de8. URL: https://doi.org/10.1088/1367-2630/aa5de8.

[82] A. F. Mayadas, J. F. Janak, and A. Gangulee. "Resistivity of Permalloy thin films". In: *J. Appl. Phys.* 45.6 (1974), pp. 2780–2781.

[83] P. Seidel and J. Richter. "Theoretical Investigation of the Critical Josephson Current of Niobium-Lead Tunnel Junctions". In: *Phys. Status Solidi B* 99.2 (1980), pp. 607–613. DOI: https://doi.org/10.1002/pssb.2220990220.

[84] A. A. Golubov et al. "Proximity effect in superconductor-insulator-superconductor Josephson tunnel junctions: Theory and experiment". In: *Phys. Rev. B* 51 (2 1995), pp. 1073–1089. DOI: 10.1103/PhysRevB.51.1073.

[85] M. Weides et al. "High quality ferromagnetic 0 and π Josephson tunnel junctions". In: *Appl. Phys. Lett.* 89.12 (2006), p. 122511. DOI: 10.1063/1.2356104.

[86] J. Pfeiffer et al. "Static and dynamic properties of 0, π, and $0-\pi$ ferromagnetic Josephson tunnel junctions". In: *Phys. Rev. B* 77 (21 2008), p. 214506. DOI: 10.1103/PhysRevB.77.214506.

[87] C. G"urlich et al. "Visualizing supercurrents in ferromagnetic Josephson junctions with various arrangements of 0 and π segments". In: *Phys. Rev. B* 81 (9 2010), p. 094502. DOI: 10.1103/PhysRevB.81.094502.

[88] M. Caputo et al. "Influence of the magnetic configuration on the vortex-lattice instability in Nb/permalloy bilayers". In: *Phys. Rev. B* 96 (17 2017), p. 174519. DOI: 10.1103/PhysRevB.96.174519.

[89] M. Maezawa et al. "Specific capacitance of Nb/AlO_x/Nb Josephson junctions with critical current densities in the range of 0.1–18 kA/cm^2". In: *Appl. Phys. Lett.* 66.16 (1995), pp. 2134–2136. DOI: 10.1063/1.113927.

[90] R. Held et al. "Superconducting memory based on ferromagnetism". In: *Appl. Phys. Lett.* 89.16 (2006), p. 163509. DOI: 10.1063/1.2362870.

[91] C. Monton, F. de la Cruz, and J. Guimpel. "Magnetic behavior of superconductor/ferromagnet superlattices". In: *Phys. Rev. B* 75 (6 2007), p. 064508. DOI: 10.1103/PhysRevB.75.064508. URL: https://link.aps.org/doi/10.1103/PhysRevB.75.064508.

[92] "Magnetization modification by superconductivity in Nb/$Ni_{80}Fe_{20}$/Nb trilayers". In: *J. Magn. Magn. Mater.* 322.1 (2010), pp. 169–172. ISSN: 0304-8853. DOI: https://doi.org/10.1016/j.jmmm.2009.09.001.

[93] T. S. Khaire, W. P. Pratt, and N. O. Birge. "Critical current behavior in Josephson junctions with the weak ferromagnet PdNi". In: *Phys. Rev. B* 79 (2009), p. 094523.

[94] O. Bourgeois et al. "Josephson effect through a ferromagnetic layer". In: *Eur. Phys. J. B* 21 (1 2001), pp. 75–80. DOI: https://doi.org/10.1007/s100510170215.

[95] R. Satariano et al. "Inverse magnetic hysteresis of the Josephson supercurrent: study of the magnetic properties of thin Nb/Py interfaces". In: *Phys. Rev. B* 103 (2021), p. 224521. DOI: 10.1103/PhysRevB.103.224521.

[96] R. Satariano et al. “Investigation of the inverse magnetic hysteresis of the Josephson supercurrent in magnetic Josephson Junctions”. In: *IEEE Trans. Appl. Supercond.* (2021), pp. 1–1. DOI: 10.1109/TASC.2021.3129983.

[97] B. Mora et al. “Engineering magnetic nanostructures with inverse hysteresis loops”. In: *Nano Res.* 9 (8 2016), pp. 2347–2353. DOI: 10.1007/s12274-016-1121-y.

[98] T. Maity et al. “Observation of complete inversion of the hysteresis loop in a bimodal magnetic thin film”. In: *Phys. Rev. B* 95 (10 2017), p. 100401. DOI: 10.1103/PhysRevB.95.100401.

[99] L. Parlato et al. “Characterization of scalable Josephson memory element containing a strong ferromagnet”. In: *J. Appl. Phys.* 127 (2020), p. 193901. DOI: https://doi.org/10.1063/5.0004554.

[100] R. McDermott et al. “Quantum–classical interface based on single flux quantum digital logic”. In: *Quantum Sci. Technol.* 3.2 (2018), p. 024004. DOI: 10.1088/2058-9565/aaa3a0.

[101] J. W. A. Robinson et al. “Zero to π transition in superconductor-ferromagnet-superconductor junctions”. In: *Phys. Rev. B* 76 (9 2007), p. 094522.

[102] A. Iovan, T. Golod, and V. M. Krasnov. “Controllable generation of a spin-triplet supercurrent in a Josephson spin valve”. In: *Phys. Rev. B* 90 (13 2014), p. 134514. DOI: 10.1103/PhysRevB.90.134514.

[103] V. P. Morozov A. V.and Alekseev, V. A. Naumov, and V. V. Morozov. “The Study of Anisotropy and Domain Condition of Permalloy Thin Films”. In: *J. Nano- Electron. Phys* 5.4 (2013), pp. 4016-1-04016–4.

[104] A. Yu Aladyshkin et al. “Nucleation of superconductivity and vortex matter in superconductor–ferromagnet hybrids”. In: *Supercond. Sci. Technol.* 22.5 (2009), p. 053001. DOI: 10.1088/0953-2048/22/5/053001.

[105] P. J. Curran et al. “Irreversible magnetization switching at the onset of superconductivity in a superconductor ferromagnet hybrid”. In: *Appl. Phys. Lett.* 107.26 (2015), p. 262602. DOI: 10L.1063/1.4938467.

[106] J. del Valle et al. “Superconducting/magnetic Three-state Nanodevice for Memory and Reading Applications”. In: *Sci. Rep.* 5.1 (2015), p. 15210. DOI: 10.1038/srep15210.

[107] V. K. Vlasko-Vlasov et al. “Magnetic gates and guides for superconducting vortices”. In: *Phys. Rev. B* 95 (14 2017), p. 144504. DOI: 10.1103/PhysRevB.95.144504.

[108] T. Golod, A. Iovan, and V. M. Krasnov. “Single Abrikosov vortices as quantized information bits”. In: *Nat. Commun.* 6 (1 2015), p. 8628. DOI: 10.1038/ncomms9628.

[109] S. Bergeret, A. F. Volkov, and K. B. Efetov. “Induced ferromagnetism due to superconductivity in superconductor-ferromagnet structures”. In: *Phys. Rev. B* 69 (2004), p. 174504.

[110] F. S. Bergeret, A. F. Volkov, and K. B. Efetov. “Odd triplet superconductivity and related phenomena in superconductor-ferromagnet structures”. In: *Rev. Mod. Phys.* 77 (2005), pp. 1321–1373.

[111] F. S Bergeret, A. F Volkov, and K. B Efetov. “Spin screening of magnetic moments in superconductors”. In: *EPL* 66.1 (2004), pp. 111–117. DOI: https://doi.org/10.1209/epl/i2004-10003-3.

[112] A. F. Volkov, F. S. Bergeret, and K. B. Efetov. “Spin polarization and orbital effects in superconductor-ferromagnet structures”. In: *Phys. Rev. B* 99 (14 2019), p. 144506.

[113] S. Mironov, A. S. Mel’nikov, and A. Buzdin. “Electromagnetic proximity effect in planar superconductor-ferromagnet structures”. In: *Appl. Phys. Lett.* 113.2 (2018), p. 022601. DOI: 10.1063/1.5037074.

[114] S. V. Mironov et al. “Electromagnetic Proximity Effect and the Fulde–Ferrell–Larkin–Ovchinnikov Instability in Hybrid Superconductor–Ferromagnet Structures (Brief Review)”. In: *JETP Lett.* 113.2 (2021), pp. 92–101. DOI: https://doi.org/10.1134/S0021364021020077.

[115] Zh. Devizorova et al. “Electromagnetic proximity effect controlled by spin-triplet correlations in superconducting spin-valve structures”. In: *Phys. Rev. B* 99 (10 2019), p. 104519. DOI: 10.1103/PhysRevB.99.104519.

[116] M. G. Flokstra et al. “Meissner screening as a probe for inverse superconductor-ferromagnet proximity effects”. In: *Phys. Rev. B* 104 (6 2021), p. L060506.

[117] Yu. N. Khaydukov et al. “On the feasibility to study inverse proximity effect in a single S/F bilayer by Polarized Neutron Reflectometry”. In: *JETP Letters* 98 (2 2013), pp. 107–110.

[118] J. Xia et al. “Inverse Proximity Effect in Superconductor-Ferromagnet Bilayer Structures”. In: *Phys. Rev. Lett.* 102 (2009), p. 087004.

[119] R. I. Salikhov et al. “Experimental Observation of the Spin Screening Effect in Superconductor/Ferromagnet Thin Film Heterostructures”. In: *Phys. Rev. Lett.* 102.8 (2009), p. 087003.

[120] M. G. Flokstra et al. “Remotely induced magnetism in a normal metal using a superconducting spin-valve”. In: *Nat. Phys.* 12 (1 2016), pp. 57–61.

[121] S. M. Dahir, A. F. Volkov, and I.M. Eremin. “Phase-dependent spin polarization of Cooper pairs in magnetic Josephson junctions”. In: *Phys. Rev. B* 100 (13 2019), p. 134513. DOI: 10.1103/PhysRevB.100.134513.

[122] A. F. Volkov. In: *private correspondence* (2022).

[123] R. J. Wakelin and E. L. Yates. “A Study of the Order-Disorder Transformation in Iron-Nickel Alloys in the Region FeNi3”. In: *Proc. Phys. Soc. London* 66.3 (1953), p. 221. DOI: 10.1088/0370-1301/66/3/310.

[124] R. Zhang and R. F. Willis. "Thickness-Dependent Curie Temperatures of Ultrathin Magnetic Films: Effect of the Range of Spin-Spin Interactions". In: *Phys. Rev. Lett.* 86 (12 2001), pp. 2665–2668. DOI: 10.1103/PhysRevLett.86.2665.

[125] K. Jeon et al. "Effect of Meissner Screening and Trapped Magnetic Flux on Magnetization Dynamics in Thick Nb/$Ni_{80}Fe_{20}$/Nb Trilayers". In: *Phys. Rev. Appl.* 11 (1 2019), p. 014061. DOI: 10.1103/PhysRevApplied.11.014061. URL: https://link.aps.org/doi/10.1103/PhysRevApplied.11.014061.

[126] H. Zhou, X. Gong, and X. Jin. "Magnetic properties of superconducting Bi/Ni bilayers". In: *J. Magn. Magn. Mater.* 422 (2017), pp. 73–76. DOI: https://doi.org/10.1016/j.jmmm.2016.08.073.

[127] D. Stamopoulos et al. "Effective ferromagnetic coupling between a superconductor and a ferromagnet in LaCaMnONb hybrids". In: *Phys. Rev. B* 72 (21 2005), p. 212514. DOI: 10.1103/PhysRevB.72.212514.

[128] H. Wu et al. "Experimental evidence of magnetization modification by superconductivity in a $Nb/Ni_{81}Fe_{19}$ multilayer". In: *Phys. Rev. B* 76 (2 2007), p. 024416. DOI: 10.1103/PhysRevB.76.024416. URL: https://link.aps.org/doi/10.1103/PhysRevB.76.024416.

[129] R. Satariano. "Nanoscale spin ordering and full screening in tunnel ferromagnetic Josephson junctions". In: *in preparation* (2023).

[130] V. N. Gubankov et al. "Influence of trapped Abrikosov vortices on the critical current of the Josephson tunnel junction". In: *Supercond. Sci. Technol.* 5 (1992), pp. 168–173. DOI: 10.1088/0953-2048/5/3/011.

[131] W. M. Martinez, W. P. Pratt, and N. O. Birge. "Amplitude Control of the Spin-Triplet Supercurrent in $S/F/S$ Josephson Junctions". In: *Phys. Rev. Lett.* 116 (7 2016), p. 077001. DOI: 10.1103/PhysRevLett.116.077001. URL: https://link.aps.org/doi/10.1103/PhysRevLett.116.077001.

[132] C. Bell et al. “Characteristics of strong ferromagnetic Josephson junctions with epitaxial barriers”. In: *Phys. Rev. B* 71 (18 2005), p. 180501. DOI: 10.1103/PhysRevB.71.180501. URL: https://link.aps.org/doi/10.1103/PhysRevB.71.180501.

[133] J. A. Glick et al. “Critical current oscillations of elliptical Josephson junctions with single-domain ferromagnetic layers”. In: *J. Appl. Phys.* 122.13 (2017), p. 133906. DOI: 10.1063/1.4989392.

[134] B. M. Niedzielski et al. “Spin-valve Josephson junctions for cryogenic memory”. In: *Phys. Rev. B* 97 (2 2018), p. 024517. DOI: 10.1103/PhysRevB.97.024517. URL: https://link.aps.org/doi/10.1103/PhysRevB.97.024517.

[135] N. Satchell et al. *Limits of magnetic interactions in Ni-Nb ferromagnet-superconductor bilayers*. 2022. DOI: 10.48550/ARXIV.2209.15366.

[136] T. Golod, A. Pagliero, and V. M. Krasnov. “Two mechanisms of Josephson phase shift generation by an Abrikosov vortex”. In: *Phys. Rev. B* 100 (17 2019), p. 174511. DOI: 10.1103/PhysRevB.100.174511.

[137] H. G. Ahmad et al. “Hybrid ferromagnetic transmon qubit: Circuit design, feasibility, and detection protocols for magnetic fluctuations”. In: *Phys. Rev. B* 105 (21 2022), p. 214522. DOI: 10.1103/PhysRevB.105.214522.

[138] R. Kleiner et al. “Superconducting quantum interference devices: State of the art and applications”. In: *Proceedings of the IEEE* 92.10 (2004), pp. 1534–1548. DOI: 10.1109/JPROC.2004.833655.

[139] P.L. Richards and Tek-Ming Shen. “Superconductive devices for millimeter wave detection, mixing, and amplification”. In: *IEEE Transactions on Electron Devices* 27.10 (1980), pp. 1909–1920. DOI: 10.1109/T-ED.1980.20128.

[140] J. Clarke and F. Wilhelm. “Superconducting quantum bits.” In: *Nat.* 453.10 (2008), pp. 1031–1042. DOI: 10.1109/T-ED.1980.20128.

[141] J. Q. You and F. Nori. "Atomic physics and quantum optics using superconducting circuits". In: *Nature* 474.7353 (2011), pp. 589–597. DOI: 10.1038/nature10122.

[142] A. F Kockum and F. Nori. "Quantum Bits with Josephson Junctions". In: *Fundamentals and Frontiers of the Josephson Effect*. Ed. by F. Tafuri. Springer International Publishing, Cham, 2019, pp. 703–741.

[143] P. Krantz et al. "A quantum engineer's guide to superconducting qubits". In: *Appl. Phys. Rev.* 6.2 (2019), p. 021318. DOI: 10.1063/1.5089550.

[144] W. D. Oliver and P. B. Welander. "Materials in superconducting quantum bits". In: *MRS Bulletin* 38.10 (2013), pp. 816–825. DOI: 10.1557/mrs.2013.229.

[145] J. Koch et al. "Charge-insensitive qubit design derived from the Cooper pair box". In: *Phys. Rev. A* 76 (4 2007), p. 042319. DOI: 10.1103/PhysRevA.76.042319.

[146] M. Kjaergaard et al. "Superconducting Qubits: Current State of Play". In: *Annual Review of Condensed Matter Physics* 11.1 (2020), pp. 369–395. DOI: 10.1146/annurev-conmatphys-031119-050605.

[147] J. M. Martinis et al. "Decoherence in Josephson Qubits from Dielectric Loss". In: *Phys. Rev. Lett.* 95 (21 2005), p. 210503. DOI: 10.1103/PhysRevLett.95.210503. URL: https://link.aps.org/doi/10.1103/PhysRevLett.95.210503.

[148] S. Oh et al. "Elimination of two level fluctuators in superconducting quantum bits by an epitaxial tunnel barrier". In: *Phys. Rev. B* 74 (10 2006), p. 100502. DOI: 10.1103/PhysRevB.74.100502. URL: https://link.aps.org/doi/10.1103/PhysRevB.74.100502.

[149] M. P. Weides et al. "Coherence in a transmon qubit with epitaxial tunnel junctions". In: *Appl. Phys. Lett.* 99.26 (2011), p. 262502. DOI: 10.1063/1.3672000. eprint: https://doi.org/10.1063/1.3672000. URL: https://doi.org/10.1063/1.3672000.

[150] A. P. M. Place et al. “New material platform for superconducting transmon qubits with coherence times exceeding 0.3 milliseconds”. In: *Nat. Commun.* 12.1 (2021), p. 1779. DOI: 10.1038/s41467-021-22030-5.

[151] C. Wang et al. “Surface participation and dielectric loss in superconducting qubits”. In: *Appl. Phys. Letters* 107.16 (2015), p. 162601. DOI: 10.1063/1.4934486. eprint: https://doi.org/10.1063/1.4934486. URL: https://doi.org/10.1063/1.4934486.

[152] A. Bilmes et al. “Probing defect densities at the edges and inside Josephson junctions of superconducting qubits”. In: *npj Quantum Inf* 8.1 (2022), p. 24. DOI: 10.1038/s41534-022-00532-4. URL: https://doi.org/10.1038/s41534-022-00532-4.

[153] K. Serniak et al. “Hot Nonequilibrium Quasiparticles in Transmon Qubits”. In: *Phys. Rev. Lett.* 121 (15 2018), p. 157701. DOI: 10.1103/PhysRevLett.121.157701. URL: https://link.aps.org/doi/10.1103/PhysRevLett.121.157701.

[154] J. M. Martinis, M. Ansmann, and J. Aumentado. “Energy Decay in Superconducting Josephson-Junction Qubits from Nonequilibrium Quasiparticle Excitations”. In: *Phys. Rev. Lett.* 103 (9 2009), p. 097002. DOI: 10.1103/PhysRevLett.103.097002. URL: https://link.aps.org/doi/10.1103/PhysRevLett.103.097002.

[155] Y. Dong et al. “Measurement of Quasiparticle Diffusion in a Superconducting Transmon Qubit”. In: *Appl. Sci* 12.17 (2022). ISSN: 2076-3417. DOI: 10.3390/app12178461. URL: https://www.mdpi.com/2076-3417/12/17/8461.

[156] E. Paladino et al. “$\mathbf{1}/\mathbf{f}$ noise: Implications for solid-state quantum information”. In: *Rev. Mod. Phys.* 86 (2 2014), pp. 361–418. DOI: 10.1103/RevModPhys.86.361. URL: https://link.aps.org/doi/10.1103/RevModPhys.86.361.

[157] J. D. Strand et al. “First-order sideband transitions with flux-driven asymmetric transmon qubits”. In: *Phys. Rev. B* 87 (22 2013), p. 220505. DOI: 10.1103/PhysRevB.87.220505. URL: https://link.aps.org/doi/10.1103/PhysRevB.87.220505.

[158] M. D. Hutchings et al. “Tunable Superconducting Qubits with Flux-Independent Coherence”. In: *Phys. Rev. Applied* 8 (4 2017), p. 044003. DOI: 10.1103/PhysRevApplied.8.044003.

[159] T. W. Larsen et al. “Semiconductor-Nanowire-Based Superconducting Qubit”. In: *Phys. Rev. Lett.* 115 (12 2015), p. 127001. DOI: 10.1103/PhysRevLett.115.127001. URL: https://link.aps.org/doi/10.1103/PhysRevLett.115.127001.

[160] F. Luthi et al. “Evolution of Nanowire Transmon Qubits and Their Coherence in a Magnetic Field”. In: *Phys. Rev. Lett.* 120 (10 2018), p. 100502. DOI: 10.1103/PhysRevLett.120.100502. URL: https://link.aps.org/doi/10.1103/PhysRevLett.120.100502.

[161] L. Casparis et al. “Superconducting gatemon qubit based on a proximitized two-dimensional electron gas”. In: *Nat. Nanotechnol.* 13.10 (2018), pp. 913–919. DOI: 10.1038/s41565-018-0207-y.

[162] J. I. Wang et al. “Coherent control of a hybrid superconducting circuit made with graphene-based van der Waals heterostructures”. In: *Nat. Nanotechnol.* 14 (2 2019), pp. 120–125. DOI: 10.1038/s41565-018-0329-2.

[163] A. K. Feofanov et al. “Implementation of superconductor/ferromagnet/superconductor π-shifters in superconducting digital and quantum circuits”. In: *Nat. Phys.* 6 (8 2010), pp. 593–597. DOI: 10.1103/PhysRevB.103.094509. URL: https://link.aps.org/doi/10.1103/PhysRevB.103.094509.

[164] T. Yamashita et al. “Superconducting π Qubit with a Ferromagnetic Josephson Junction”. In: *Phys. Rev. Lett.* 95 (9 2005), p. 097001. DOI: 10.1103/PhysRevLett.95.097001. URL: https://link.aps.org/doi/10.1103/PhysRevLett.95.097001.

[165] T. Yamashita, S. Takahashi, and S. Maekawa. "Superconducting π qubit with three Josephson junctions". In: *Appl. Phys. Lett.* 88.13 (2006), p. 132501. DOI: 10.1063/1.2189191. eprint: https://doi.org/10.1063/1.2189191. URL: https://doi.org/10.1063/1.2189191.

[166] S. Kawabata et al. "Macroscopic quantum dynamics of π junctions with ferromagnetic insulators". In: *Phys. Rev. B* 74 (18 2006), p. 180502. DOI: 10.1103/PhysRevB.74.180502. URL: https://link.aps.org/doi/10.1103/PhysRevB.74.180502.

[167] T. Yamashita et al. "π phase shifter based on NbN-based ferromagnetic Josephson junction on a silicon substrate". In: *Sci. Rep.* 10 (1 2020), p. 13687. DOI: 10.1038/s41598-020-70766-9.

[168] A. V. Shcherbakova et al. "Fabrication and measurements of hybrid Nb/Al Josephson junctions and flux qubits with π-shifters". In: 28.2 (2020), p. 025009. DOI: https://doi.org/10.1007/s10948-020-05577-0. URL: https://dx.doi.org/10.1088/0953-2048/28/2/025009.

[169] J. M. Martinis. "Superconducting phase qubits". In: *Quantum. Inf. Process.* 8.2 (2009), pp. 81–103. DOI: 10.1007/s11128-009-0105-1.

[170] Y. Dong et al. "Measurement of Quasiparticle Diffusion in a Superconducting Transmon Qubit". In: *Appl. Sci.* 12.17 (2022). ISSN: 2076-3417. DOI: 10.3390/app12178461. URL: https://www.mdpi.com/2076-3417/12/17/8461.

[171] K. Senapati, M. G. Blamire, and Z. H. Barber. "Spin-filter Josephson junctions". In: *Nat. Mater.* 10 (2011), pp. 849–852. DOI: 10.1038/nmat3116.

[172] H.G. Ahmad et al. "Electrodynamics of Highly Spin-Polarized Tunnel Josephson Junctions". In: *Phys. Rev. Appl.* 13 (1 2020), p. 014017. DOI: 10.1103/PhysRevApplied.13.014017. URL: https://link.aps.org/doi/10.1103/PhysRevApplied.13.014017.

[173] H. G. Ahmad et al. “Critical Current Suppression in Spin-Filter Josephson Junctions”. In: *J. Supercond. Nov. Magn.* 33 (10 2020), pp. 3043–3049. DOI: https://doi.org/10.1007/s10948-020-05577-0.

[174] D. Massarotti et al. “Macroscopic quantum tunnelling in spin filter ferromagnetic Josephson junctions”. In: *Nat. Commun.* 6 (2015), p. 7376. DOI: 10.1038/ncomms8376.

[175] F. Yan et al. “Tunable Coupling Scheme for Implementing High-Fidelity Two-Qubit Gates”. In: *Phys. Rev. Appl.* 10 (5 2018), p. 054062. DOI: 10.1103/PhysRevApplied.10.054062. URL: https://link.aps.org/doi/10.1103/PhysRevApplied.10.054062.

[176] Y. Sung et al. “Realization of High-Fidelity CZ and ZZ-Free iSWAP Gates with a Tunable Coupler”. In: *Phys. Rev. X* 11 (2 2021), p. 021058. DOI: 10.1103/PhysRevX.11.021058. URL: https://link.aps.org/doi/10.1103/PhysRevX.11.021058.

[177] J. C. Lee et al. “Nonlinear resonant behavior of a dispersive readout circuit for a superconducting flux qubit”. In: *Phys. Rev. B* 75 (14 2007), p. 144505. DOI: 10.1103/PhysRevB.75.144505. URL: https://link.aps.org/doi/10.1103/PhysRevB.75.144505.

[178] J. Lisenfeld et al. “Temperature Dependence of Coherent Oscillations in Josephson Phase Qubits”. In: *Phys. Rev. Lett.* 99 (17 2007), p. 170504. DOI: 10.1103/PhysRevLett.99.170504. URL: https://link.aps.org/doi/10.1103/PhysRevLett.99.170504.

[179] E. Hoskinson et al. “Quantum Dynamics in a Camelback Potential of a dc SQUID”. In: *Phys. Rev. Lett.* 102 (9 2009), p. 097004. DOI: 10.1103/PhysRevLett.102.097004. URL: https://link.aps.org/doi/10.1103/PhysRevLett.102.097004.

[180] M. Watanabe. “Technologies for the fabrication of nanoscale superconducting circuits”. In: *Modern Physics Letters B* 19.9 (2005), pp. 405–424. DOI: 10.1142/S0217984905008529. eprint: https://doi.org/

10.1142/S0217984905008529. URL: https://doi.org/10.1142/S0217984905008529.

[181] A. Osman et al. "Simplified Josephson-junction fabrication process for reproducibly high-performance superconducting qubits". In: *Appl. Phys. Lett.* 118.6 (2021), p. 064002. DOI: 10.1063/5.0037093.

[182] A. Vettoliere et al. "Aluminum-ferromagnetic Josephson tunnel junctions for high quality magnetic switching devices". In: *Appl. Phys. Lett.* 120.26 (2022), p. 262601. DOI: 10.1063/5.0101686.

[183] H. Kroger, L. N. Smith, and D. W. Jillie. "Selective niobium anodization process for fabricating Josephson tunnel junctions". In: *Appl. Phys. Lett.* 39.3 (1981), pp. 280–282. DOI: 10.1063/1.92672.

[184] M. Gurvitch, M. A. Washington, and H. A. Huggins. "High quality refractory Josephson tunnel junctions utilizing thin aluminum layers". In: *Appl. Phys. Lett.* 42.5 (1983), pp. 472–474. DOI: 10.1063/1.93974.

[185] A. Vettoliere et al. "High-Quality Ferromagnetic Josephson Junctions Based on Aluminum Electrodes". In: *Nanomaterials* 12.23 (2022). DOI: 10.3390/nano12234155.

[186] H.J. Mamin et al. "Merged - Transmons: Design and Qubit Performance". In: *Phys. Rev. Appl.* 16 (2 2021), p. 024023. DOI: 10.1103/PhysRevApplied.16.024023. URL: https://link.aps.org/doi/10.1103/PhysRevApplied.16.024023.

[187] R. Cristiano et al. "Investigation of subgap structures in high-quality Nb/AlO_x/Nb tunnel junctions". In: *Phys. Rev. B* 49 (1 1994), pp. 429–440. DOI: 10.1103/PhysRevB.49.429. URL: https://link.aps.org/doi/10.1103/PhysRevB.49.429.

[188] B. N. Taylor and E. Burstein. "Excess Currents in Electron Tunneling Between Superconductors". In: *Phys. Rev. Lett.* 10 (1 1963), pp. 14–17. DOI: 10.1103/PhysRevLett.10.14.

[189] J. R. Schrieffer and J. W. Wilkins. "Two-Particle Tunneling Processes Between Superconductors". In: *Phys. Rev. Lett.* 10 (1 1963), pp. 17–20. DOI: 10.1103/PhysRevLett.10.17. URL: https://link.aps.org/doi/10.1103/PhysRevLett.10.17.

[190] I. O. Kulik. "Magnitude of the Critical Josephson Tunnel Current". In: *Sov. J. Exp. Theor. Phys.* 22 (1966), p. 841.

[191] M. A. Sulangi et al. "Disorder and critical current variability in Josephson junctions". In: *J. Appl. Phys.* 127.3 (2020), p. 033901. DOI: 10.1063/1.5125765.

[192] Y. Ivry et al. "Universal scaling of the critical temperature for thin films near the superconducting-to-insulating transition". In: *Phys. Rev. B* 90 (21 2014), p. 214515. DOI: 10.1103/PhysRevB.90.214515. URL: https://link.aps.org/doi/10.1103/PhysRevB.90.214515.

[193] P. Townsend, S. Gregory, and R. G. Taylor. "Superconducting Behavior of Thin Films and Small Particles of Aluminum". In: *Phys. Rev. B* 5 (1 1972), pp. 54–66. DOI: 10.1103/PhysRevB.5.54.

[194] L. Marchegiani G.and Amico and G. Catelani. "Quasiparticles in Superconducting Qubits with Asymmetric Junctions". In: *PRX Quantum* 3 (4 2022), p. 040338. DOI: 10.1103/PRXQuantum.3.040338. URL: https://link.aps.org/doi/10.1103/PRXQuantum.3.040338.

[195] X. Hao, J. S. Moodera, and R. Meservey. "Spin-filter effect of ferromagnetic europium sulfide tunnel barriers". In: *Phys. Rev. B* 42 (13 1990), pp. 8235–8243. DOI: 10.1103/PhysRevB.42.8235. URL: https://link.aps.org/doi/10.1103/PhysRevB.42.8235.

[196] G. X. Miao et al. "Spin regulation in composite spin-filter barrier devices". In: *Nat. Commun.* 5 (1 2014), p. 3682. DOI: 10.1038/ncomms4682.

[197] R. Ferraiuolo et al. "Superconducting resonators: a path towards advanced quantum circuits". In: *2022 IEEE 15th Workshop on Low Temperature*

Electronics (WOLTE). 2022, pp. 1–4. DOI: 10.1109/WOLTE55422.2022.9882676.

[198] O. Mukhanov et al. "Scalable Quantum Computing Infrastructure Based on Superconducting Electronics". In: *2019 IEEE International Electron Devices Meeting (IEDM)*. 2019, pp. 31.2.1–31.2.4. DOI: 10.1109/IEDM19573.2019.8993634.

[199] L. Di Palma et al. "Discriminating the phase of a weak coherent tone with a flux-switchable superconducting circuit". In: *submitted* (2022).

[200] M. A. Qader et al. "The magnetic, electrical and structural properties of copper-permalloy alloys". In: *J. Magn. Magn. Mater.* 442 (2017), pp. 45–52. ISSN: 0304-8853. DOI: https://doi.org/10.1016/j.jmmm.2017.06.081. URL: https://www.sciencedirect.com/science/article/pii/S0304885317307035.

[201] G. Cao and Y. Wang. *Nanostructures and Nanomaterials*. 2nd. WORLD SCIENTIFIC, 2011. DOI: 10.1142/7885. eprint: https://www.worldscientific.com/doi/pdf/10.1142/7885. URL: https://www.worldscientific.com/doi/abs/10.1142/7885.

[202] S. Foner. "Versatile and Sensitive Vibrating-Sample Magnetometer". In: *Rev. Sci. Instrum.* 30.7 (1959), pp. 548–557. DOI: 10.1063/1.1716679. eprint: https://doi.org/10.1063/1.1716679. URL: https://doi.org/10.1063/1.1716679.

[203] P. Das, R. Bruyn de Ouboter, and K. W. Taconis. "A Realization of a London-Clarke-Mendoza Type Refrigerator". In: *Low Temperature Physics LT9*. Boston, MA: Springer US, 1965, pp. 1253–1255. ISBN: 978-1-4899-6443-4.

[204] James C. Ho, H. R. O'Neal, and Norman E. Phillips. "Low Temperature Heat Capacities of Constantan and Manganin". In: *Review of Scientific Instruments* 34.7 (1963), pp. 782–783. DOI: 10.1063/1.1718572. eprint: https://doi.org/10.1063/1.1718572. URL: https://doi.org/10.1063/1.1718572.